Proposal:
A Search for Sterile Neutrino at J-PARC Materials and Life Science Experimental Facility

September 2, 2013

M. Harada, S. Hasegawa, Y. Kasugai, S. Meigo, K. Sakai,
S. Sakamoto, K. Suzuya

JAEA, Tokai, Japan

E. Iwai, T. Maruyama, K. Nishikawa, R. Ohta

KEK, Tsukuba, JAPAN

M. Niiyama

Department of Physics, Kyoto University, JAPAN

S. Ajimura, T. Hiraiwa, T. Nakano, M. Nomachi, T. Shima

RCNP, Osaka University, JAPAN

T. J. C. Bezerra, E. Chauveau, T. Enomoto, H. Furuta, H. Sakai,
F. Suekane

Research Center for Neutrino Science, Tohoku University, JAPAN

M. Yeh

Brookhaven National Laboratory, Upton, NY 11973-5000, USA

W. C. Louis, G. B. Mills, R. Van de Water

Los Alamos National Laboratory, Los Alamos, NM 87545, USA

[1]

---

[1]Spokes person : Takasumi Maruyama (KEK)
takasumi.maruyama@kek.jp

Executive Summary

In the last fifteen years, several experiments have reported neutrino phenomena, which may indicate the existence of more than three kinds of neutrinos. The experimental indications include an excess of $\bar{\nu}_e$ events in a predominantly μ^+ decay, a deficiency of ν_e events from a β source, and a $\bar{\nu}_e$ deficiency in nuclear reactors. There is also an indication of an excess of electromagnetic shower events in a predominantly ν_μ and $\bar{\nu}_\mu$ neutrino beams. If these phenomena are confirmed and are shown to be due to neutrino oscillations, then the corresponding Δm^2 is about an eV^2, which is orders of magnitude larger than those in solar and atmospheric neutrinos oscillations. This requires the existence of a new mass state(s) near an eV in addition to the three standard mass states. This, in turn, requires an additional neutrino state(s) in nature both in mass and flavor (in addition to ν_e, ν_μ, and ν_τ). Considering the Z-boson width, the new flavor state does not couple to the Z-boson. Therefore, this is a new kind of lepton, namely a sterile neutrino, which does not interact electromagnetically or weakly.

We propose a definite search for the existence of neutrino oscillations with Δm^2 near 1 eV^2 at the J-PARC Materials and Life Science Experimental Facility (MLF). With the 3 GeV Rapid Cycling Synchrotron (RCS) and spallation neutron target, an intense neutrino beam from muon decay at rest (μDAR) is available. Neutrinos come predominantly from μ^+ decay : $\mu^+ \rightarrow e^+ + \bar{\nu}_\mu + \nu_e$. The oscillation to be searched for is $\bar{\nu}_\mu \rightarrow \bar{\nu}_e$ which is detected by the inverse β decay interaction $\bar{\nu}_e + p \rightarrow e^+ + n$, followed by a γ from neutron capture.

The unique features of the proposed experiment, compared with the prior experiment at LSND and experiments using conventional horn focused beams, are;

(1) The pulsed beam with about 600 ns spill width from J-PARC RCS and muon long lifetime allow us to select neutrinos from μDAR. This can be easily achieved by gating out for about $1\mu s$ from the start of the proton beam spill. This eliminates neutrinos from pion and kaon decay-in-flight.

(2) Due to nuclear absorption of π^- and μ^-, neutrinos from μ^- decay are suppressed to about the 10^{-3} level. The resulting neutrino beam is predominantly ν_e and $\bar{\nu}_\mu$ from μ^+ with contamination from other neutrino species at the level of 10^{-3}.

(3) Neutrino cross sections are well known. $\bar{\nu}_e$ interacts by inverse β decay. The cross section is known to a few percent accuracy.

(4) The neutrino energy can be calculated from positron energy by adding $\sim$ 1.8 MeV.

(5) The $\bar{\nu}_\mu$ and ν_e fluxes have different and well defined spectra. This allows us to separate $\bar{\nu}_e$ due to $\bar{\nu}_\mu \rightarrow \bar{\nu}_e$ oscillations from those due to μ^- decay contamination.

We propose to proceed with the oscillation search in steps. The region of Δm^2 to be examined is large, i.e. a positive signal can be found anywhere between $sub - eV^2$ to several tens of eV^2. We would like to start by examining the large Δm^2 region, which can be done with short baseline. At close distance to the MLF target, a high neutrino flux is available and allows us to use relatively small detector.

If no definitive positive signal is found by this experiment, a future option exists to cover small Δm^2 region. This needs a relatively long baseline and requires a large detector to compensate for the reduced neutrino flux.

Contents

1   Physics Goals

In 1998 the Super-Kamiokande collaboration announced the observation of neutrino oscillations with atmospheric neutrinos [1, 2]. Oscillations have been observed also in accelerator [3], solar [4] and reactor [5] neutrinos since then. These observations are evidence of the fact that each neutrino flavor state is a super-position of mass states and that neutrino mass states have different masses, i.e. at least two non-zero values. For three flavors of neutrinos, three mass states exist. The relation between flavor and mass states can be described by a 3x3 Unitary matrix [6] and can be parametarized by three mixing angles, one Dirac and two Majorana phases.

From solar, atmospheric, accelerator and reactor experiments, the difference of square of masses have two distinct values, namely

$$m_2^2 - m_1^2 = (7.54 \pm 0.21) \times 10^{-5} eV^2, |\, m_3^2 - m_2^2 \,| = (2.42 \pm 0.12) \times 10^{-3} eV^2$$

There is no way to construct a mass squared difference to be very different from those numbers within three neutrino scheme.

In the last fifteen years, several experiments have reported neutrino phenomena, which are consistent with the existence of neutrino oscillations with $\Delta m^2 \geq eV^2$. If they are confirmed to be neutrino oscillations, it requires more than three mass states, and therefore, more than three kinds of neutrinos are required in nature. On the other hand, collider experiments have measured the number of neutrinos to be three by the measurement of the invisible width of the Z-boson, $Z \to \nu + \bar{\nu}$[7]. The fourth state, if it exists, is a new kind of lepton, which does not have electromagnetic or weak intearction, namely a sterile neutrino.

The standard three neutrio scheme is a minimal phenomenological extension of the Standard Model of particle physics, requiring a lepton mixing matrix that is analogous to the quark sector and non-zero neutrino masses. Despite its success, the present description of neutrino states does not address fundamental questions such as how many fermions exist in nature, why the neutrino sector has small masses and large mixing angles compared to the quark sector etc. There needs to be a critical test regarding whether the three generation neutrino scheme completes the discription of the lepton sector. In the quark sector, the three generation scheme has been tested extensively in term of the test of the unitarity triangle of the Kobayashi-Maskawa matrix.

One of the critical tests of the three neutrino scheme is to examine the existence of a 4th mass state beyond three generations of neutrinos. Sterile neutrinos are naturally present in many theories beyond the standard model [8], in particular in several manifestations of the seesaw mechanism. the number of fermion species is important not only in particle physics but also in cosmology. If the existence of the sterile neutrino is confirmed, the following implications follow.;

(1) The 3x3 active neutrino mixing matrix (PMNS matrix) is not unitary, and neutrino mixing involves at least 6 mixing angles and 6 phases, 3 of which are Majorana phases.

(2) The electron neutrino is a superposition of four neutrino mass eigen-states.

The direct mass measurements and the rate of neutrino-less double β decay must take into account the effect of the 4th neutrino state.

(3) Depending on the model of the early Universe, the existence of more than 3 light neutrinos influence the expansion rate of the early Universe.

(4) Depending on the nature of sterile neutrinos, possiblities for the existence of more species and thier masses and mixing are future subjects of investigation.

In this Proposal, we describe a short baseline neutrino experiment at the J-PARC 3 GeV MLF facility to search for sterile neutrinos.

2 Present status and the principle of measurement

2.1 Experimental status

Experimental evidence for sterile neutrinos would come from disappearance or appearance of active flavor with different Δm^2, which cannot be explained by Δm_{12}^2 or Δm_{23}^2. Table1 is the summary of observed anomalies and their significance.

Experiment	neutrino source	Signal	σ
LSND	π decay at rest	$\bar{\nu}_\mu \to \bar{\nu}_e$	3.8σ
MiniBooNE	π decay in flight	$\nu_\mu \to \nu_e$	3.4σ
MiniBooNE	π decay in flight	$\bar{\nu}_\mu \to \bar{\nu}_e$	2.8σ
Gallium/SAGE	e capture	$\nu_e \to \nu_x$	2.7σ
Reactor	β decay	$\bar{\nu}_e \to \bar{\nu}_x$	3.0σ

Table 1: Possible large Δm^2 anomalies

The first indication was reported by the LSND experiment. LSND reported an excess of $87.9\pm22.4\pm6.0$ $\bar{\nu}_e$ events (3.8σ) in 1998[9]. MiniBooNE results are presented recently. The MiniBooNE experiment observed excesses of $\nu_e, \bar{\nu}_e$ candidates in the 200-1250 MeV energy range in neutrino mode (3.4σ) and in anti-neutrino mode (2.8σ). The combined excess is $240.3 \pm 34.5 \pm 52.6$ events, which corresponds to 3.8σ [10]. It is not clear whether the excesses are due to oscillations. If they are due to oscillations, both LSND and MiniBooNE indicate a flavor conversion of $\bar{\nu}_\mu$ to $\bar{\nu}_e$ at a probability of about 0.003 with a Δm^2 of $\sim 1 eV^2$.

The second indication is a deficiency observed in the calibrations of low energy radio-chemical solar neutrino experiments. The results indicated a deficiency in neutrino event rates. Mono-energetic neutrino sources (^{51}Cr and ^{37}Ar) were used in these experiments. Their results were presented in terms of the ratio of the observed and the predicted rate. The predictions are based on theoretical calculations of neutrino cross sections by Bahcall and by Haxton. The quoted numbers are $R_{obs}/R_{pred} = 0.86 \pm 0.05(\sigma_{Bahcall}), 0.76 \pm 0.085(\sigma_{Haxton})$ [11].

The so-called reactor anomaly indicates a 6% deficit of detected $\bar{\nu}_e$ from nuclear

reactors at baselines less than 100 m. The ratio of observed and expected rate is 0.927 ± 0.023. This is entirely based on the re-analysis of existing data. The deficit is caused by three independent effects which all tend to increase the expected neutrino event rate. There have been two re-evaluations of reactor anti-neutrino fluxes and both indicate an increase of flux by about 3%. The neutron lifetime decreased from 887-899s to 885.7s and thus the inverse β-decay cross section increased by a corresponding amount. The contribution from long-lived isotopes to the neutrino spectrum was previously neglected and enhances the neutrino flux at low energies [12].

All these hints have a statistical significance around $3-3.8\sigma$ and may be caused by one or more sterile neutrinos with a mass of roughly 1 eV. If they are due to neutrino oscillation with new mass state $m_4(\sim eV)$, the disappearance and the appearance of active neutrinos are related by ($m_4 \gg m_{1,2,3}$ and $U_{s4} \sim 1 \gg U_{e\mu\tau,4}$.)

$$
\begin{aligned}
P(\nu_e, \nu_\mu \to \nu_s) &= -4 \sum_{i>j} Re(U_{si} U^*_{\mu,ei} U^*_{sj} U_{\mu,ej}) \sin^2 \Delta_{ij} \\
&\quad - 2 \sum_{i>j} Im(U_{si} U^*_{\mu,ei} U^*_{sj} U_{\mu,ej}) \sin 2\Delta_{ij} \\
P(\nu_\mu \to \nu_e) &= -4 \sum_{i>j} Re(U_{ei} U^*_{\mu i} U^*_{ej} U_{\mu j}) \sin^2 \Delta_{ij} \\
&\quad - 2 \sum_{i>j} Im(U_{ei} U^*_{\mu i} U^*_{ej} U_{\mu j}) \sin 2\Delta_{ij} \\
\Delta_{ij} &= (m_j^2 - m_i^2)L/4E_\nu
\end{aligned}
$$

For a short baseline experiments $(L(m)/E(MeV) \sim 1)$ and if only one sterile neutrino involved in mixing,

$$
\begin{aligned}
P(\nu_{e,\mu} \to \nu_s) &\sim -4 \sum_j Re(U_{s4} U^*_{\mu,e4} U^*_{sj} U_{\mu,ej}) \sin^2(m_4^2 L/4E_\nu) \\
&\quad - 2 \sum_j Im(U_{s4} U^*_{\mu,e4} U^*_{sj} U_{\mu,ej}) \sin 2(m_4^2 L/4E_\nu) \\
&= 4 \mid U_{s4} \mid^2 \mid U_{\mu,e4} \mid^2 \sin^2(m_4^2 L/4E_\nu) \\
P(\nu_\mu \to \nu_e) &\sim -4 \sum_i Re(U_{e4} U^*_{\mu 4} U^*_{ei} U_{\mu i}) \sin^2(m_4^2 L/4E_\nu) \\
&\quad - 2 \sum_j Im(U_{e4} U^*_{\mu 4} U^*_{ej} U_{\mu j}) \sin 2(m_4^2 L/4E_\nu) \\
&= 4 \mid U_{e4} \mid^2 \mid U_{\mu 4} \mid^2 \sin^2(m_4^2 L/4E_\nu)
\end{aligned}
\tag{1}
$$

Thus $P(\nu_\mu \to \nu_s) \cdot P(\nu_e \to \nu_s) \sim P(\nu_\mu \to \nu_e)$.

In order for the LSND and MiniBooNE data to be consistent with the sterile neutrino hypothesis, ν_μ disappearance at $\Delta m^2 \sim eV^2$ should exist in addition to the possible ν_e deficiencies, which has been observed in β source and reactor measurements. So far only several % level upper limit exists for ν_μ. Thus some tension exist

in this respect [13].

The indicated allowed regions are shown in Figure 1 for the appearance channel (left figure) ($\bar{\nu}_\mu \to \bar{\nu}_e$) and for the disappearance channel (right figure) ($\nu_e \to \nu_s$).
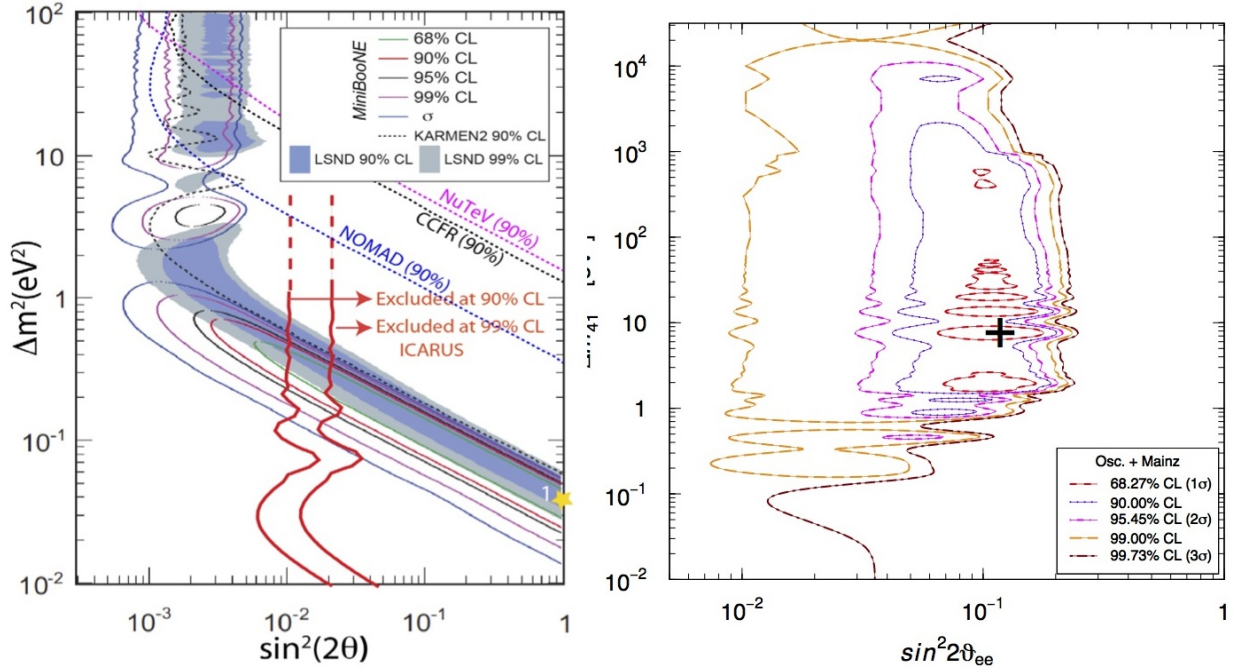
Figure 1: Left figure : Allowed region for $\bar{\nu}_\mu \to \bar{\nu}_e$ appearance channel as a result of combining LSND, MiniBooNE and ICARUS [14]. Right figure : Allowed region for disappearance channel with Reactor and β source anomalies, taken into account KATRIN and neutrino-less double β decay limits [15].

2.2 The principle of measurement

-Advantages of pion/muon decay at rest neutrino source

The measurement will be based on the following features of the μ Decay-At-Rest(DAR; $\pi^+ \to \nu_\mu + \mu^+$; $\mu^+ \to e^+ + \nu_e + \bar{\nu}_\mu$) beam at J-PARC MLF;

(1) Low duty factor of the pulsed proton beam.
(2) No decay in flight components by timing cut.
(3) Selection of the neutrino flavor by detecting Inverse Beta Decay (IBD; $\bar{\nu}_e + p \to e^+ + n$) signal in liquid scintillator.
(4) Well known different spectrum shapes for $\bar{\nu}_\mu$ and $\bar{\nu}_e$ from μ^- decay contamination.
(5) The IBD cross section is well measured in neutron β decay [16].
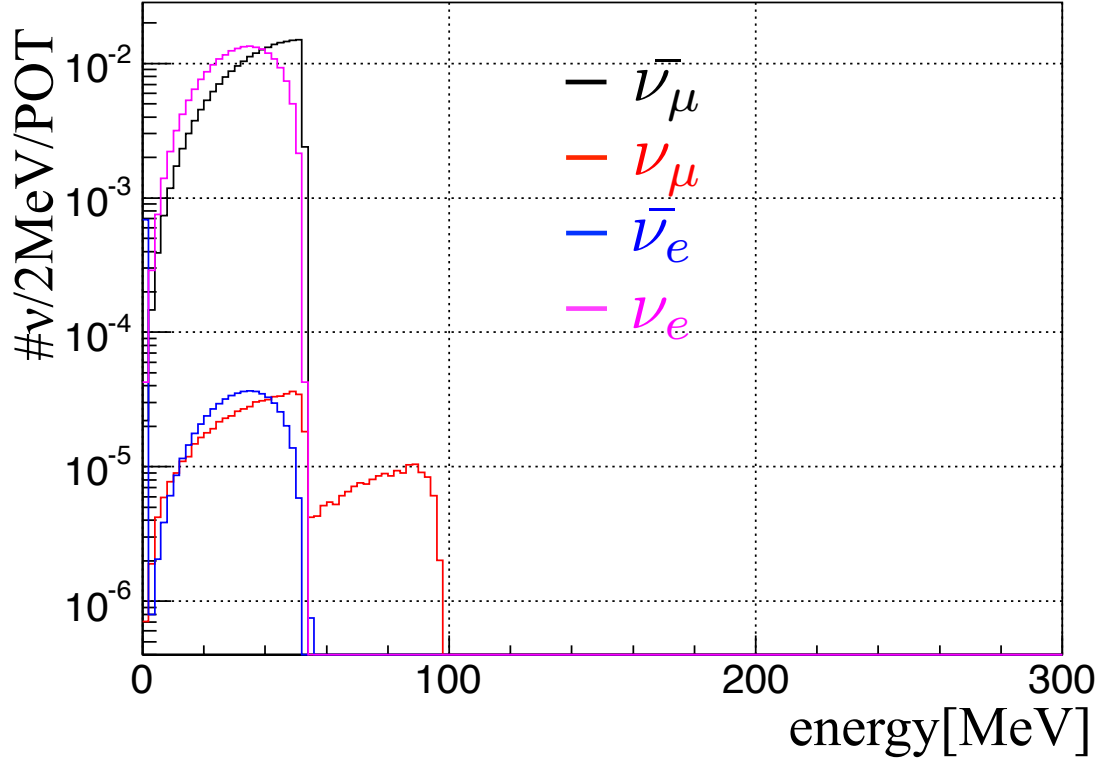
Figure 2: Estimated neutrino flux after 1 μs from the start of proton beam. The μ^+DAR components are selected and main background come from μ^- decays.

(6) Ease of E_ν reconstruction. : $E_\nu \sim E_e + 1.8$ MeV [2].
(7) The flux of $\bar{\nu}_\mu$ can be monitored by the rate of ν_e interactions.

2.2.1 Neutrino spectrum from decay at rest of μ^+

In this proposal, we concentrate on the neutrino beam from muon decay at rest (μDAR). To use neutrinos from pion and kaon decay at rest, extensive studies and experience in dealing with the backgrounds during the proton beam bunch will be needed.

The μDAR component can be selected by gating out the first 1 μs from the start of the proton beam. The resulting neutrino fluxes for each type of neutrino species are shown in Figure 2. Note that the resulting $\bar{\nu}_\mu$ and ν_e fluxes have different spectrum with endpoint energy of 52.8 MeV. A possible survived μ^- decay will be at the level of 10^{-3} and produce ν_μ and $\bar{\nu}_e$ with same spectrum as those of $\bar{\nu}_\mu$ and ν_e, respectively.

---

[2] Note that recoil neutrons carry kinetic energy up to 5 MeV where E_ν =50 MeV; however, the incident neutrino energy can be determined by the energy and angle of the positron.

2.2.2   Interactions of neutrino from μ^+ decay at rest

There are four kinds of neutrino interactions in scintillator detector (CH_2).

(1)Inverse beta decay (IBD)
The signal we are looking for is $\bar{\nu}_\mu \to \bar{\nu}_e$ and $\bar{\nu}_e + p \to e^+ + n$ with neutron capture γ as a delayed coincidence.

$$
\begin{aligned}
\sigma_{IBD} &= \frac{G_F^2 E_\nu^2}{\pi}(g_V^2 + 3g_A^2)\sqrt{1 - \frac{2Q}{E_\nu} + \frac{Q^2 - m_e^2}{E_\nu^2}}\theta(E_\nu - Q) \\
&\sim 9.3 \times 10^{-48}E_\nu^2(MeV)m^2
\end{aligned}
$$

(2)Charged current interaction of ν_e
$\nu_e +^{12}C \to e + N^*$. For N_{gs} final state, $N_{gs} - \beta$ decay gives a delayed coincidence as a clear signature with 17 MeV endpoint energy.

(3) Neutral current interaction with nucleus
All active neutrinos interact by neutral current interaction with nucleus; $\nu_{e,\mu} + X \to \nu_{e,\mu} + X')$. A dominant process in scintillator (CH_2) detector to produce an electro magnetic particle is
$\nu_{e,\mu} +^{12}C \to \nu_{e,\mu} + C(15.11)$ producing 15 MeV γ.

(4) Atomic electron target reaction
$\nu_{e,\mu} + e \to \nu_{e,\mu} + e$. These are negligible contribution.

Figure 3 shows the cross sections as functions of E_ν for each interaction.

2.2.3   Signatures of the oscillation

A sensitive search for $\bar{\nu}_e$ appearance ($\bar{\nu}_\mu \to \bar{\nu}_e$ from $\mu^+ DAR$) can be performed by searching for the two-fold signature of $\bar{\nu}_e + p \to e^+ + n$ scattering with a positron with 52.8 MeV endpoint energy followed by gammas due to Gd neutron capture.

The main background coming from μ^- decays as shown in Fig.2, is highly suppressed by π^- and μ^- capture in heavy metals like Hg. However, μ^-s, which stopped in a light metal such as Be, does usually decay before absorption. This background can be estimated from the E_ν distribution, which is well defined and different from oscillated events.

Since the oscillation probability is given by

$$
P = \sin^2 2\theta \sin^2(\frac{1.27\Delta m^2(eV^2)L(m)}{E_\nu(MeV)})
$$

, there are two distinct signatures of oscillation signal. One is the energy spectrum of the oscillated signal, which is a convolution of the energy spectrum of the original neutrino (in this case, $\bar{\nu}_\mu$) and the oscillation probability. The other signature is the
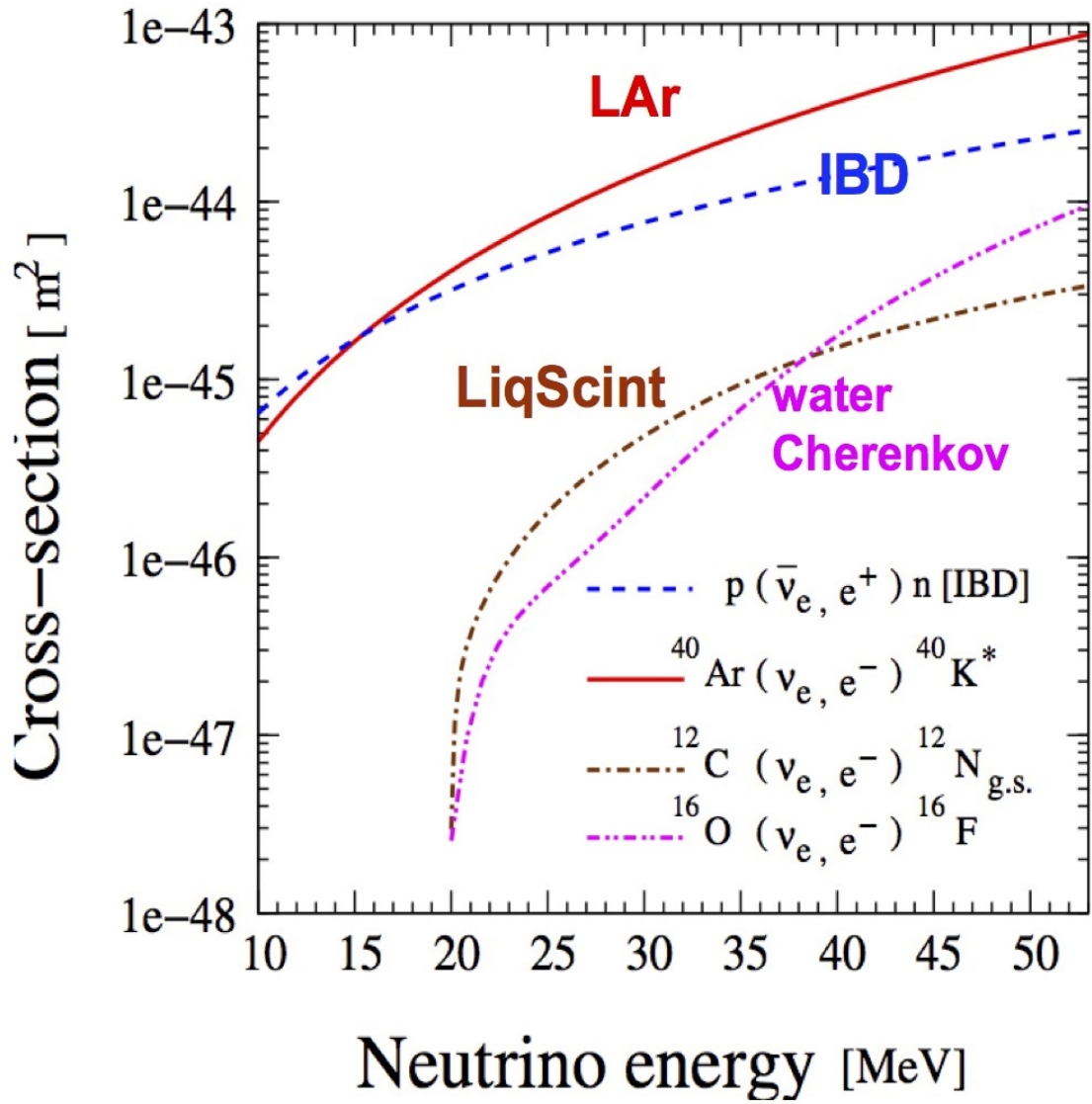
Figure 3:   Cross sections for IBD and $^{12}\mathrm{C}(\nu_e,e^-)^{12}\mathrm{N}_{g.s.}$ are shown as a function of E_ν [17].
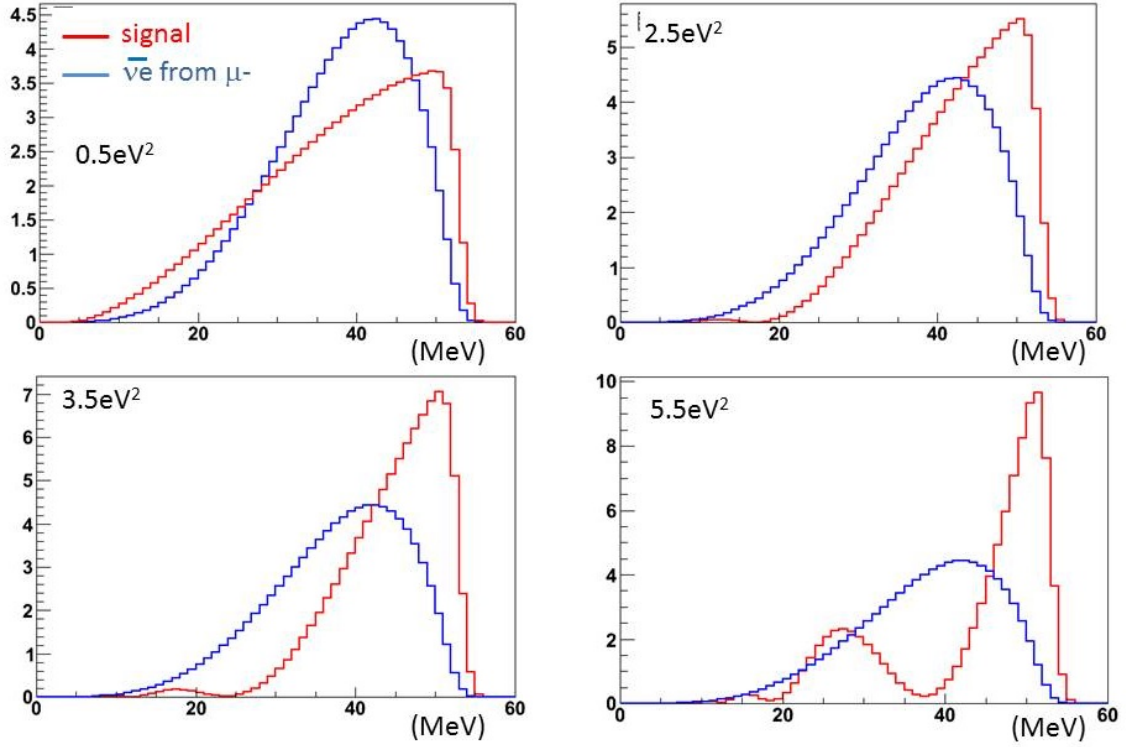
Figure 4: Examples of oscillation signals at typical Δm^2 for a baseline of 17 m. The red graphs are shapes of $\bar{\nu}_e$ appearance signal and the blue graphs are shapes of signal from μ^- decays. Energy is smeared by $15\%/\sqrt{E}$, which is the assumption of the energy resolution of the detector. All plots are normalized by area.

distribution of events as a function of distance from the source. The background $\bar{\nu}_e$ from μ^- decay has a different spectrum from that of $\bar{\nu}_\mu$ oscillations. Figure 4 shows oscillation signals at some typical Δm^2s for a baseline of 17 m.

2.2.4 Signal identification

The signal for $\bar{\nu}_e$ appearance from $\bar{\nu}_\mu \to \bar{\nu}_e$ is a primary positron signal followed by delayed signal.

The primary signal is $\bar{\nu}_e + p \to e + n$ (Inverse Beta Decay (IBD)) and the delayed signal is the neutron capture gamma. For the normalization of μ^+ decay, $\nu_e + C \to e + N_{gs}$ events will be measured. The primary signal is an electron and the delayed signal is a positron from N_{gs} β decay.

The time gate for the primary signal should be from 1μs to 10μs, corresponding to the muon lifetime and avoiding pion decay from both decay at rest and decay in flight. Table 2 is a summary of primary and delayed signal.

	primary timing	primary energy	delayed timing	delayed energy
$\bar{\nu}_\mu \to \bar{\nu}_e$	1-10 μs	0-53 MeV	10-100μs	8 MeV
$\nu_e C \to e N_{gs}$, $N_{gs} \to C e^+ \nu_e$	1-10 μs	0-37 MeV	100μs-10 ms	0-16 MeV

Table 2: The expected signal timing relative to proton beam bunch and signal energy

2.3 Strategy of this experiment

We select a strategy to put a detector with 50 tons of liquid scintillator using a short baseline ($\sim$ 17 m; the third floor of the MLF, maintenance area of the target. See section 5.1 for more details.) for the following reasons;

1. The distortion of the neutrino energy spectrum is clear in the $\Delta m^2 > 2.0$ eV^2 region if neutrino oscillations exist as shown in Fig. 4.

2. This short baseline provides a large number of events due to 1/L^2 law from the target, i.e., the neutrino flux is reduced as a function of 1/L^2.

3. As a result, the sensitivity to search for sterile neutrinos above the few eV^2 region is comparable to or better (see Fig. 5) than the experiment using a larger detector at a longer distance.

If no definitive positive signal is found by this configuration, a future option exists to cover the small Δm^2 region. This needs a relatively long baseline and requires a large detector to compensate for reduced neutrino flux (see appendix).

3 The J-PARC MLF as a DAR Neutrino Source

Neutrino beam from stopped pion decay from the J-PARC Rapid Cycling Synchrotron (RCS) is one of the best suited facilities for searches of neutrino oscillations in the mass range $\Delta m^2 \sim eV^2$, because of the following reasons:
(1) available beam power
(2) mercury target absorbs μ^- and suppresses free decay,
(3) short duty factor of the pulsed beam enables us to eliminate decay-in-flight components and to separate μDAR from other background sources, and the resulting $\nu_e, \bar{\nu}_e$ have well defined spectrum and well defined cross section.

3.1 The RCS beam and the target

The proton intensity is expected to reach 0.33 mA (1 MW) after major upgrades of the accelerator. The protons are produced with a repetition rate of 25 Hz, where each spill contains two 80 ns wide pulses of protons spaced 540 ns apart. 1 MW beam
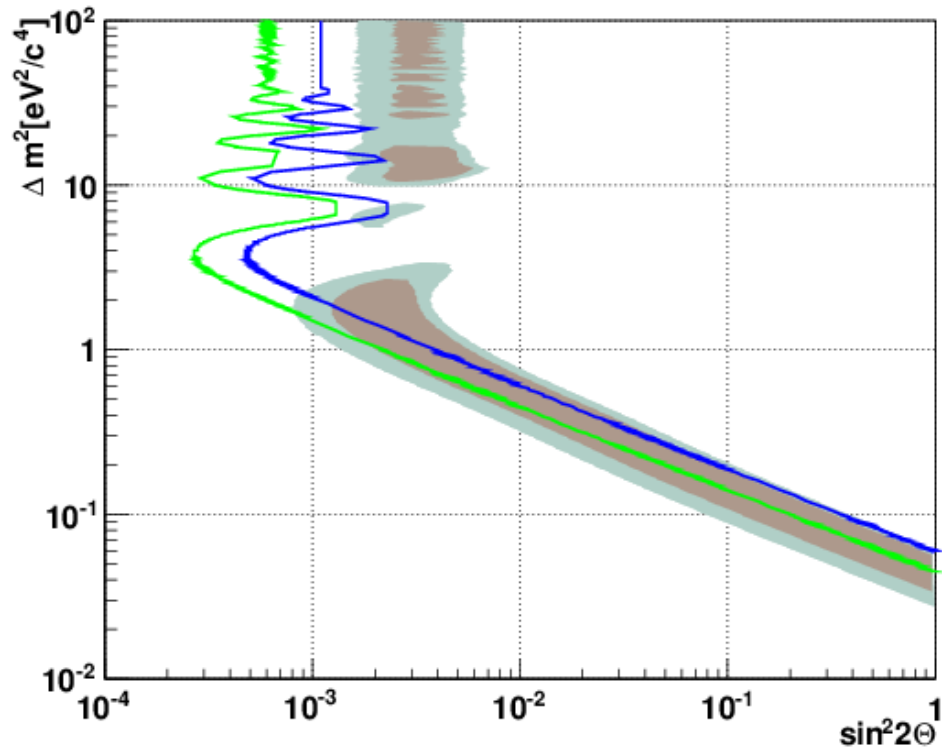
Figure 5: The sensitivity of the MLF experiment assuming 4 years operation (4000 hours / year) assuming the ∼50% detection efficiency and a 17 m baseline. The blue line shows the 5 σ C.L., while green one corresponds to 3 σ.

14

provides 3×10^{22} protons-on-target (POT) during 4000 hours / year operation (i.e.; 3.6×10^8 spills are provided during one year). The short pulsed beam (540 ns, 25 Hz) provides the ability to distinguish between neutrinos from pion decay and those from muon decay.

Figure 6 shows a plan view of Materials and Life Science and Experimental Facility (MLF) in J-PARC. After penetrating a muon production target made of carbon graphite of 2 cm thickness, protons are introduced to a mercury target. A schematic drawing of the J-PARC spallation neutrino source is shown in Figure 6. 3 GeV protons interact in the mercury spallation target, producing pions and kaons that decay into ν_e and ν_μ and their anti-neutrinos after heavy shielding. Surrounding the target are cooling pipes, beryllium reflectors, and steel shielding.

A beam of protons enters from the left and strikes the target. The beam has a wide spot size such as 3.3 cm by 1.3 cm in root mean square (rms) for reduction of the local heat load in the target. The target, shown in Figure 7, has dimensions of 54 cm in width by 19 cm in height by 210 cm in length. Mercury is contained within a multiple wall structure made of stainless steel. To remove heat, the mercury of the target is constantly circulated at a rate of 154 kg/sec. The cryogenic liquid hydrogen moderators are located at the top and bottom of the target. Target and moderators are surrounded by a beryllium reflector and an iron shielding which extends at least to a radius of 5 meter around the target. There are 23 neutron channels looking at the moderators, rather than at the target. Shutters are provided on each channel.

3.2   Neutrino Beam

There are two time structures of the neutrino beam.
One is 'On-bunch' (neutrinos produced during proton bunch and pion or kaon lifetime).

- $\pi^+ \rightarrow \mu^+ \ \nu_\mu$ decay at rest with monochromatic neutrino energy of 30 MeV

- $\mu^- + A \rightarrow \nu_\mu + A$ with end point at 105 MeV

- $K^+ \rightarrow \mu^+ \ \nu_\mu$ decay at rest with monochromatic energy of 236 MeV

- $K^+ \rightarrow \mu^+ \ \pi^0 \ \nu_\mu$ decay at rest with a end point energy of 215 MeV

- $K^+ \rightarrow e^+ \ \pi^0 \ \nu_e$ decay at rest with end point energy at 228 MeV

- Small components from π and K decay in flight

The other is 'Off-bunch' (during muon lifetime) component, which is produced by muon decay at rest.

- $\mu^+ \rightarrow e^+ \ \nu_e \ \bar{\nu}_\mu$

- If μ^- stop in a light material, μ^- also decay partially by $\mu^- \rightarrow e^+ \ \bar{\nu}_e \ \nu_\mu$
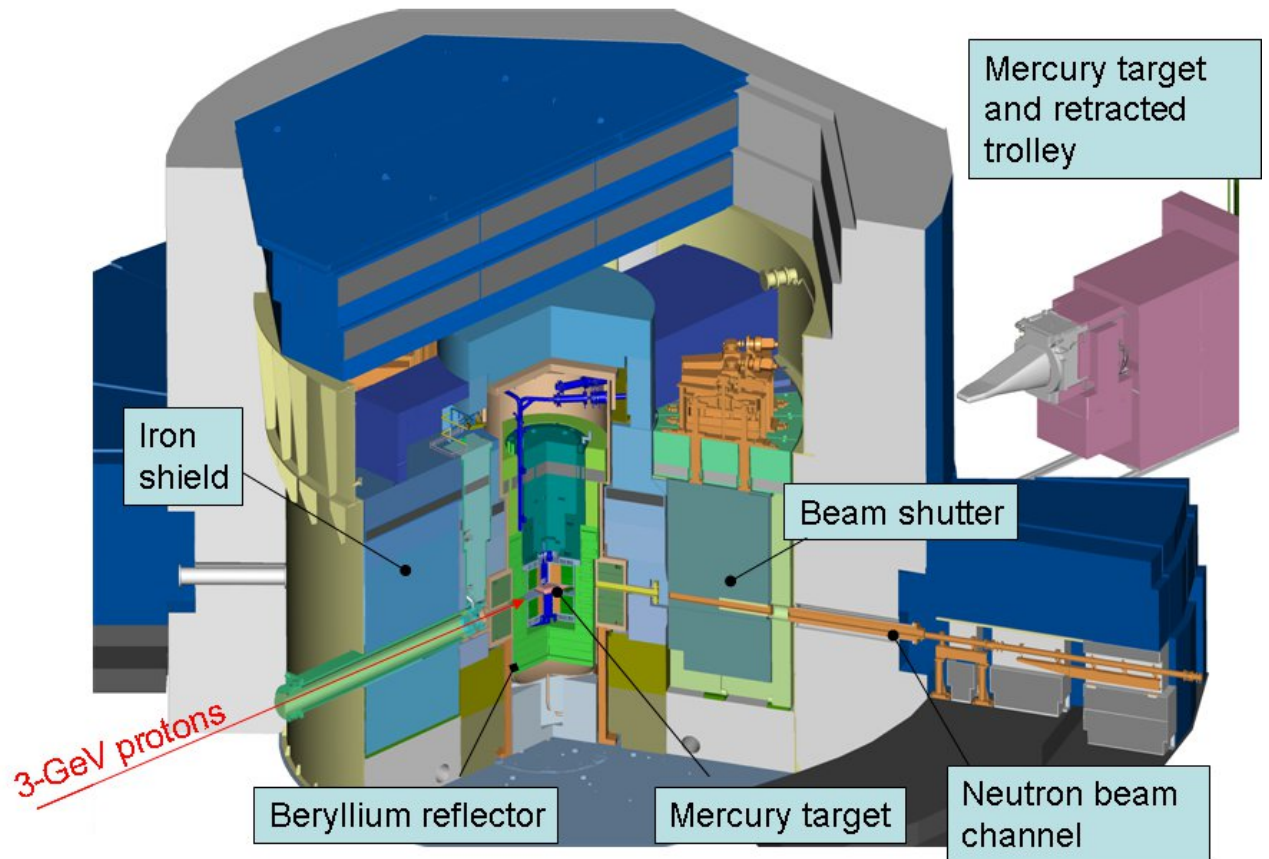
Figure 6: A schematic view of the MLF facility in J-PARC.
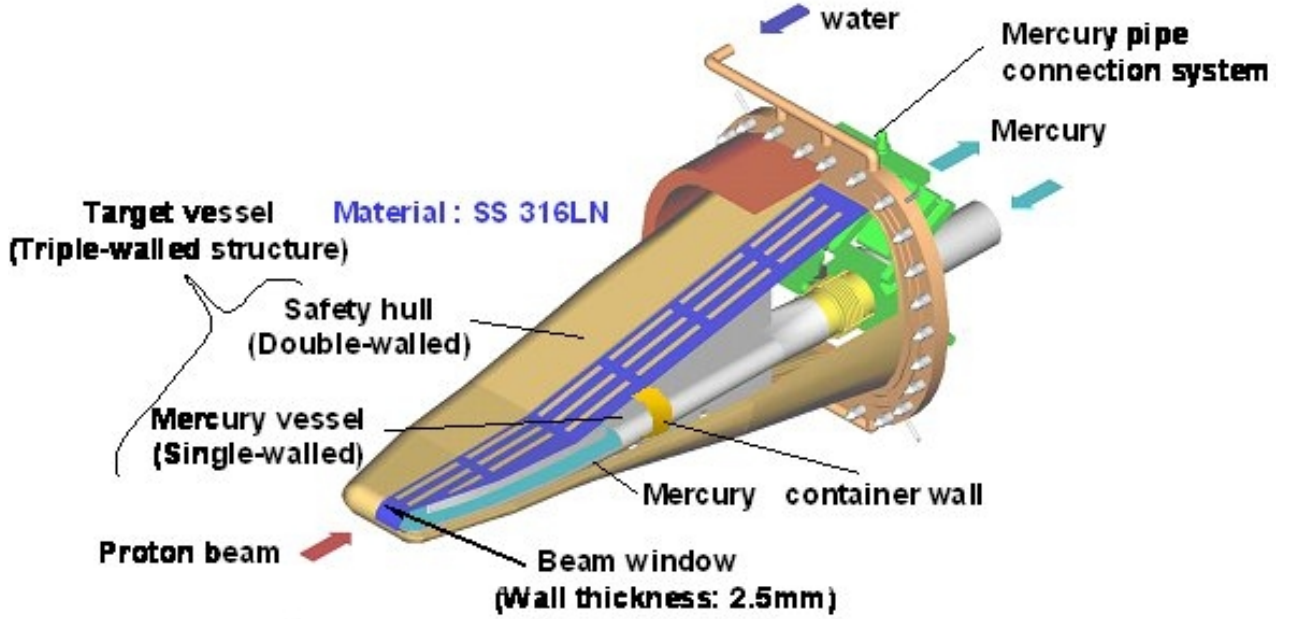
Figure 7: A schematic drawing of the mercury target in the J-PARC.

These can be selected by gating out the first 1 μsec from the start of the proton beam. Figure 8 shows the expected neutrino spectrum from MLF target (top) and time distributions from various sources (bottom). In this proposal, we concentrate on neutrino beam from muon decay at rest. With extensive studies and experience in dealing with the backgrounds during the proton beam, neutrinos from pion and kaon decay at rest may become usable.

The μ decay at rest neutrino beam was simulated by the following steps. Table 3 and 4 are summary tables for the production of neutrinos from μ decays.

1. Particle production by 3 GeV proton
   The interaction of the 3 GeV proton beam with the mercury target and beam line components has been simulated with FLUKA [18] and QGSP-BERT (in Geant4 [19]) hadron interaction simulation packages.

2. $\pi^{\pm}$ interactions and decay
   After the production, both π^+ and π^- lose their energy mainly by ionization. In addition, they disappear by charge exchange reaction $\pi^{\pm}(n,p) \to \pi^0(p,n)$, $\pi^0 \to \gamma\gamma$. The survived π^+s stop and decay with 26 ns lifetime. On the other hand, the survived π^-s are absorbed by forming a π-mesic atom and get absorbed promptly. The decay-in-flight takes place with very suppressed rate of about $\sim 8 \times 10^{-3}$ of produced $\pi^{\pm}$s.

3. $\mu^{\pm}$ absorption and decay
   All μ^+ decay by $\mu^+ \to e^+\nu_e\bar{\nu}_\mu$. Because of the muon lifetime and energy loss process, the decay-in-flight is negligible. μ^- is captured by nucleus by forming a mu-mesic atom and eventually produce ν_μ with an end point energy of 100 MeV. The absorption rate depends on the nucleus and becomes faster for heavier

17

Figure 8: The yield estimation of neutrinos from pion and kaon decays which are based on Geant4 [19] calculations (top). This tends to be at the low end of estimates of various particle production models. Time distribution of neutrinos from pion, muon and kaon decays is shown in the bottom plot. Neutrino beams from muon decay at rest only survive after 1 μsec from the start of proton beam.
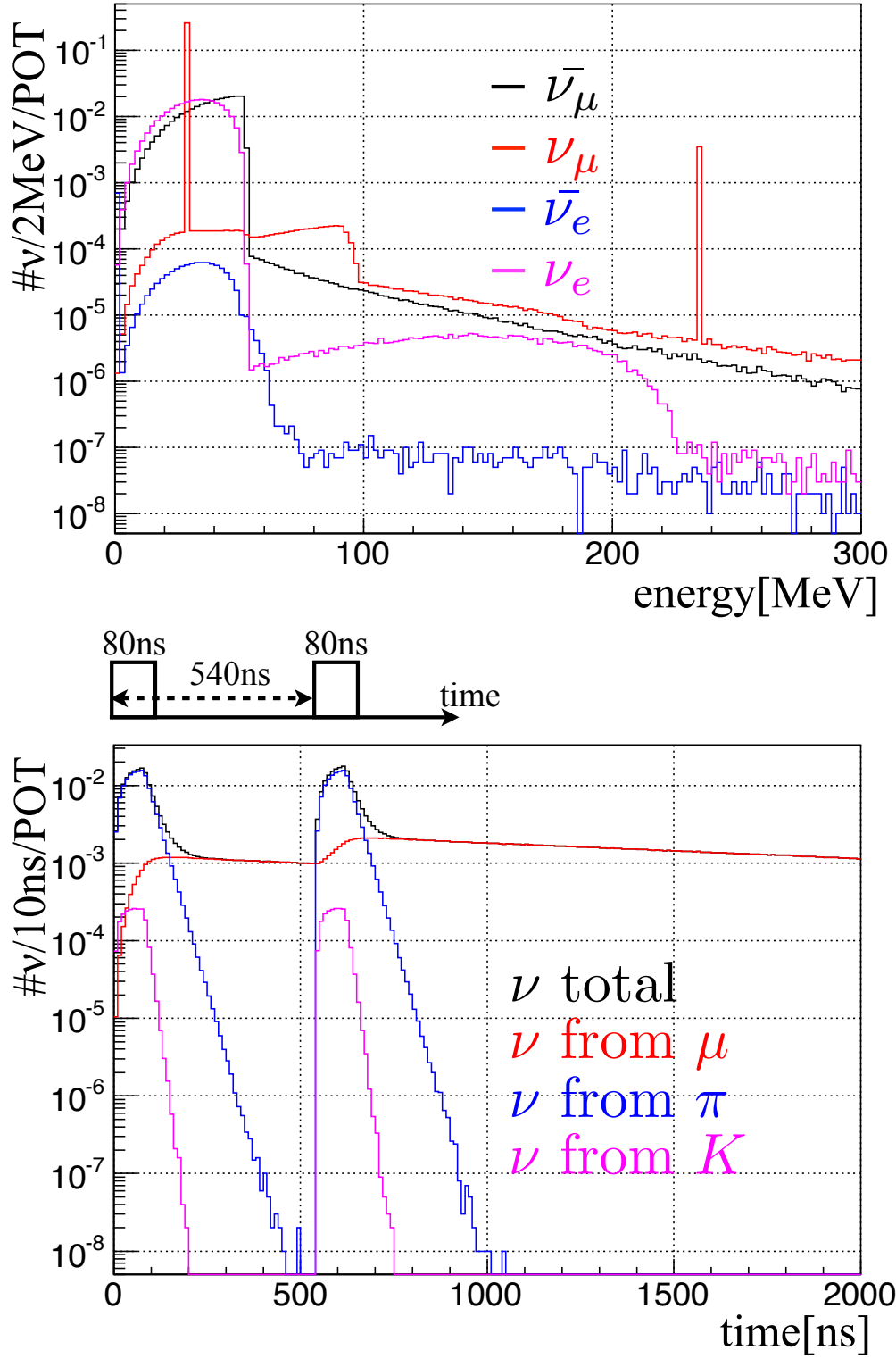
nuclei. The total nuclear capture rates for negative muons have been measured in terms of effective muon lifetime.[20]

The resulting neutrino fluxes for each type of neutrino species are shown in Figure 2, which has been already shown previously. Tables 3 and 4 are examples of expected production rates of $\pi^{\pm}$ by 3 GeV protons on mercury target and resulting μ^+ and μ^- decay neutrino per proton, based on a pion production model.

	$\pi^+ \to \mu^+ \to \bar{\nu}_\mu$	$\pi^- \to \mu^- \to \bar{\nu}_e$
π/p	6.49×10^{-1}	4.02×10^{-1}
μ/p	3.44×10^{-1}	3.20×10^{-3}
ν/p	3.44×10^{-1}	7.66×10^{-4}
ν after 1μs	2.52×10^{-1}	4.43×10^{-4}

Table 3: Summary of an estimate of μDAR neutrino production by 3 GeV proton by FLUKA hadron simulation package.

	$\pi^+ \to \mu^+ \to \bar{\nu}_\mu$	$\pi^- \to \mu^- \to \bar{\nu}_e$
π/p	5.41×10^{-1}	4.90×10^{-1}
μ/p	2.68×10^{-1}	3.90×10^{-3}
ν/p	2.68×10^{-1}	9.34×10^{-4}
ν after 1μs	1.97×10^{-1}	5.41×10^{-4}

Table 4: Summary of an estimate of μDAR neutrino production by 3 GeV protons by QGSP-BERT hadron simulation package.

Needless to say, there are many sources of ambiguities in pion production, for example production by secondary particles in thick target, target geometrical modeling, and pion production from mercury. We use these calculations as estimates and the actual μ^- backgrounds should be determined from the data based on their known spectrum and known cross section (see section 7.1).

For this proposal, numbers from Table 3 are used to estimate the central values, and those in Table 4 are used for the cross checks.

3.3   Estimated neutrino event rates

The estimated neutrino event rates (50 tons of total fiducial mass, 4 years measurement) is shown in Tables 5. The proton intensity is assumed to be 0.33 mA, delivering 3×10^{22} protons on target (POT) per 4000 hour operation in one year. The stopping ν/p ratio is estimated from FLUKA simulations to be 0.344. The $\bar{\nu}_\mu$ flux from the $\pi^+ \to \mu^+ + \nu_\mu \to e^+ + \nu_e + \bar{\nu}_\mu$ chain at 17 m is then equal to $1.9 \times 10^{14} \nu$ year/cm^2. The event reconstruction efficiencies are assumed to be 100 % for all processes here.

Reactions	XS (cm^2) averaged by energy	Events	Comment
$\bar{\nu}_e p \rightarrow e^+ n(\mu^+)$	9.5×10^{-41}	1690	$\Delta m^2 = 3.0 eV^2$ $sin^2(2\theta) = 3.0 \times 10^{-3}$ (Best Δm^2 for MLF exp.)
		703	$\Delta m^2 = 1.2 eV^2$ $sin^2(2\theta) = 3.0 \times 10^{-3}$ (Best fit values of LSND)
$\bar{\nu}_e p \rightarrow e^+ n(\mu^-)$	7.2×10^{-41}	804	FLUKA (shown in Table 3)
$\nu_e + {}^{12}C \rightarrow e^- + {}^{12}N_{gs}$	8.9×10^{-42}	22934	
$\nu_e + {}^{12}C \rightarrow e^- + {}^{12}N^*$	$4.3 \times 10^{-42} E_\nu^2$	11008	

Table 5: Number of neutrino events with 50 tons of total fiducial mass times 4 years operation.

4 Backgrounds Studies

4.1 Overview and brief summary of this section

As described in Section 2.2.4, we use inverse β-decay (IBD; $\bar{\nu}_e + p \rightarrow e^+ + n$) to detect $\bar{\nu}_\nu \rightarrow \bar{\nu}_e$ oscillations. The neutron from IBD is thermalized in detector material and captured by a nucleus, and afterwards the nucleus emits a gamma(s). The signature of the $\bar{\nu}_e$ signal is thus the coincidence of an e^+ as a 'prompt signal' and gammas by the neutron capture[3] as a 'delayed signal'.

Beam associated and natural sources of backgrounds (gammas, neutrons etc.) can mimic the prompt and delayed signals. To estimate amount of background at the detector location (the 3rd floor of MLF), we carried out background measurements in one of the MLF beam lines, BL13. In addition to gammas and neutrons as backgrounds for delayed signal, Michel electrons from muon decays were observed as a background for prompt signal. Following are the results of measurements:

- Michel electrons made by fast neutrons ($n + p \rightarrow X + \pi^\pm$, then $\pi^\pm \rightarrow \mu^\pm \rightarrow e^\pm$) are observed as an "IBD prompt" background. Probability of the fake prompt signal made by Michel electrons is 5.6×10^{-4} /spill/ton/300 kW/9 μs (1< t[μs] <10).

- Gammas ($6 < E[\text{MeV}] < 12$) made from neutron captured around the 1 ton detector, which is the background of "IBD delayed" signal, are observed. Total amount of the background is 0.9 /spill/ton/300 kW/100 μs.

- The amount of the neutrons below 1 MeV are also estimated by the detector. Total amount of the background is 14 /spill/ton/300 kW/100 μs.

The expected amount of background at the 3rd floor was then extrapolated by using the MC predictions at both BL13 and the 3rd floor. The background rates at

---

[3]The neutron capture reaction by Gd releases a sum of 8-MeV energy in a cascade of 3-4 gammas.

the 3rd floor at the surface of the supposed detector described in Section 5 with 1 MW beam power, are estimated as follows;

- Michel electrons at the 3rd floor is 2×10^{-7} /spill/detector/MW/9 μs.

- Total amount of gammas ($6 < E[\text{MeV}] < 12$) is 14 /spill/detector/MW/100 μs.

- Total amount of neutrons ($E < 1$ MeV) is 40 /spill/detector/MW/100 μs.

By taking the probability of the backgrounds coming to the fiducial volume in the detector into account (see Section 6.3), these values are low enough to observe the oscillated $\bar{\nu}_e$ signals by IBD at the 3rd floor.

4.2   Measurements at BL13

Figure 9 shows the top view of BL13 beam line. The amount of background was
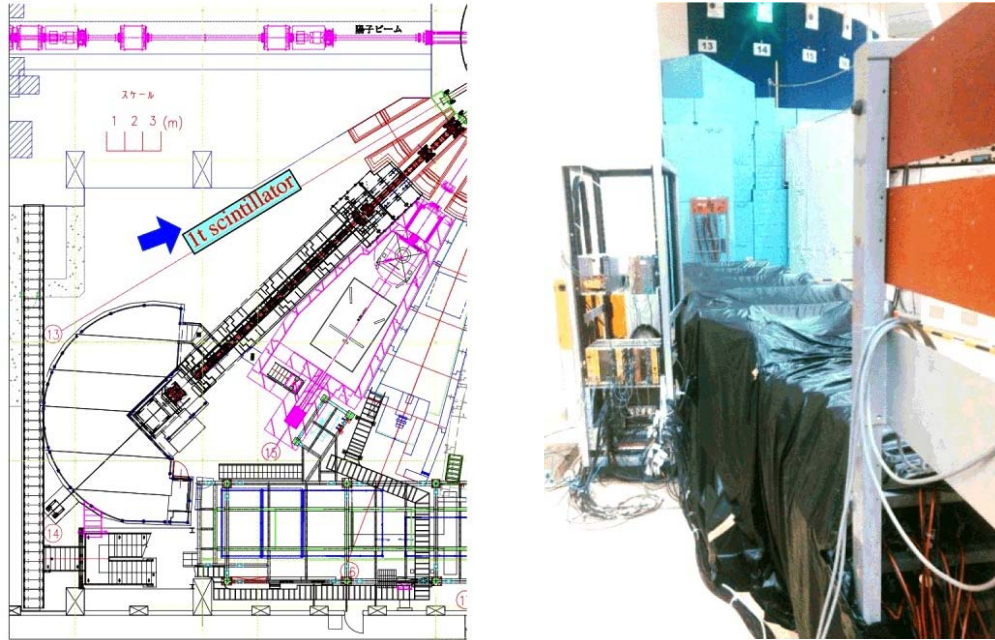
Figure 9: Top view of the BL13 and the location of the scintillator detector (left), and a photograph of the scintillator detector at BL13 (right). This photograph was taken at the blue arrow shown in the left figure.

measured with a one-ton scintillator detector and 370g NaI during 300kW beam operation and beam-off.

We placed a plastic scintillator detector at BL13 in MLF. The target mass of the detector was 1 ton. The details of the detector are described in Appendix A.2. Figure 10 shows the correlation between energy and timing of the observed activities. The two bunch structure of the RCS proton beam was clearly seen as the groups of the activities.

We also placed a NaI detector at BL13. The details of the NaI detector are described in Appendix A.3.
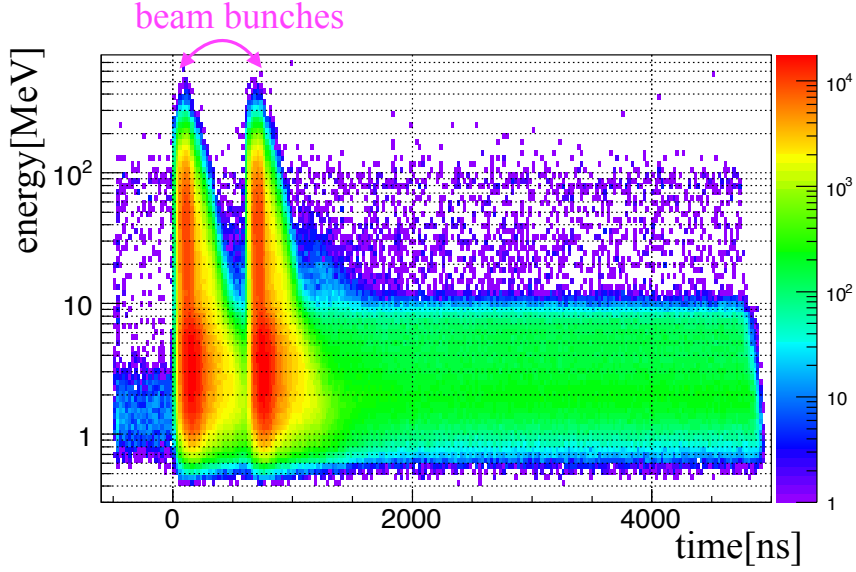
Figure 10: 2D plot for energy (vertical) and timing of the activities (horizontal) observed with the 1 ton scintillator detector placed at BL13. The clear two bunch structure of the RCS proton beam is seen.

4.2.1 Backgrounds for the prompt signal at BL13

Michel electrons were observed as a background for prompt signal. Figure 11 shows the timing distribution from the first bunches for the activities: $20 < E[\mathrm{MeV}] < 60$. We fitted the distribution with the function:

$$f(t) = A \exp\left(-\frac{t}{\tau}\right) + B, \tag{2}$$

where A (B) is the amount of the time dependent (independent) term and τ is the lifetime of the activities. When we fixed the time independent term, B, with the estimated value from Beam-off data, we obtained $\tau = 2.3 \pm 0.4\ \mu$s and it is consistent with the muon lifetime.

Figure 12 shows the energy distributions of the activities just after beam bunches and during Beam-off with and without the cosmic-muon veto[4]. The distributions above 60 MeV are consistent with each other between Beam-on and Beam-off, and activities below 60 MeV remain even with the cosmic-muon veto. Figure 13 shows

---

[4]As shown in Figure 40, the 1 ton detector consists of 24 pieces of plastic scintillators. Pairs of scintillators on the top, bottom, and both horizontal sides, surrounding scintillators in the middle, were used as cosmic-muon veto counters. Activities associated with the scintillators in the second row from top and bottom of the detector were also vetoed.

Figure 11: Timing distribution from the 1st bunches for the activities: $20 < E[\text{MeV}] < 60$. The distribution was fitted with the Equation 2 (red line). The constant (time-independent) term was estimated with Beam-off data (b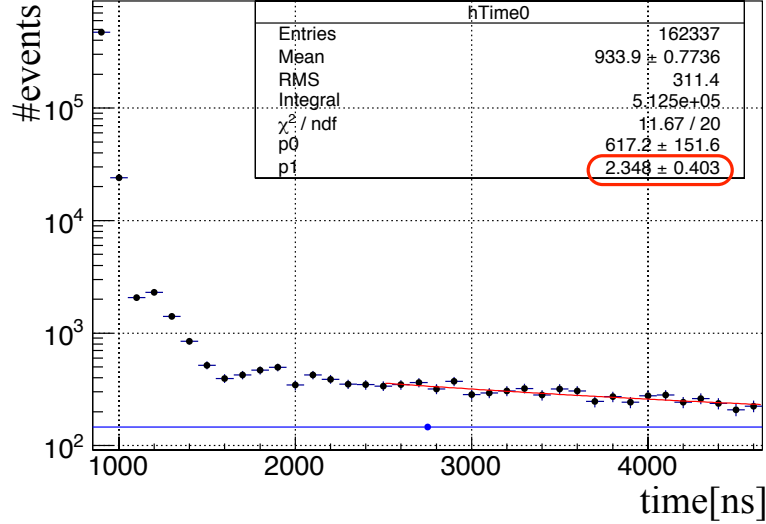lue line with a dot). The lifetime of the activities is $\tau = 2.3 \pm 0.4$ μs and is consistent with the muon lifetime.

the timing distribution from the 1st bunches for the activities: $20 < E[\text{MeV}] < 60$ with the cosmic-muon veto. The distribution later than 1500 ns is still consistent with Michel electrons from muon decays and time independent activities estimated from Beam-off data even with the cosmic-muon veto. The activities before 1500 ns will be investigated with the measurement at the detector location.

We investigated the correlation between those 'prompt-like' activities and activities on bunch timings. For comparison, we first made two samples: correlated and uncorrelated samples. The first sample contains pairs of a 'prompt-like' activity and an activity on bunch timing at the same beam spill. The other one contains pairs of a 'prompt-like' activity and an activity on bunch timing at the next beam spill. We then calculated the spatial distance between the activities for each pair. Figure 14 shows the spatial distance distributions for both correlated and uncorrelated samples. A clear enhancement was seen within the distance of 30 cm for the correlated sample. By rejecting the prompt candidate which has an activity around itself on bunch timing, the Michel electron background is supposed to be suppressed. The rejection power of this cut will be discussed in Section 6.3.2.

These results indicated that muons hit the scintillators on bunch timing and generated the Michel electrons. There are two possibilities of the muon source.

- Muons directly coming from outside of the scintillators.

- Fast neutrons coming on bunch timing hit scintillators and produced pions, and the muons were from those pion decays. Neutrons whose kinetic energy are larger than about 200 MeV can produce charged pions as shown in Figure 15.

If the first case, we can easily reject such events by surrounding the detector with veto
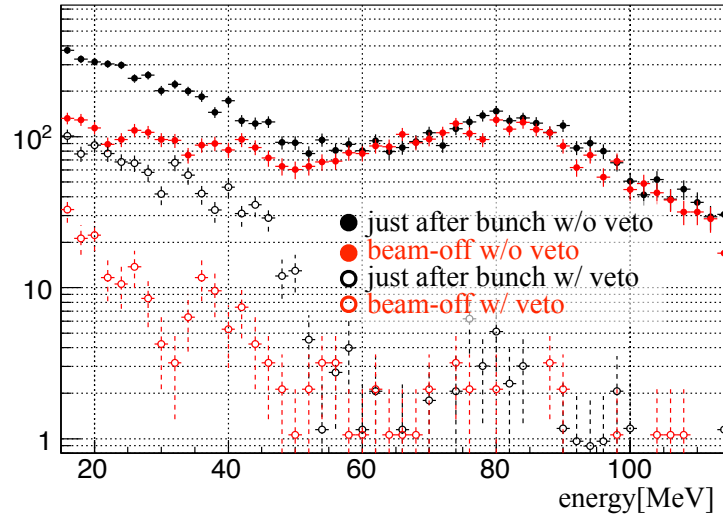
Figure 12: Energy distributions of the activities just after beam bunches and during Beam-off with and without the cosmic-muon veto. The distributions above 60 MeV are consistent with each other between Beam-on and Beam-off, and activities below 60 MeV remain even with the cosmic-muon veto.
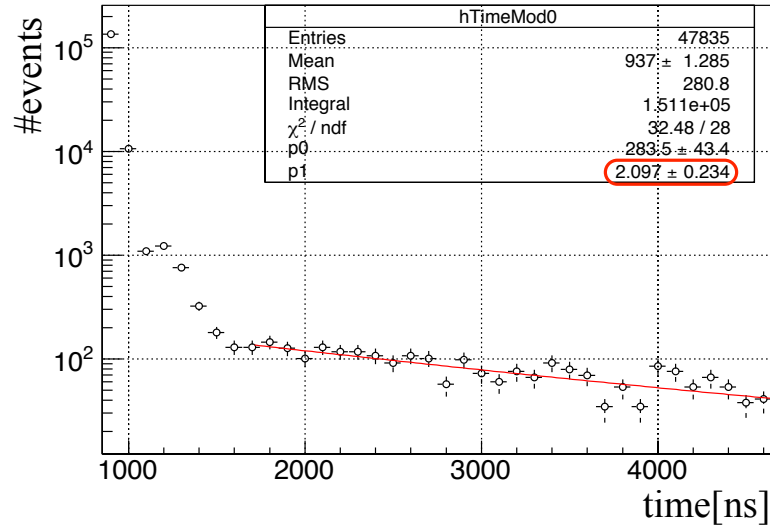
Figure 13: Timing distribution from the 1st bunches for the activities: $20 < E[\text{MeV}] < 60$ with the cosmic-muon veto. The distribution was fitted with the exponential plus constant (red line). The constant (time-independent) term was estimated with Beam-off data (~ 10). The lifetime is also consistent with the muon lifetime.

24
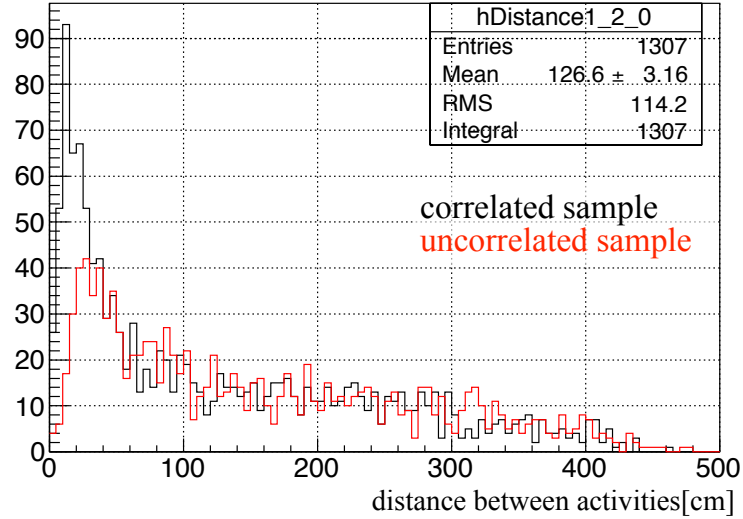
Figure 14: Spatial distance distributions for both correlated (black) and uncorrelated (red) samples. A clear enhancement was seen within the distance of 30 cm for the correlated sample.

counters. If the latter case, it is not obvious how well we can suppress such events. We thus supposed that the Michel-electrons are from $\pi \to \mu \to e$ decay induced by fast neutrons, and allocated the number of observed events itself to the background source for $\bar{\nu}_e + p \to e^+ + n$.

The number of observed Michel electron events with the 300 kW beam at BL13 was equivalent to 5.6×10^{-4} /spill within the time window, $1 < t[\mu s] < 10$, without the spatial distance cut described above.

4.2.2 Backgrounds for the delayed signal at BL13

Backgrounds for delayed signal after 1 μs from the first beam bunch were also measured with the 1 ton scintillator detector. Because of the 1 μs delay, the observed activities are dominated by neutron-capture related events. There are two types of backgrounds for delayed signal.

- Gammas by neutron captures in the materials outside of the detector. The gammas directly hit the detector from outside and mimic gammas by neutron captures in the detector.

- Neutrons which are captured in the detector and emit gammas at the end.

We measured each background level at BL13.

Gammas

Because the energy deposit for thermal neutron capture in the scintillators is 2.2 MeV, the activities with energy deposit $6 < E[\text{MeV}] < 12$ were assumed to be gammas.
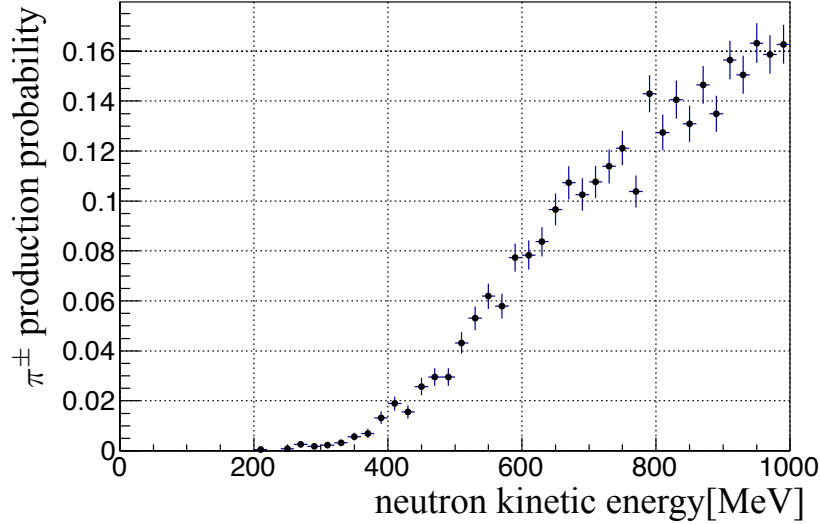
Figure 15: Production probability of charged pions as a function of kinetic energy of incident neutrons. The production target was a plastic scintillator. The values were estimated with MC simulation. Neutrons whose kinetic energy are larger than about 200 MeV can produce charged pions.

We found the activities have some effective lifetime and thus measured the lifetime of those activities. Figure 16 shows the energy distributions for each period of time, and the relative rate of gammas for each period is shown in Figure 17. We fitted the curve with the Equation 2 and obtained $\tau = 112.7 \pm 11.92$ μs.

The number of observed events with 300 kW beam at BL13 was equivalent to 7×10^4 /day within 5 μs window after the beam bunches. By considering the efficiency and the effective lifetime curve described above, the expected number of events within 100 μs window after the beam bunches was equivalent to 0.9 /spill with the 300 kW beam.

Neutrons

As described above, these neutrons were detected as thermal neutrons at the end. Because the energy deposit for thermal neutron capture in the scintillators is 2.2 MeV, we evaluated the amount of these neutrons by counting activities with the energy deposit $1 < E[\text{MeV}] < 4$.

We measured the effective lifetime of those activities. The relative event rate for each period of time is shown in Figure 18. We fitted the curve with the Equation 2 and obtained $\tau = 185 \pm 23$ μs.

The number of observed events with the 300 kW beam at BL13 was equivalent to 6×10^5 /day within 5 μs window after the beam bunches. By considering the efficiency and the effective lifetime curve described above, the expected number of events within 100 μs window after the beam bunches was estimated to be equivalent to 14 /spill with the 300 kW beam for neutrons.
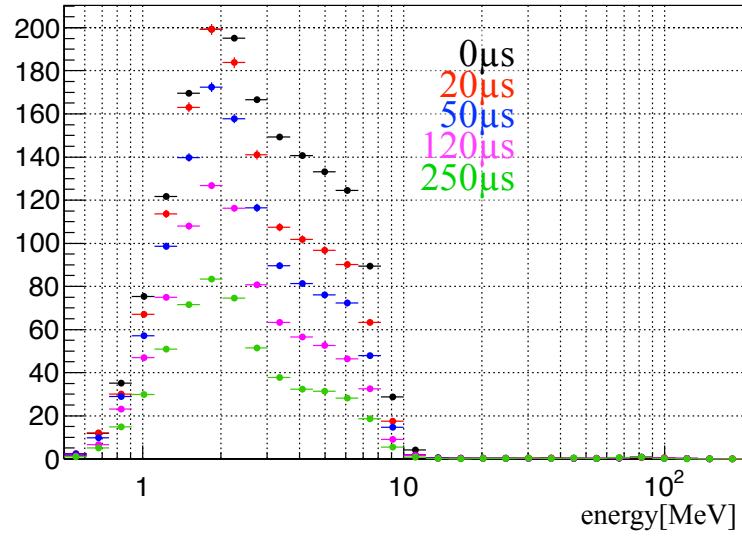
Figure 16: Energy distributions as a function of the gate delay. (the length of the time window of the FADC is fixed though). For example, "100 μs" means the FADC gate is opened from 100μs to 105.5 μs after the first bunch starting time. The black, red, blue, magenta and green dots show the energy distributions after the beam bunch, 20 μs, 50 μs, 120 μs and 250 μs later, respectively.
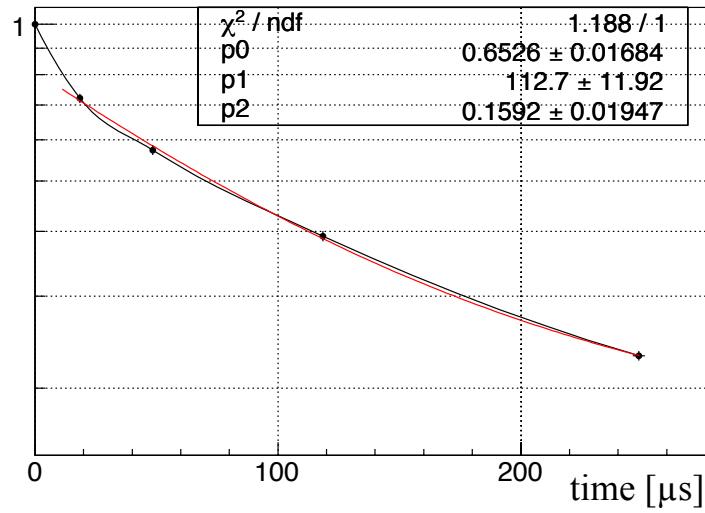
Figure 17: Relative rate of gammas with energy deposit $6 < E[\mathrm{MeV}] < 12$ as a function of the FADC gate delay. The curve was fitted with the Equation 2 (red line), which is , the exponential + constant term..

27

χ^2 / ndf	1.498 / 1
p0	0.8083 ± 0.04746
p1	185.3 ± 22.94
p2	2.55e-07 ± 1.478
p3	112.7 ± 0
p4	0.1957 ± 0.04974
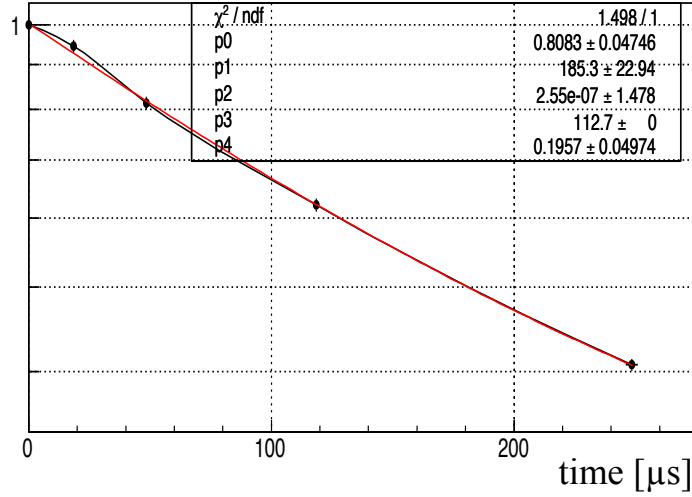
Figure 18: Relative rate of the activities with energy deposit $1 < E[\text{MeV}] < 4$ as a function of the FADC gate delay. The curve was fitted with the Equation 2 (red line), the exponential + constant term.

4.2.3 Environmental gamma

Environmental gamma was measured with the NaI counter at BL13 when the RCS was off. The count rate between 1 and 3 MeV measured with the NaI counter is 10.13 Hz. The activities above 3 MeV was induced by cosmic rays. Using Geant4, the shape of spectrum can be reproduced from the combination of ^{238}U, ^{232}Th series and ^{40}K, assuming $3\%/\sqrt{E[\text{MeV}]}$. The spectra of measured and reproduced environmental gamma are shown in Figure 19. Estimated flux of environmental gamma is 4.3 /s/cm^2. Similarly, environmental gamma was measured with other NaI counter at Tohoku University and estimated flux is 3.9 /s/cm^2. Although amount of environmental gamma depends on surrounding materials such as concrete, soil and so on, the amount of environmental gamma at two different places are not much different. Therefore the amount of environmental gamma at the 3rd floor is expected to be at the same level as above fluxes. This measurement concludes that Gd-loaded scintillator is useful to reduce the background efficiently.

4.3 Estimated background rates at the detector location

The background rate at the detector location (the 3rd floor in MLF) was estimated by using Particle and Heavy Ion Transport code System (PHITS)[21]. The PHITS is used for designing radiation shielding at MLF. The outputs of PHITS and the radiation survey results at many places at MLF were compared and evaluated with each other. The PHITS is suitable to estimate the background rate at MLF. We first evaluated the background rate at BL13 by PHITS and check the validity of PHITS. Figure 20 shows the comparison of the energy spectrum measured with the 1 ton detector, and the estimation based on PHITS. The observed energy spectrum was
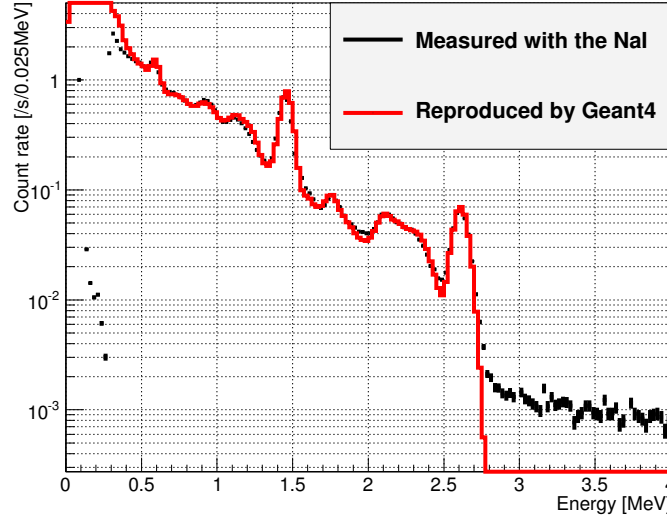
Figure 19: The energy spectrum of environmental gammas at BL13 measured by the NaI counter. The black spectrum is measured data, while the red spectrum is MC result reproduced by Geant4. The effects of the cosmic ray events is observed above 2.6 MeV in data. We can avoid this background with Gd-loaded scintillator.

reproduced.

We then estimated the rates of backgrounds hitting the detector at the 3rd floor by PHITS. By taking the ratio of the estimated rates at BL13 and the 3rd floor by PHITS, and multiplying the ratio to the observed background rate at BL13, the expected background rate at the 3rd floor, n_{exp}, is

$$n_{\mathrm{exp}} = n_{\mathrm{BL13}} \times \frac{N_{\mathrm{candidate}}}{N_{\mathrm{BL13}}} \ , \tag{3}$$

where n_{BL13} is the observed background rate at BL13, N_i is the estimated background rate at the i-th location by PHITS. By calculating the equation, the background rates at the 3rd floor at the surface of the supposed detector described in Section 5 with 1 MW beam power were estimated to be 14 /spill/detector for gammas and 40 /spill/detector for neutrons. By taking the probability of the backgrounds coming to the fiducial volume in the detector, into account, these values are low enough to observe the $\bar{\nu}_e$ signals by IBD as described in Section 6.3.

We also estimated the background rate of the Michel-electrons. Because of the limitation of the Monte-Carlo statistics, we just compared the rates of high energy neutrons which can potentially produce charged pions ($E_{\mathrm{neutron}} >200$ MeV). Figure 21 shows the estimated rate of the high energy neutrons hitting each detector at BL13 and the 3rd floor. The PHITS estimated more than 4 orders of magnitude smaller background rate at the 3rd floor than that at BL13. By considering the beam power difference (300 kW $\rightarrow$ 1 MW), we thus supposed the background rate of the Michel-electron at the 3rd floor was 2×10^{-7} /spill/detector.
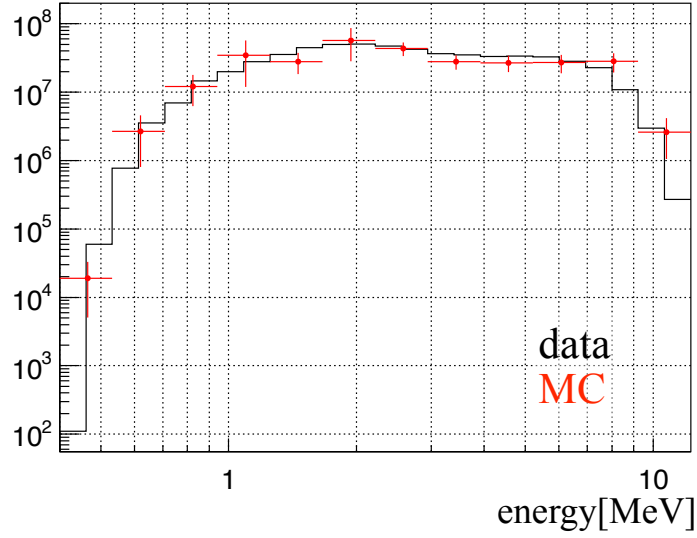
Figure 20: Comparison of the energy spectrum below 12 MeV measured with the 1 ton detector and the estimation based on PHITS. The integrals of the histograms were normalized to each other. The observed energy spectrum was reproduced by PHITS.
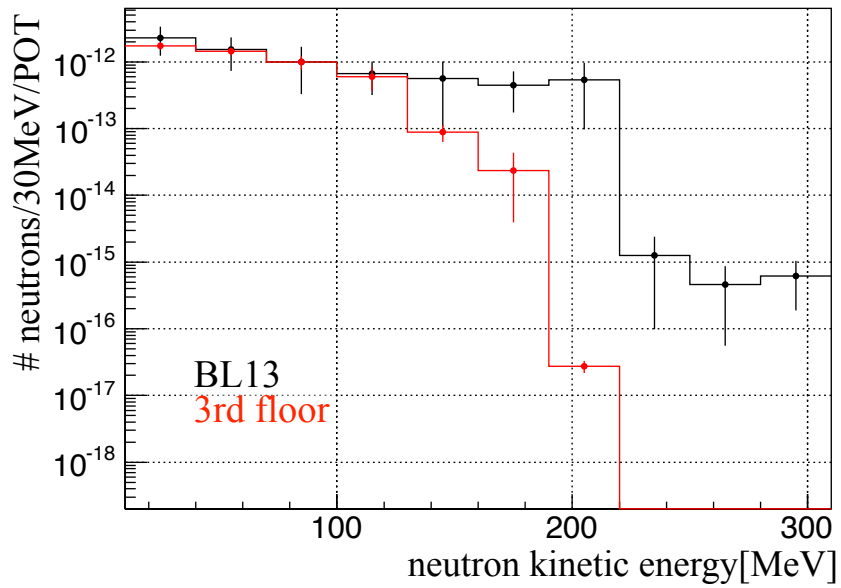
Figure 21: Estimated rate of the neutrons hitting each detector at BL13 (black) and the 3rd floor (red) as a function of neutron kinetic energies. The PHITS estimated more than 4 orders of magnitude smaller background rate at the 3rd floor than that at BL13 with respect to neutrons which can produce charged pions.
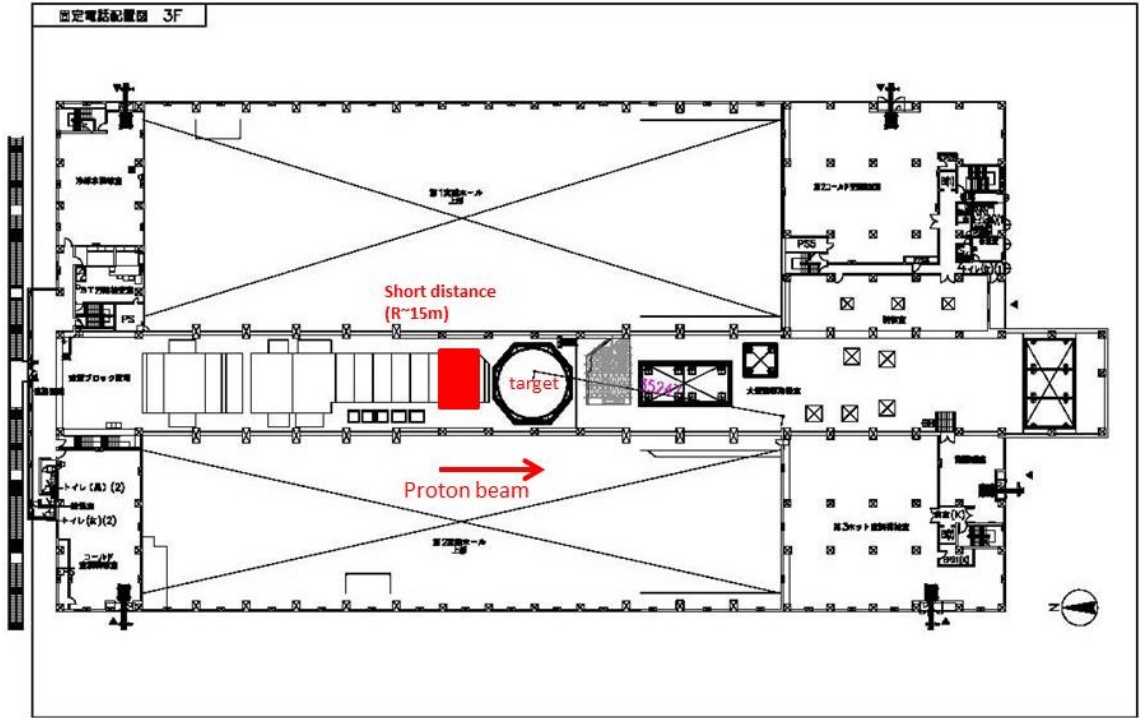
Figure 22:   Drawings of the 3rd floor of the MLF building (top view). Candidate site of the 50 ton detector is shown in the red box.

5   The detector

5.1   The detector site

The detector site is the third floor of the MLF, which is used for the maintenance of the mercury target. Figures 22 and 23 show the top and side view of the detector site. Red box in Figure 22 shows the detector site at the 3rd floor. It is put at 13 m above and 11 m upstream of the target.

For the constraints from the entrance of the MLF building, two detectors are put in the red box area. A design of one detector is shown in the next subsection.

5.2   Detector structure

Figure 24 shows a schematic drawing of one of two proposed neutrino detectors.

The outer tank is a stainless steel cylindrical tank with diameter of 4.4 m, height of 4.4 m and volume of 70 m^3. In the tank, there is an acrylic vessel of diameter of 3.4 m, height of 3.4 m and volume of 31 m^3. The acrylic vessel is filled with 25 tons of a gadolinium loaded liquid scintillator (Gd-LS) described in section 5.3. Signal is defined by the delayed Gd signal. In this way the detection efficiency of the prompt signal is independent of the energy. There is a calibration port on the top of the acrylic vessel which allows access of calibration devices from top of the detector. The
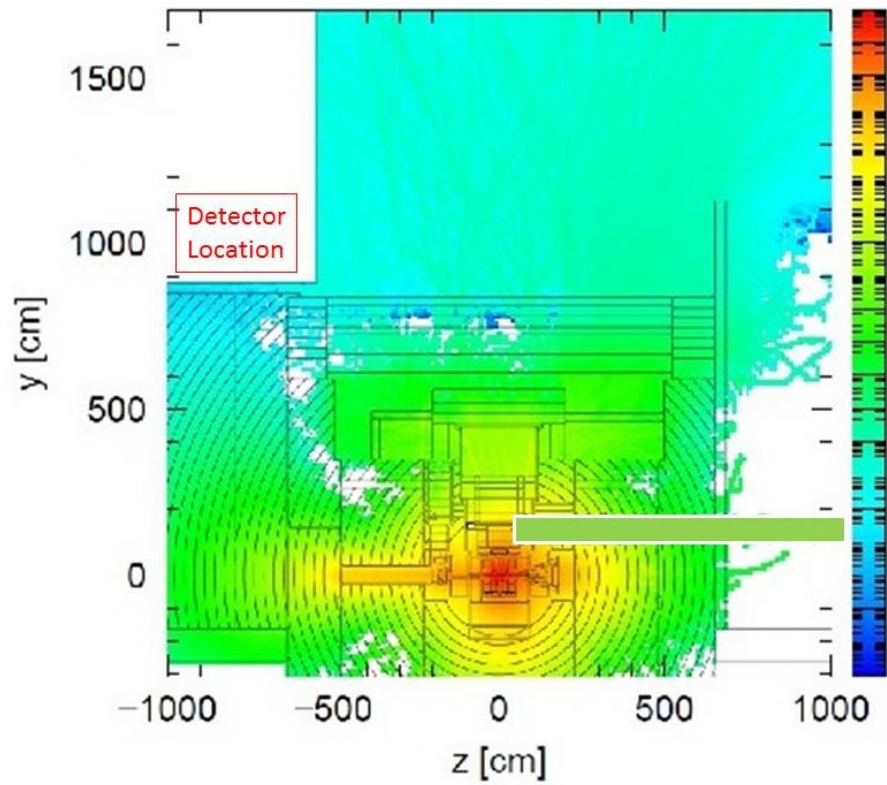
Figure 23: Detector location of the 3rd floor of the MLF building (side view). Color shows the radiation level, and the red part corresponds to the mercury target.
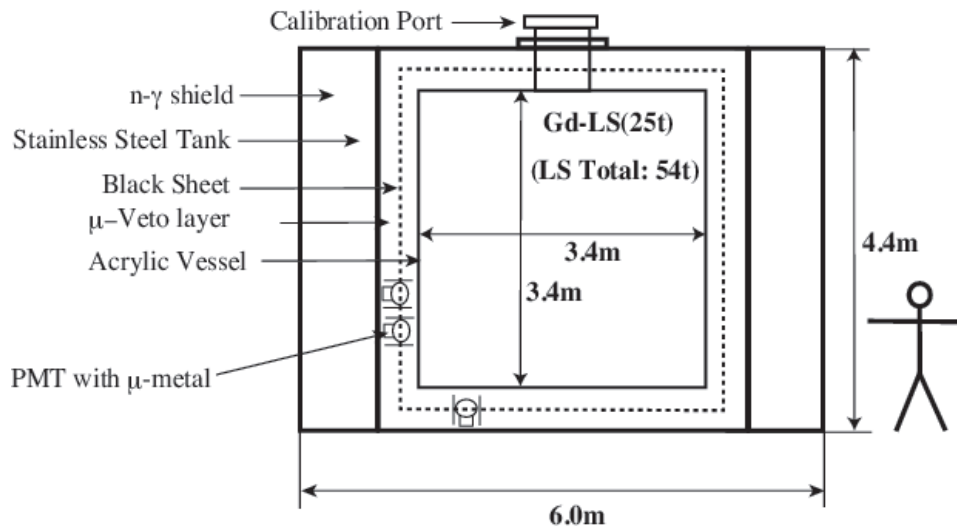
Figure 24: Schematic drawing of the neutrino detector. (Note that the same two detectors are put at the site, which have a total fiducial mass of 50 t consisting of Gd-loaded liquid scintillator.)

region between the stainless steel tank and the acrylic vessel is filled with 36 m^3 of gadolinium *unloaded* liquid scintillator. The scintillation yield of the LS and the specific gravity are matched to those of Gd-LS. This LS catches γ-rays which escape from the Gd-LS region and reproduces original neutron absorption energy. 150 10-inch diameter PMTs (section 5.4) are arranged such a way that their equator of the glass is 25 cm from the stainless steel wall. Black sheets equipped between PMTs optically separate the liquid scintillator layer into two. The LS can move freely through openings of the black sheets and there is no differential pressure between the two LS regions. The outer region is viewed by additional 5-inch PMTs and used as cosmic-ray anti counter.

There are electronics racks near the tank. Most of the data processing is performed near the tank. Only a few network and power cables connect between the detector-electronics system and outer laboratory. The detector-electronics system can be moved by a crane at once after disconnecting such cables.

The weight of the stainless steel tank is 5 tons. The weight of the liquid is 54 tons and electronics is 1 tons. The total weight of the detector is 60 tons and the weight per unit footprint is 4 ton/m^2.

The whole detector structure is surrounded by neutron and γ-ray shields which is made of iron slab and boron loaded paraffin blocks or additional water tank or LS layer. These shields can be dismantled quickly. The detector has to be transferred to a different place at least once per year to make room for inspection of the MLF beam lines. In such cases the radiation shield will be disassembled and the detector and electronics system will be moved by the crane of the lab. In case emergency access to the beamlines is necessary, the detector has to be quickly made ready for the transfer.

5.3 Liquid scintillator [22]

The detection of electron antineutrinos via the inverse beta-decay reaction is one of the main signals. Various organic liquid scintillators (LS) have often been used as the detector medium because they produce relatively large numbers of photons at low energies of a few MeV. The antineutrino signal is a delayed coincidence between the prompt positron and the capture of the neutron in an (n,γ) reaction after it has been thermalized in the LS. This delayed coincidence tag serves as a powerful tool to reduce random backgrounds.

The neutron capture can occur on gadolinium, Gd. The (n,γ) cross-section for natural Gd is high, 49,000 barns. Because of this high cross section, only a small concentration of Gd, (0.1 $\sim$ 0.2 % by weight), is needed in the LS. The neutron-capture reaction by Gd releases a sum of 8-MeV energy in a cascade of 3-4 γ-rays. The higher total energy release of the γ-rays and their enhanced isotropy help to exclude low-energy backgrounds from other sources, such as radioactive decay in the surrounding environment and materials. The time delay for the neutron-capture is $\sim27\mu$s in 0.1 % Gd, and this short delay time helps to reduce the accidental background rate significantly.

A multi-ton scintillation detector for an antineutrino oscillation experiment must satisfy a number of stringent requirements: The Gd-LS must be chemically stable

which means no formation over time of any components in the liquid that will absorb or scatter light, or change the concentration. The Gd-LS must be optically transparent, have high light output, and pose low intrinsic radioactive background. The Gd-LS must also be chemically compatible with the containment vessel. For example, it is known that certain steels could leach metallic impurities into scintillator. Several organic scintillation solvents were studied to test their feasibilities for the above-mentioned criteria. Linear alkylbenzene, LAB, first identified as a scintillation liquid from the SNO+ R & D, is composed of a linear alkyl chain of 10-13 carbons attached to a benzene ring; it is commercially used primarily for the industrial production of biodegradable synthetic detergents. LAB has a light yield comparable to that of PC and a high flash point, which significantly reduces the safety concerns. These notable characteristics make it suitable for a large-scale neutrino experiment. Current ongoing or proposed experiments for reactor electron antineutrinos, Daya Bay and RENO; double-beta decay, SNO+; and solar neutrinos, LENS, unanimously select LAB as their primary scintillation liquid. Similarly, this proposed experiment will use LAB as the singular solvent for the Gd-loaded option; which has advantage of stability, high light-yield, and optical transmission over a binary solvent system (i.e. PC or LAB in dodecane or mineral oil).

It is commonly known in the community that the quality of Gd-LS is the key to the success of the LS experiments. There is heightened concern for a new long-duration oscillation experiment such as we propose here. The BNL neutrino and nuclear chemistry group has been involved in R&D of chemical techniques for synthesizing metal-loaded organic liquid scintillators since 2000 and is currently a member of several liquid scintillator experiments. A highly stable 0.1% Gd-LS with attenuation length of $\sim$ 20m and $\sim$ 10,000 optical photons/MeV has been developed by the BNL group for the reactor antineutrino experiments. Indeed, Daya Bay has published its first observation of non-zero θ_{13} in 2012, based on the successful detection of the IBD reaction by Gd-loaded liquid scintillator.

5.4   PMT [23]

150 low background 10 inch PMTs will be used to detect the scintillator photons produced by IBD reaction. These kinds of PMTs have been used in paraffin oil at Double Chooz and RENO neutrino detectors. For example, the PMT used in Double Chooz and RENO experiment is HPK-R7801MOD-ASSY which has the following properties. The quantum efficiency times collection efficiency is 23%. TTS is 2.9 ns FWHM, dark rate for 1/4 p.e. threshold is 4 kHz (typical) and 8 kHz (Max). The peak to valley ratio is 2.8 and clear one photoelectron peak can be detected. 10^7 gain is obtained with 1500 V of high voltage and the power consumption is 0.2 W with this voltage. The PMT is operated with positive HV. The base part of the PMT is molded by transparent epoxy to prevent the electric circuit material from directly touching the oil. A Teflon jacket cable (RG303/U) is used to readout signal and supply HV. There is a splitter circuit between HV and PMT to separate HV and signals. There is a 50 Ω resister at the end of the signal cable to quickly dump the tail of large signals. The PMT will be equipped with μ-metal shield to reduce the effect of the
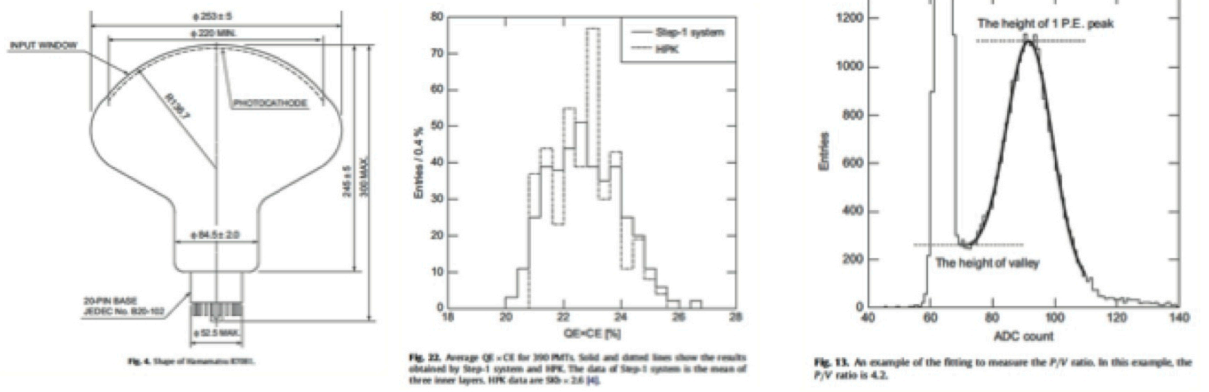
Figure 25: HPK PMT properties. Left: Dimension. Center: Quantum efficiency × collection efficiency. Right: Peak to Valley ratio for one photoelectron signal.

earth magnetic field. The PMT base is thermally contacted to the stainless steel tank wall to dissipate the generated heat efficiently.

The energy of neutron signal is 8 MeV and we require the energy resolution of

$$\frac{\delta E}{E} < \frac{15\%}{\sqrt{E(\mathrm{MeV})}}. \tag{4}$$

4% of photo coverage is necessary to obtain this energy resolution assuming there is 50% of scintillation light inefficiency from various reasons, which corresponds to 150 PMTs. The glass is a low background type. Low background sands are chosen for the glass material and they are melted in a platinum coated furnace to avoid contamination of radioactivities from the crust of the furnace wall.

The radioactive elements in the glass are U:13 ppb, Th:61 ppb and ^{40}K:3.3 ppb and expected γ-ray rate ($E > 1$ MeV) from the PMT glass is ~ 400 Hz. In addition to the PMTs for neutrino target, 50 additional 5 inch PMTs will be used for muon anti counter.

5.5 Liquid Operations

5.5.1 LS Filling Operation

The liquid scintillators will be delivered by using teflon coated iso-containers and lorry tracks from manufacturer. There will be temporary liquid handling hut with storage tanks and pumps at the unloading area of the MLF area. The delivered liquids are once stored in the storage tanks and then sent to the detector and carefully put in the detector by equalizing the liquid levels between inside and outside of the acrylic vessel. After the filling is complete, the oil filling pipes are disconnected from the detector to isolate it for the transfer.

5.5.2   Detector Operation during data taking

It is not necessary to circulate the liquid during data taking operation. So once the detector is filled by the liquids, it will be sealed. On the other hand, the gas phase is filled by nitrogen from tanks. A small amount of nitrogen gas will be continuously supplied to the detector, which equalizes the differential pressure passively keeping up the changes of the atmospheric pressure.

5.6   Electronics

The requirements for the electronics are listed below:

1. The prompt signal must be recorded without dead time for 10 μs from the beam injection.

2. The delayed signal must be recorded with a time stamp for ~ 40 ms from the beam injection.

3. The sampling rate must be high enough to achieve the timing resolution of 1 ns.

4. The dynamic range must cover from 1 MeV to 50 MeV with a resolution of 12 bits or more.

In order to fulfill these requirements within a reasonable cost, we will modify a 500-MHz flash ADC and a Micro TCA readout system, which is designed at RCNP for the CANDLES experiment upgrade. The system is based on the existing a 500-MHz flash ADC (Figure 26) and an ATCA readout system [24] for the present CANDLES experiment [25]. A Micro TCA system [26] is described as the following. An AMC module has two 8-bit flash ADC with the 500 MHz sampling rate. 12 AMC modules are installed on a micro TCA sub-rack. Thus, one sub-rack accepts 24 analog signals. Each signal from the detector will be divided into low and high gain analog signals with a splitter at the input of the flash ADC. One AMC module handles one pair of signals. A total of 400 AMC modules will be used for the experiment. They are held on 34 sub-racks. Or using ATCA carrier, which holds 8 AMC modules, 5 ATCA sub-racks holds up to 480 AMC modules as shown in Figure 27. The dead-time-less signal processing for the trigger and the data readout is realized by pipeline data processing using a FPGA that implements delays, a trigger control, a clock, event buffers with a data processor and a read-out control (Figure 28). The concept of the pipeline processing is already applied to the CANDLES experiment. Performance of a prototype of the new flash ADC will be checked at RCNP in December 2013.

Serial data link is used for the data collection from each FPGA chip. On board connections, backplane connections and inter-sub-rack connections use the same data link. The data link is extended by router chip of the data link. Therefore the system is highly scalable from small system to large system. Maximum data rate from each AMC module is 16 MB/s at the maximum. Collected data are read through several

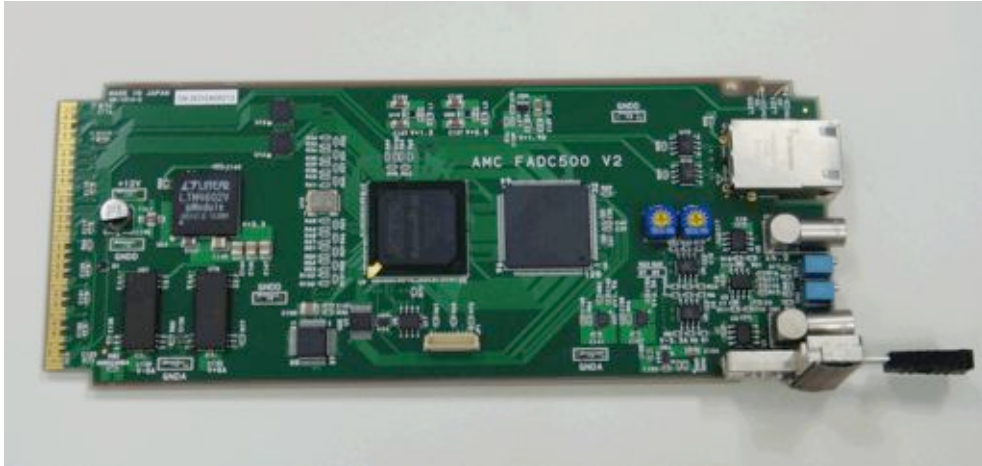Figure 26: 500-MHz flash ADC module used for the present CANDLES experiment.

schematic view of MicroTCA crate   schematic view of ATCA carrier module
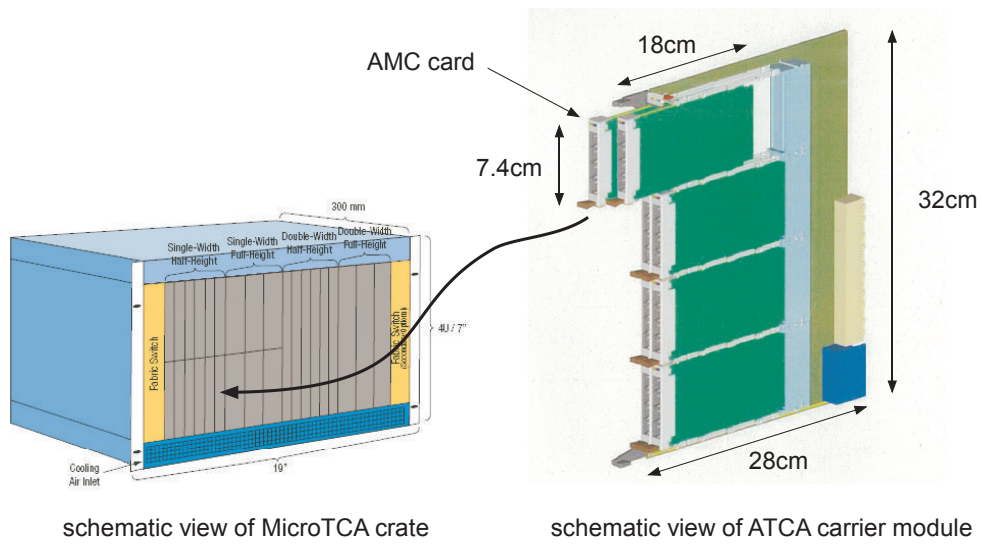
Figure 27: Schematic view of Micro TCA crate (left) and ATCA carrier module (right).

37
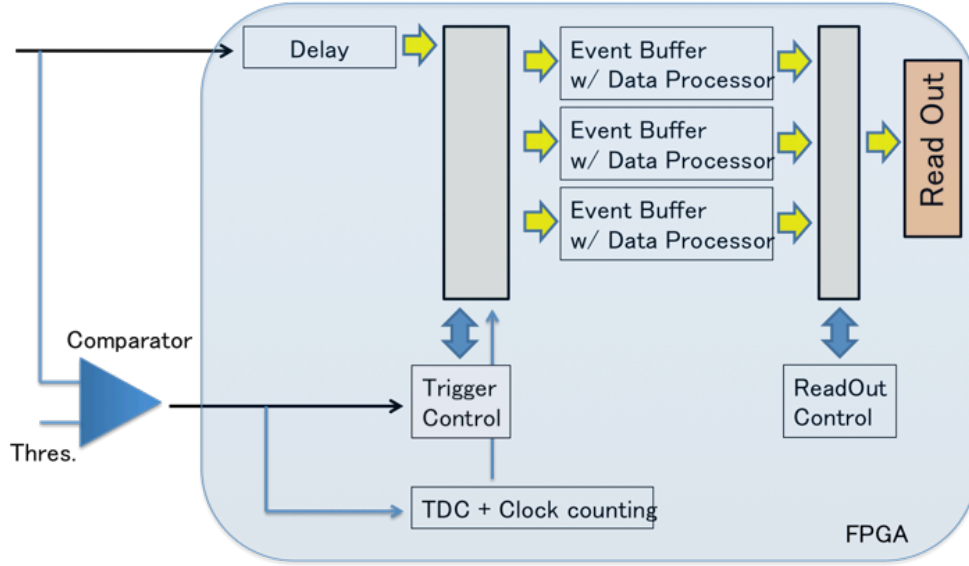
Figure 28: Concept of the electronics.

Gigabit Ethernet links by several PC. The number of PC and Ethernet link depends on the demands of the data rate.

5.7 Expected performance

5.7.1 Vertex reconstruction and the position resolution

Vertex of an event is reconstructed by using hit times from the buffer PMTs. The hit time for each PMT is defined as time difference by when the pulse height exceeds 1 mV of the threshold from the trigger time. The hit time depends on time constant of light emissions in the liquid scintillator, time of flight of the light between the vertex and surface of each PMT, time shift due to time difference until when a signal is produced from when the event occurs, and number of photoelectrons hitting each PMT. So as free parameters in fit function for the vertex reconstruction, the vertex position (x,y,z) and the base shift (T0) are used. Here, corrected hit time of i_{th} PMT ($CorT_i$) is defined as follows.

$$ CorT_i = HitT_i - T0 - \frac{|\vec{P}_{VTX} - \vec{P}_i|}{C_n}, \tag{5} $$

where, $\vec{P}_{VTX}$ and $\vec{P}_i$ are the vertex and i_{th} PMT positions, respectively, C_n is light velocity in the liquid scintillator. Upper figure in Figure 29 shows probability density distribution(f_{pdf}) of the corrected hit times depending on the number of photoelectrons(N_i^{PE}), estimated by using MC samples of thermal neutron capture on Gd at various positions in the buffer tank. Lower figure shows the examples depending on number of

photoelectrons. When the number of photoelectrons hitting a PMT is a few, the corrected hit times distribute following the time constant of light emission in the scintillator. When the number of photoelectrons increases, the time constant of the light emission does not affect the distribution of the corrected hit times. Then the distribution is close to Gaussian depending on TTS of the PMT. For the vertex reconstruction, maximum likelihood method with the probability density distribution. The likelihood($\mathcal{L}$) is defined as follows.

$$\mathcal{L} = \prod_i f_{pdf}(CorT_i, N_i^{PE}), \quad (6)$$

then, position with minimum value of $-ln\mathcal{L}$ is the reconstructed vertex.
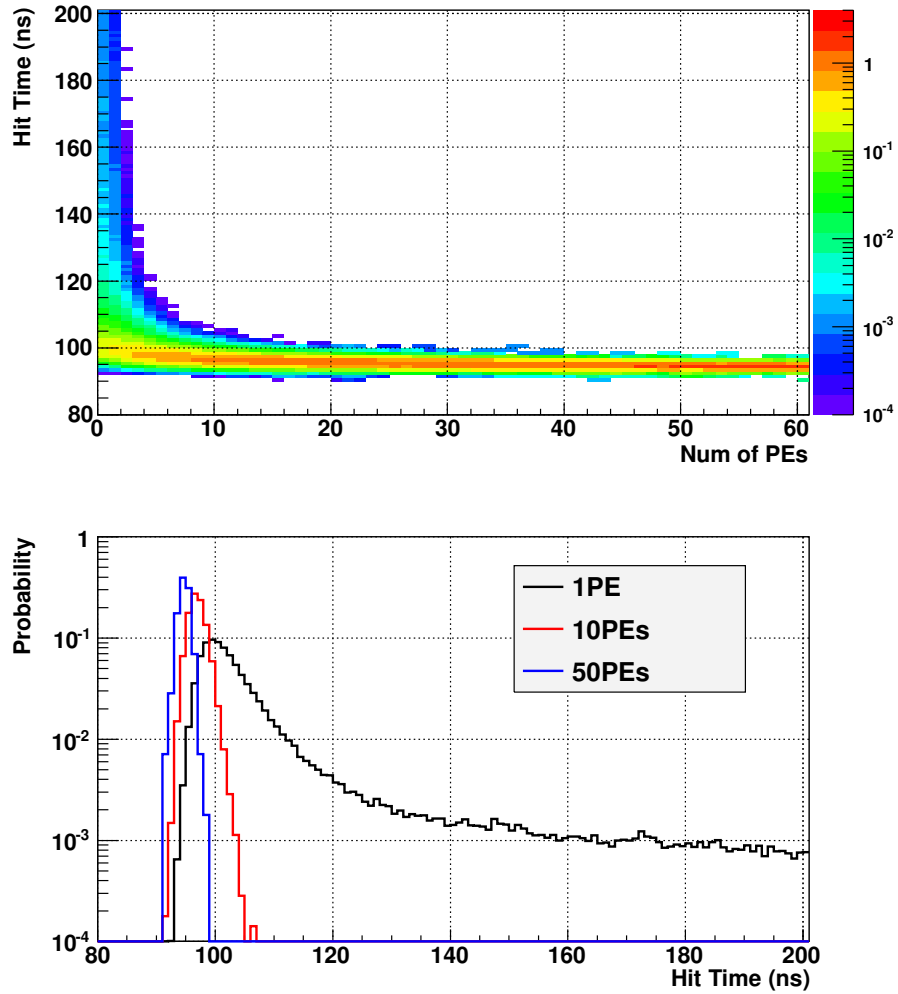
Figure 29: Hit timing delay as a function of the number of photo-electron received by PMTs. It is used for the probability density distribution for maximum likelihood method for the vertex reconstruction. Upper figure shows the probability density distribution. Lower figure shows the typical number of photo-electron dependence of the hit time. Black, red and blue lines show 1 photoelectron, 10 photoelectrons and 50 photoelectrons cases, respectively.

Figure 30 shows evaluations of the reconstructed position biases and resolutions in cases of thermal neutron capture on Gd (total 8 MeV gammas) and 60 MeV electron considering the e$^+$ energy of the IBD events for the $\overline{\nu}_e$ signals at various positions on R direction and Z axis in the cylindrical detector. The reconstructed position bias is estimated as mean value of a peak of distance distribution between true vertex position and the reconstructed one, and the reconstructed position resolution is estimated as the RMS. The reconstructed bias and position resolution in energy range of the IBD events for the $\overline{\nu}_e$ signals and whole target volume, are less than ±15 cm and 25cm, respectively.

Figure 30: Reconstructed vertex bias(upper plot) and resolution(lower plot) on R direction (left) and Z direction (right). Blue and red lines show cases of neutron capture events on Gd (The true energy is 8 MeV) and positron events with 60MeV of the kinetic energy (The true energy is 61.022MeV due to annihilation gammas with electron), respectively. Gray and black lines show target and buffer walls, respectively.

5.7.2 Energy reconstruction and the resolution

Number of photoelectrons of i$_{th}$ PMT (N_i^{PE}) is calculated as follows considering attenuation length of the scintillation light ($L_{Att} \sim 10$m) and solid angle to the PMT from the vertex position.

$$N_i^{PE} = N_{tot} \times \frac{S_{10inch}^{PMT}cos\theta_i}{4\pi L_i^2} \times exp(-\frac{L_i}{L_{Att}}), \qquad (7)$$

where N_{tot} is total number of scintillation photons emitted at the vertex, S_{10inch}^{PMT} is surface area of photocathode of 10 inch PMTs, θ_i is angle between the surface and incident direction of the light to the PMT, and L_i is base line between the vertex and the PMT. Energy of the event (E) has a relation of $N_{tot} \propto E$, and the energy is

reconstructed as follows.

$$E = \frac{N_{tot}}{\alpha} = \frac{\sum N_i^{PE}/\alpha}{\sum \left(\frac{S_{10inch}^{PMT} cos\theta_i}{4\pi L_i^2} \times exp(-\frac{L_i}{L_{Att}}) \right)}, \quad (8)$$

where, α is number of scintillation photons emitted at the vertex per 1MeV, and Q_{tot} is sum of numbers of photoelectrons of all PMTs. Then, the α is calculated by fitting with Gaussians to peaks in the N_{tot} distribution of thermal neutron capture events on Gd at detector center.

Figure 31 shows evaluations of the reconstructed energy biases and resolutions in cases of thermal neutron capture on Gd (total 8 MeV gammas) and e^+ with 60 MeV of the kinetic energy considering the e^+ energy of the IBD events for the $\bar{\nu}_e$ signals at various positions on R direction and Z axis in the cylindrical detector. The reconstructed energy bias is estimated as a ratio of true energy and mean value calculated by fitting with Gaussian to a peak of the reconstructed energy spectrum, and the reconstructed energy resolution is estimated as the sigma. The reconstructed bias in energy range of the IBD events for the $\bar{\nu}_e$ signals and whole target volume, are less than 5% except for near the target wall.
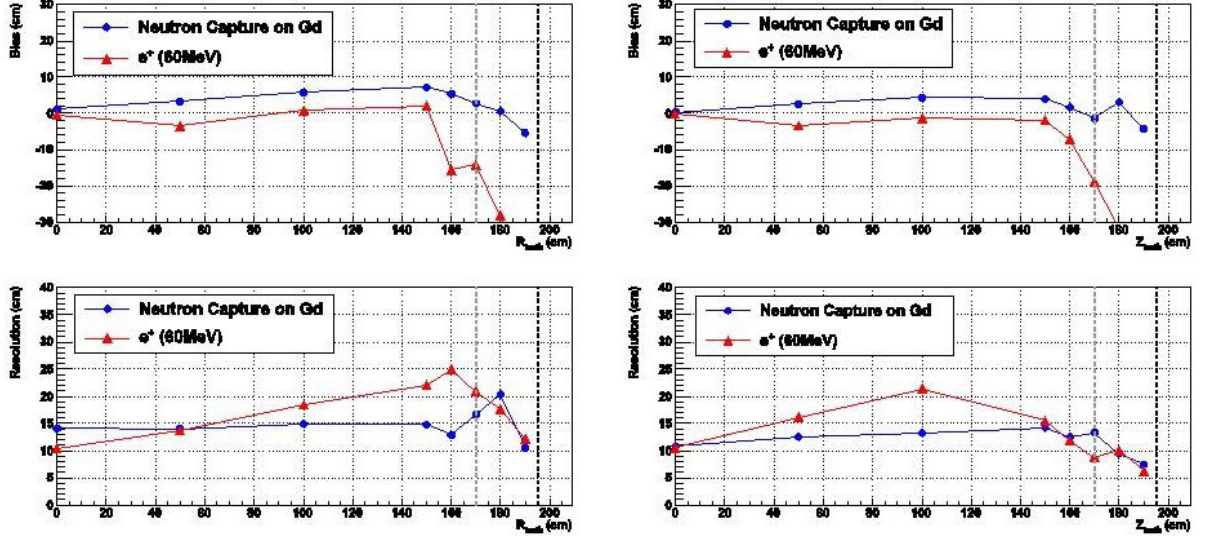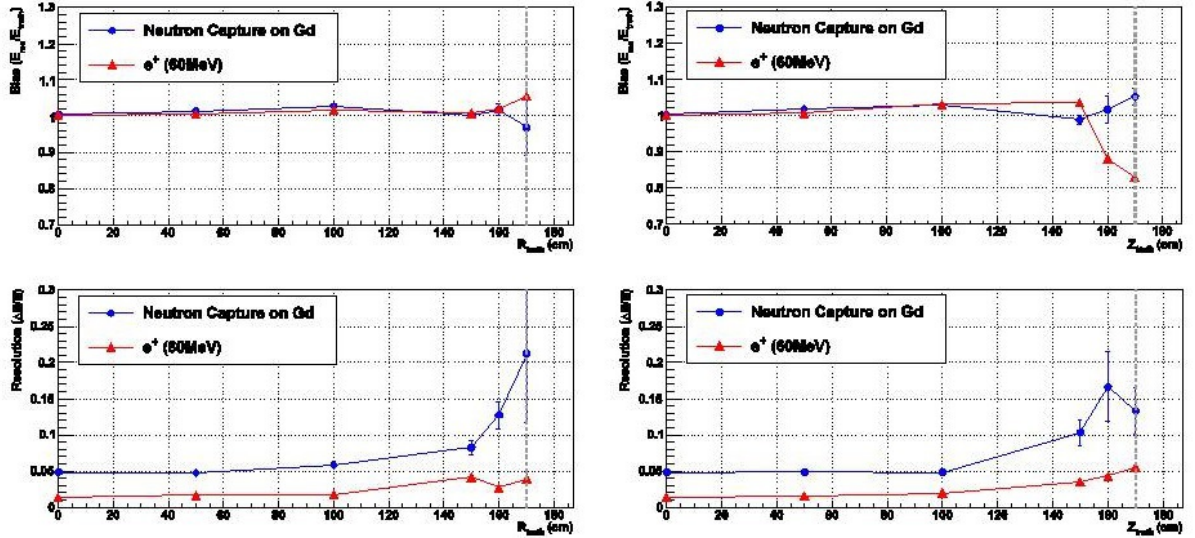

Figure 31: Reconstructed energy bias(upper plot) and resolution(lower plot) on R direction (left) and Z direction (right). Blue and red lines show cases of neutron capture events on Gd (The true energy is 8 MeV) and positron events with 60MeV of the kinetic energy (The true energy is 61.022MeV due to annihilation gammas with electron), respectively. Gray and black lines show target and buffer walls, respectively.

5.8 Neutron Selfshielding

The detectors have selfshield regions with the 50-cm thick LS. We estimated selfshield effect on neutrons with various energies using Geant4. Figure 32 shows ratio of

neutrons which penetrate into the detector to incoming neutrons at the detector surface. Neutrons below 100 keV of kinetic energy are reduced 5 orders of magnitude before they reach the surface of the acrylic tank. On the other hand, the selfshield effect on neutrons above 1 MeV of kinetic energy is smaller than that of below 100 keV because the cross section on hydrogen of neutron elastic scattering decreases as kinetic energy of neutron increases.
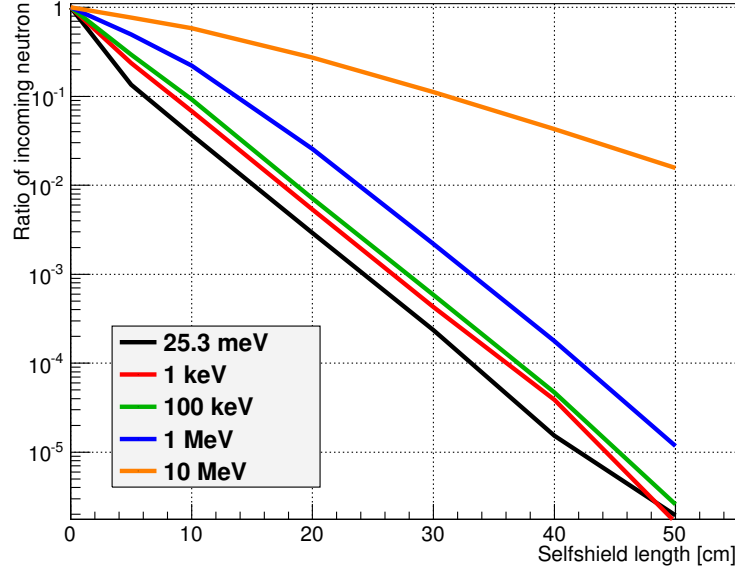
Figure 32: Selfshield effect of the liquid scintillator as a function of the thickness on neutrons estimated with Geant4.

5.9 Particle Identification

As shown in Figure 33, the LSND experiment was able to reject low-energy (< 100 MeV) neutrons relative to electrons by a factor of more than 100. This rejection factor was obtained by combining the fit to the Cherenkov cone with the fraction of hit phototubes that were late (> 10 ns) relative to the fitted event time. The most powerful particle identification parameter was the fraction of hit phototubes that were late, due to the fact that low-energy electrons produce both prompt Cherenkov light and delayed scintillation light, while low-energy neutrons only produce scintillation light with time constants of $\sim$ 2 ns and $\sim$ 20 ns. The LSND mineral oil was doped with a low concentration (0.031 g/l) of b-PBD, so that electrons produced approximately 10 photoelectrons per MeV of Cherenkov light and 20 photoelectrons per MeV of scintillation light at the LSND case, while neutrons produced only scintillation light.

Particle Identification
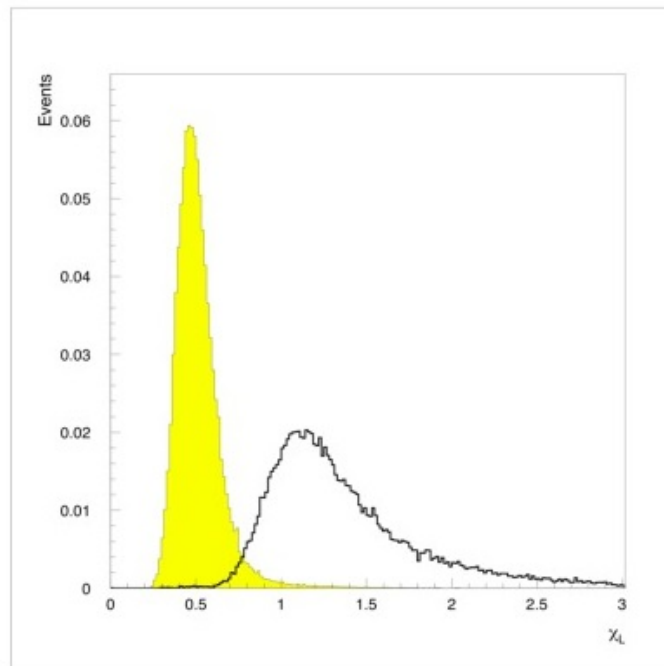
Figure 33: The separation of low-energy electrons from low-energy neutrons in the LSND experiment. The low-energy electrons come from stopped muon decay (shaded yellow), while the low-energy neutrons are cosmic-ray induced (blank).

Improved neutron rejection factors are possible in the future with better electronics and with longer time constant scintillation fluors. The LSND electronics only recorded the time of the first photoelectron on a given phototube. However, better electronics could record the time of all photoelectrons, which would increase the photoelectron statistics and improve the separation between electrons and neutrons. In addition, the use of longer time constant scintillation fluors would further improve the identification of Cherenkov light and scintillation light and the rejection of neutrons.

In the MLF experiment, the expected numbers of photoelectrons (pe) from Cherenkov and scintillation light for a 30 MeV electron are approximately 100 pe and 1000 pe, respectively. The prompt Cherenkov light can be distinguished from the delayed scintillation light with timing, as the time constant for scintillation light is > 2 ns. Cherenkov light is very important both for particle identification (30 MeV neutrons, for example, produce no Cherenkov light) and for angular reconstruction, which can be used to identify neutrino-electron elastic scattering events.

6 Event selection

6.1 Summary of this section

In this section, cuts for the IBD event selection and remaining backgrounds after the selection and efficiency of the cuts are described. Table 6 summarizes the selected number of events for each event category with 50 tons fiducial mass and 1MW times 4-year exposure (assuming 4000 hours operation per year).

The accidental background is expected to be well suppressed with good shielding at the detector site and after the various cuts. Therefore, the dominant background is $\bar{\nu}_e$ from μ^-.

	Contents	/4years/50tons	Comment
Signal	$\overline{\nu}_\mu \to \overline{\nu}_e$	811	$\Delta m^2 = 3.0 eV^2$, $sin^2 2\theta = 3.0 \times 10^{-3}$ (Best Δm^2 for MLF exp.)
		337	$\Delta m^2 = 1.2 eV^2$, $sin^2 2\theta = 3.0 \times 10^{-3}$ (Best fit values of LSND)
Backgrounds	$\overline{\nu}_e$ from μ^-	377	FLUKA (Table 3)
	$^{12}C(\nu_e, e^-)^{12}N_{g.s.}$	38	see 6.3.4
	beam associated fast neutron	0.3	see 6.3.2
	Cosmic ray induced fast neutron	42	see 6.3.5
	Total accidental events	37	see 6.3.6

Table 6: Numbers of events of the signal and backgrounds with total fiducial mass of 50 tons after applying IBD selection criteria shown in Table 7 for 4 years measurement.

6.2 Selection criteria

Before applying IBD event selection, events in time window from 1 μs to 10 μs after the beam trigger are selected as the prompt signal in order to reject the on bunch events (Δt_{prompt} cut). Variables for the IBD event selection are energies of prompt (E_{prompt}) and delayed ($E_{delayed}$) signals, $\Delta t_{delayed}$, which is time difference between the prompt and delayed signals, and ΔVTX, which is distance between reconstructed positions for the prompt and delayed signals. Cut condition and the efficiency of $\overline{\nu}_e$ signals for each variable are shown in Table 7. This efficiency is for oscillated signals for high Δm^2 region (e.g.; $\Delta m^2 > 100$ eV^2). Cut condition of the prompt energy is decided considering with the spectra of oscillated $\overline{\nu}_e$ signals and other neutrino backgrounds. Cut conditions of the delayed energy and $\Delta t_{delayed}$ are decided considering the total 8 MeV gammas via thermal neutron capture on Gd in the target volume and the 30 μs of capture time. The ΔVTX cut is powerful for reducing the accidental background, because ΔVTX of correlated events like $\overline{\nu}_e$ signals are usually distributed within 1 m, while the ΔVTX of accidental events are distributed over several meters depending on the target and buffer volumes. Total cut efficiency of $\overline{\nu}_e$ from $\overline{\nu}_\mu$ is 48%. Number of $\overline{\nu}_e$s (50 tons of total fiducial mass, 4 years measurement) in case of Δm^2=3.0eV^2 and sin$^2 2\theta$=3.0×10^{-3} after applying the selection criteria, is 811 events.

Cut Condition	Cut Efficiency
1.0≤ Δt_{prompt} ≤10μs	74%
6≤$E_{delayed}$ ≤12MeV	78%
20≤E_{prompt} ≤60MeV	92%
$\Delta t_{delayed}$ ≤100μs	93%
ΔVTX≤60cm	96%
Total	48%

Table 7: IBD Selection criteria and efficiencies for the oscillated signals for high Δm^2 case.

Energy spectrum of delayed IBD signal is shown in Figure 34. Even using Gd-LS, there is some amount of H capture inside the detector, which creates capture gammas with 2.2 MeV. It reduces the detection efficiency.

6.3 Backgrounds

6.3.1 Backgrounds for IBD events

After the IBD selections, there are remaining backgrounds in the IBD candidates. The backgrounds are classified into accidental and correlated backgrounds for the IBD events. The accidental background is induced by two independent events entering in the detector in $\Delta t_{delayed}$ for the IBD coincidence accidentally (see 6.3.6). The
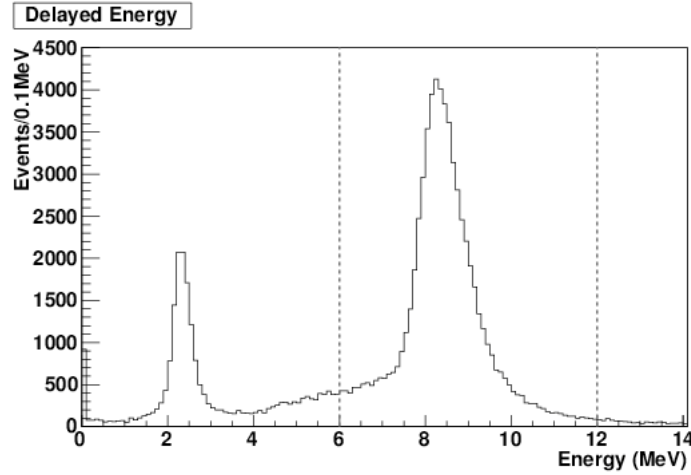
Figure 34: Energy spectrum of delayed IBD signal is shown. Even using Gd-LS, there is some amount of H capture inside the detector, which create capture gammas with 2.2 MeV. It reduces the detection efficiency.

correlated background is induced by sequential signals caused by one event. Main sources of correlated backgrounds are beam associated fast neutrons accompanied by Michel electrons and thermal neutron capture on Gd (see 6.3.2), $\overline{\nu}_e$ from μ^- (see 6.3.3), $^{12}C(\nu_e, e^-)^{12}N_{g.s.}$ reaction(see 6.3.4), and cosmic muon induced fast neutron from outside of the detector(see 6.3.5).

In order to achieve the current design sensitivity for sterile neutrino search, we need to reduce the total number of background events for the IBD candidates, except for the $\overline{\nu}_e$s from μ^-, to several events/year per one detector, compared with several tens events/year/detector of $\overline{\nu}_e$s from μ^-. The detail of each background is described in each subsection.

6.3.2 Beam associated fast neutron

Fast neutrons are induced by beam protons interacting in the target, and these beam neutrons contribute to the background and are classified into the 3 types below:

1. Neutrons below several tens MeV.

2. High energy neutrons with several hundreds MeV entering in the detector.

3. Gamma rays generated via thermal neutron capture with several μs of capture time outside of the detector.

Neutrons below several tens MeV The neutron flux entering the detector at the candidate site is 41/spill per one detector (see section 4). The remaining beam neutron rate after applying the IBD selections for delayed signals (delayed energy between 6 and 12MeV, and $\Delta t_{delayed} <100\mu$s) is 1.9/spill. In order to reduce more neutrons, number of hit PMTs cut (NHIT cut) is very effective in addition to the IBD selections. Because most remaining events after applying the IBD selections are ones

captured on H in the gamma catcher region near PMT surfaces, the visible energy becomes larger when comparing with the true energy, but the number of hits is not large when comparing with events captured on Gd. Actually, the neutrino signals after applying the IBD selections are not reduced by the NHIT cut (the cut efficiency is above 99 %). The neutron rate reduced by $\sim 10^{-3}$ by applying the NHIT cut. Finally, the remaining neutron rate after applying both NHIT and IBD selections for delayed signals is expected to be 2.4×10^{-3}/spill per one detector.

High energy neutrons with several hundred MeV entering in the detector
The Michel electron rate in the prompt energy range entering in the detector i at the candidate site is estimated to be 2×10^{-7}/spill per one detector for 1MW. The number of Michel electrons per year is then 72 per one detector. For reducing the number of Michel electrons more, the ΔVTX cut between prompt-like signal due to Michel electron and on-bunch signal due to protons recoiled by the neutrons and rejection of the multi-neutron captures are expected to be effective. Figure 35 shows the ΔVTX distributions between Michel electrons and on-bunch signals, and between the neutrino prompt signals and accidental on-bunch signals, calculated by the MC simulation. There is good separation between both distributions. Thus, the rejection power is expected to be 100. Figure 36 shows the relation between energy of the initial neutron and the multiplicity of neutrons induced by the hadronic interactions (left figure), and the rejection power applying the multiplicity=1 selection (right figure). The mean rejection power is 20. So by applying both cuts, the number of Michel electrons contributing as the correlated backgrounds for the IBD candidates is reduced by 1/2000. It is expected to be 0.3 events considering total fiducial mass of 50 tons for 4 years measurement.
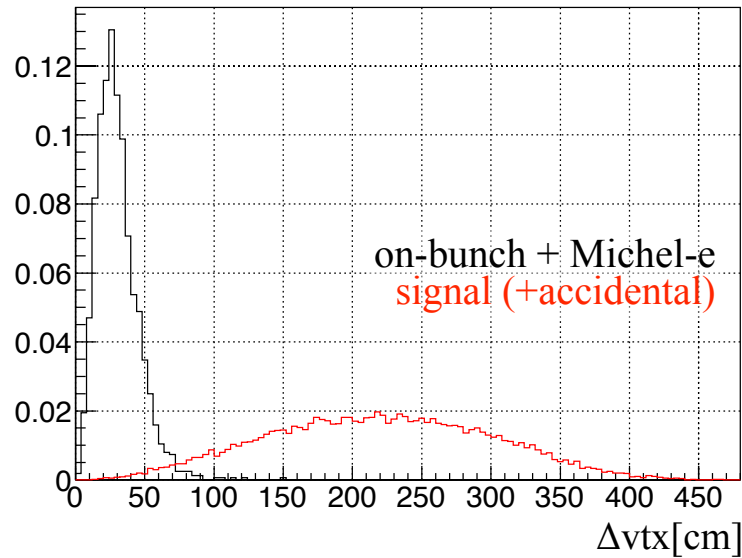

Figure 35: The ΔVTX distributions between Michel electrons and on-bunch signals (black line), and between the neutrino prompt signals and accidental on-bunch signals (red line), calculated by the MC simulation.
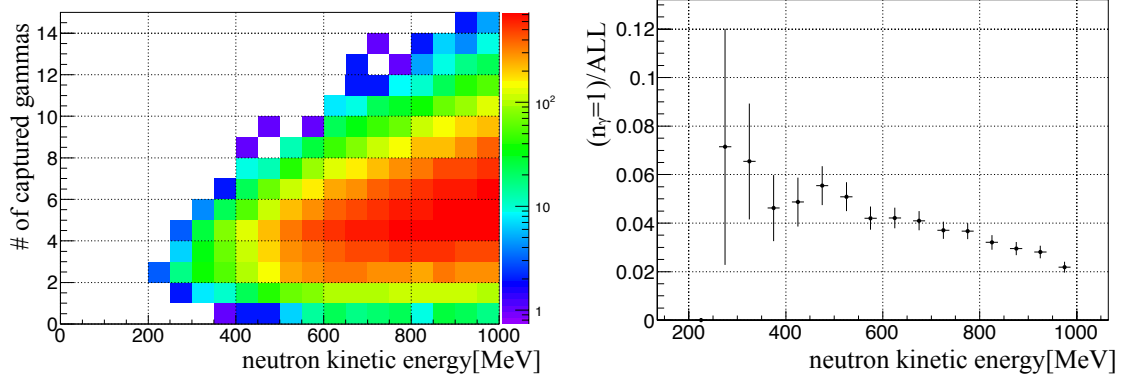
47

Figure 36: The relation between energy of the initial neutron and the multiplicity of neutrons induced by the hadronic interactions (left figure), and the rejection power applying the multiplicity=1 selection.

Gamma rays generated via thermal neutron capture The gamma flux entering the detector at the candidate site is 14/spill per one detector (see section 4). Many remaining events after applying the IBD selections for delayed signals deposit energy in the gamma catcher region near the PMT surfaces, so the NHIT cut, in addition to the IBD selections, is also effective for more gamma reduction. Finally, the remaining gamma rate after applying both NHIT cut and IBD selections for delayed signals is reduced by 4.7×10^{-2}/spill per one detector from 0.8/spill in case of only applying the IBD cuts.

6.3.3 $\overline{\nu}_e$ from μ^-

$\overline{\nu}_e$ from μ^- decay is detected with same sequence of the IBD reaction as $\overline{\nu}_e$ from $\overline{\nu}_\mu$. The total cut efficiency is 47%. Assuming the rate is suppressed by 10^{-3} comparing with the μ^+ decay case, it is expected to be 804 events per 50 tons of total fiducial mass for 4 years measurement. The remaining rate after applying the IBD selection criteria is then 377 events.

6.3.4 $^{12}C(\nu_e, e^-)^{12}N_{g.s.}$

$^{12}C(\nu_e, e^-)^{12}N_{g.s.}$ reaction accompanies subsequent β decay of $^{12}N_{g.s.}$ with 15.9 ms life time as follows:

$$^{12}C + \nu_e \rightarrow e^+ + ^{12}N_{g.s.} ; ^{12}N_{g.s.} \rightarrow ^{12}C + e^- + \nu_e \qquad (9)$$

Then, e^- events contribute to the prompt-like signal and e^+ events decaying within time window for the IBD selection contribute to the delayed-like signal. The total cut efficiency is 0.17%. The rate after applying the selection criteria is expected to be 38 events for 4 years measurement.

48

The e^- and e^+ events contribute to prompt and delayed like signals for the accidental background, respectively. A rate for both prompt and delayed like signals is 8.0×10^{-6}/spill per one detector. Meanwhile, there is also the $^{12}C(\nu_e, e^-)^{12}N^*$ mode, which is a similar reaction. The rate contributing to prompt-like signals for the accidental background was estimated to be approximately 3.8×10^{-6}/spill.

6.3.5 Cosmic muon induced events

There are some important backgrounds induced by cosmic rays; fast neutrons and spallation products. Fast neutrons recoil protons inside the detector, and then are thermalized and create captured gammas. Thus, one neutron can produce both a faked "IBD prompt" and "IBD delayed" signal at the same time. As shown in section C.1 in detail, the estimated number of events with 50 tons fiducial mass times 4 years is 42 events assuming factor 100 rejection using PID ability such as in the LSND experiment.

On the other hand, the spallation products are expected to be negligible, as shown in section C.2.

6.3.6 Accidental backgrounds after applying IBD selection criteria

There is a possibility that background events in energy cut range and time window for the prompt signals contribute to the prompt like signals of accidental backgrounds. Meanwhile, there is a possibility that background events in the energy cut range and time window for the delayed signals contribute to the delayed like signals of accidental backgrounds. In this proposal, the accidental rates (R_{acc}) per one detector were calculated by multiplication of number of spills per year (3.6×10^8 spills/year), single rates per spill for the prompt and delayed like signals (R_{prompt}, $R_{delayed}$) considering the time windows and the cut efficiencies, and the ΔVTX cut efficiency (ϵ_{VTX}) as follows:

$$R_{prompt} = \sum (R_i^{prompt} \times \epsilon_i^{prompt}) \tag{10}$$

$$R_{delayed} = \sum (R_i^{delayed} \times \epsilon_i^{delayed}) \tag{11}$$

$$R_{acc} = R_{prompt} \times R_{delayed} \times \epsilon_{VTX} \times 3.6 \times 10^8 spills/year \tag{12}$$

where i is the type of event contributing to the accidental backgrounds, R_{prompt} ($R_{delayed}$) is calculated as sum rate of all types of the prompt(delayed) like signal considering each cut efficiency(ϵ_i^{prompt}, $\epsilon_i^{delayed}$). Actually, the ΔVTX cut efficiency depends on each combination of prompt and delayed like signals, but the ΔVTX cut efficiency for combinations of the $\overline{\nu}_e$ prompt signals and delayed like signals of the neutron captured on Gd distributing uniformly in the target volume, was used approximately for all components in this proposal. Figure 37 shows distributions of the ΔVTX cut. The cut efficiency below 60cm is 2.3±0.1%. Table 8 shows summary of values for calculation of the accidental background rate. Finally, total number of accidental events is 36.8 events considering 50 tons of total fiducial mass for 4 years measurement.
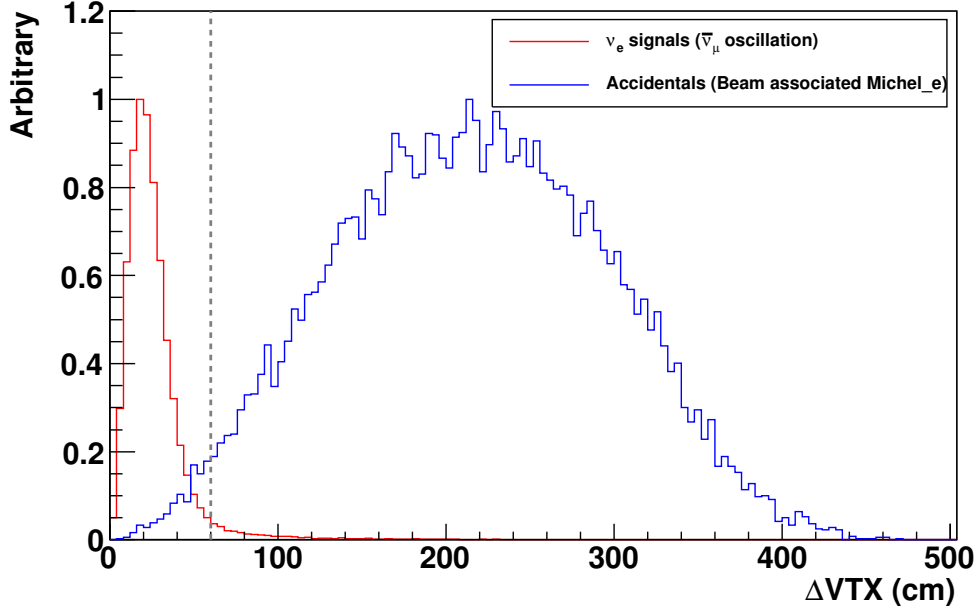
Figure 37: ΔVTX distributions of $\overline{\nu}_\mu \rightarrow \overline{\nu}_e$ oscillation events (red line) and the accidental eventsc(blue line). Gray line shows ΔVTX cut condition.

6.4 Selection summary

Table 6 summarizes numbers of signal and background events with 50 tons of total fiducial mass from two detectors after applying IBD selection criteria for 4 years. Finally, $\overline{\nu}_e$ from μ^- events are expected to be the dominant background for the IBD candidates. The number of $^{12}C(\nu_e, e^-)^{12}N_{g.s.}$ events is expected to be around 10% of the neutrino signal, and it is expected that other backgrounds can also be reduced to around the 10 % level for each in this proposal. Assuming a 4 year measurement with 2 detectors, the number of signal events in the case of $\Delta m^2 = 3eV^2$ and $sin^2(2\theta) = 3.0 \times 10^{-3}$ and the background from $\overline{\nu}_e$s from μ^- decay are 811 and 377 events, respectively. However, the backgrounds at the candidate site can be measured with some prototype detector like the 200 L Gd-loaded liquid scintillator detector. In order to confirm the reduction of background, the components below should be measured at the candidate site.

1. The beam associated neutron rate below several tens MeV and correlated gammas. The on-bunch rate is especially important.

2. Michel electron events induced by the high energy neutrons above 200 MeV.

3. Cosmic ray induced fast neutrons.

	background	R_i^{prompt} (/spill)
Prompt like signals	e^- $(^{12}C(\nu_e, e^-)^{12}N_{g.s.})$	8.0×10^{-6}
	e^- $(^{12}C(\nu_e, e^-)^{12}N^*)$	3.8×10^{-6}
	e^+ $(\bar{\nu}_e$ from $\mu^-)$	$< 10^{-6}$
	R_{prompt}	1.3×10^{-5}/spill
	background	$R_i^{delayed}$ (/spill)
Delayed like signals	Gamma (Beam associated)	4.7×10^{-2}
	Neutron (Beam associated)	2.4×10^{-3}
	e^+ $(^{12}C(\nu_e, e^-)^{12}N_{g.s.})$	1.2×10^{-5}
	Spallation products	$\sim 10^{-4}$
	$R_{delayed}$	4.9×10^{-2}/spill
R_{acc}		4.8/year

Table 8: Values for calculation of the accidental background rate per one detector.

7   Neutrino Oscillation Sensitivity

As discussed in previous section, the dominant background is $\bar{\nu}_e$ from μ^- decay in the MLF experiment. Others are estimated carefully, e.g. from the neutrinos, however those backgrounds can be neglected for the sensitivity fit study at this stage since the fraction of each background component is less than 10% of the $\bar{\nu}_e$ from μ^- decay background.

For the fit of the oscillation parameters, Δm^2 and $\sin^2(2\theta)$, constraints of the background normalization are important. However, $\bar{\nu}_e$ from μ^- has a very poor normalization constraint from the external information since the stopping point of μ^- decays and pion production are not known well, even when using MC simulation. Therefore, the uncertainty of the normalization factor for this background is taken to be 50%. (See section 3 in deails)

On the other hand, the cross section for the $\nu_e + {}^{12}C \rightarrow e + {}^{12}N_{gs}$ reaction is known at the 2% level [27]. The lifetime of $N_{gs}\beta$ decay and the e^- energy spectrum are also well known, as shown before. The measurement of the reaction provides the normalization factor for the oscillated signal $(\bar{\nu}_e + p \rightarrow e^+ + n)$ since the parent particle for the oscillated signal is $\bar{\nu}_\mu$ from μ^+ decays $(\mu^+ \rightarrow e^+ + \bar{\nu}_\mu + \nu_e)$. Note that the determination of the normalization factor can be done at the 10% level; even disappearance oscillations, if they occur, should be small (less than 10%).

7.1   Fit method

The binned maximum likelihood method is used for the analysis. The method fully utilizes the energy spectrum of each background and signal components, thus the amount of the signal components can be estimated efficiently.

The typical energy spectrum from μ^- (blue), the oscillated signal with $(\Delta m^2, \sin^2 2\theta) = (3.0, 0.003)$ (brown shaded; best Δm^2 case (left)) and (1.2, 0.003) LSND best fit case (right)), $^{12}C(\nu_e, e^-)^{12}N_{gs}$ (red) are shown in Fig. 38. Here we assume the
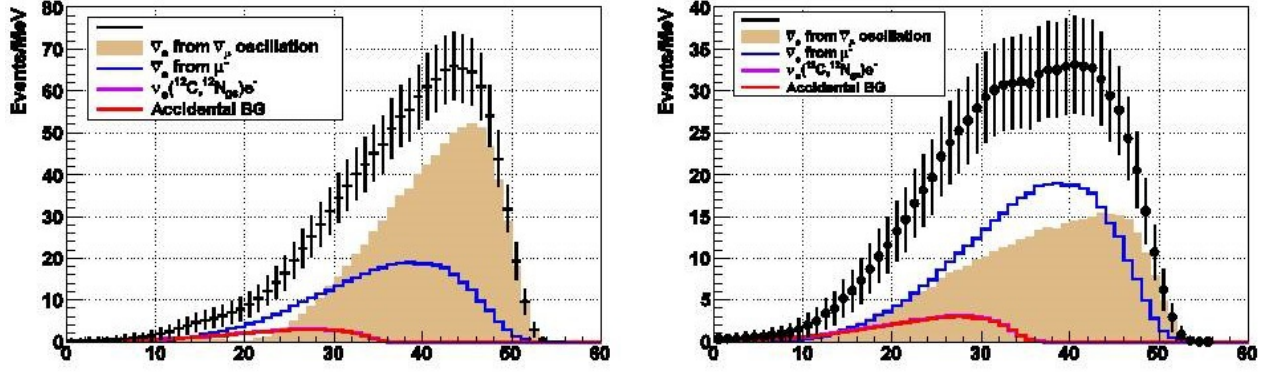
Figure 38: The typical energy spectrum from μ^- (blue), the oscillated signal with $(\Delta m^2, \sin^2 2\theta) = (3.0, 0.003)$ (brown shaded; best Δm^2 for the MLF experiment (left)), $(1.2, 0.003)$(LSND best fit point (right)), $^{12}C(\nu_e, e^-)^{12}N_{gs}$(red) are shown. Black points with error bar correspond to the sum of the all components. Positron energy is smeared by $15.0\%/\sqrt{E}$ for the detector effect.

fiducial mass of the detector is 50 tons, 1MW beam power at MLF, and four years operation with 4000 hours in the beam exposure time during each year. The signal detection efficiency is assumed to be 48%. The detector is put at the distance 17 m from the target. The number of events at each energy bin is still statistically small, therefore we use maximum likelihood instead of the usual minimum χ^2 method. The fitter estimates the oscillation parameters by varying the size and shape of the brown part to best reproduce the energy distribution of the black points.

For this purpose, the following equation is used.

$$L = \Pi_i P(N_{exp}|N_{obs})_i \tag{13}$$

$$P(N_{exp}|N_{obs}) = \frac{e^{-N_{exp}} \cdot (N_{exp})^{N_{obs}}}{N_{obs}!} \tag{14}$$

where, i corresponds to i-th energy bin, N_{exp} is expected number of events in i-th bin, N_{obs} is number of observed events in i-th bin. i is starting from 20 MeV and ends at 60 MeV because the energy cut above 20 MeV is applied for the primary signal as explained above. Note that $N_{exp} = N_{sig}(\Delta m^2, \sin^2 2\theta) + \sum N_{bkg}$, and $N_{sig}(\Delta m^2, \sin^2 2\theta)$ is calculated by the two flavor neutrino oscillation equation as shown before, $P(\bar{\nu}_\mu \to \bar{\nu}_e) = \sin^2 2\theta \sin^2(\frac{1.27 \cdot \Delta m^2 (eV^2) \cdot L(m)}{E_\nu(MeV)})$.

The maximum likelihood point gives the best fit parameters, and $2\Delta lnL$ provides the uncertainty of the fit parameters. As shown in the PDG [28], we have to use the $2\Delta lnL$ for 2 parameter fits to determine the uncertainties from the fit.

7.2 Systematic uncertainties

Equation 13 takes only statistical uncertainty into account, therefore the systematic uncertainties should be incorporated in the likelihood. Fortunately, energy spectrum of the oscillated signal and background components are well known, thus

the error (covariance) matrix of energy is not needed. In this case, uncertainties of the overall normalization of each component have to be taken into account, and the assumption is a good approximation at this stage.

In order to incorporate the systematic uncertainties, the constraint terms should be added to Equation 13 and the equation is changed as follows.

$$L = [\Pi_i P(N'_{exp}|N_{obs})_i] \times e^{-\frac{(1-f_1)^2}{2\Delta\sigma_1^2}} \times e^{-\frac{(1-f_2)^2}{2\Delta\sigma_2^2}} \tag{15}$$

where f_j are nuisance parameters to give the constraint term on the overall normalization factors. $N'_{exp} = f_1 \cdot N_{sig}(\Delta m^2, \sin^2 2\theta) + f_2 \cdot N_{bkg}$. $\Delta\sigma_i$ gives the uncertainties on the normalization factors of each components. In this proposal, the profiling fitting method is used to treat the systematic uncertainties. The method is widely known as the correct fitting method as well as the marginalizing method. The profiling method fits all nuisance parameters as well as oscillation parameters.

As mentioned above, the flux of the $\bar{\nu}_e$ from μ^- decays around the mercury target has very poor constraints from the external information. For this situation, the uncertainty of this background component is assigned to be 50%.

Table 9 shows the summary of the uncertainty of the normalization factors for the signal and background components. They are regarded as inputs of $\Delta\sigma$ although only $\bar{\nu}_e$ from μ^- is used in this proposal as mentioned above.

components	uncertainty	comments
signal	10%	normalized by ν_e from μ^+
$\bar{\nu}_e$ from μ^-	50%	
$\nu_e + ^{12}C \rightarrow e + ^{12}N_{gs}$	$<<10\%$	for correlated BKG
$\nu_e + ^{12}C \rightarrow e + ^{12}N_{gs}$ + delayed acc.	$<<10\%$	if delayed BKG is known within 10%
$\nu_e + ^{12}C \rightarrow e + ^{12}N^*$	20%	
cosmic / beam	5%	well known from calibration source

Table 9: Summary of uncertainties on the normalization factors. Note that only $\bar{\nu}_e$ from μ^- are used in the fitting in this proposal since it is dominant one.

7.3 Sensitivity

In order to obtain the experiment's sensitivity, we assume there is no oscillation signal in the pseudo-data, and then calculate $2\Delta ln(L)$ from the maximum $2ln(L)$ points. In this case, the maximum $2ln(L)$ point stays at $\sin^2 2\theta = 0.000$. The points, which have $2\Delta ln(L)$ to be 11.83 in ($\sin^2 2\theta, \Delta m^2$) 2D plane correspond to the 3 σ case. (28.76 for 5 σ case)

Fig. 39 shows the sensitivity of our experiment with 3 (green) and 5 σ (blue), respectively. A top plot shows the case with 2 years exposure, while the bottom plot shows the that with 4 years.

If no definitive positive signal is found by this experiment, a future option exists to cover small Δm^2 region. This needs a relatively long baseline and requires a large detector to compensate for the reduced neutrino flux. (See appendix)

8   Milestone

The following measurements at the candidate site (the 3rd floor of the MLF building) are planned as a part of the feasibility test of the experiment.

1. Total amount of beam associated gammas and neutrons for the "IBD delayed" background.

2. Confirmation of reduction of Michel electrons compared to BL13.

3. Total amount of cosmic induced fast neutrons for the IBD correlated background.

According to PHITS simulation, the gamma and neutron rates are $\sim 10^6/\text{day/ton/1MW/100}\mu\text{s}$ each, while the Michel electron rate is $\sim 10^{-2}/\text{day/ton/1MW/9}\mu\text{s}$ compared to $\sim 10^3$ at BL13. The cosmic induced fast neutrons are measurable with self trigger, then the flux is expected to be $\sim 10\text{Hz/m}^2$. All materials are measureable using a 1 ton level detector. The measurement provides confidence for the experiment if the measured rate is consistent with the PHITS simulation.

9   Cost estimation

Here is the cost estimation.

Table 10: Cost estimation (2 detectors)

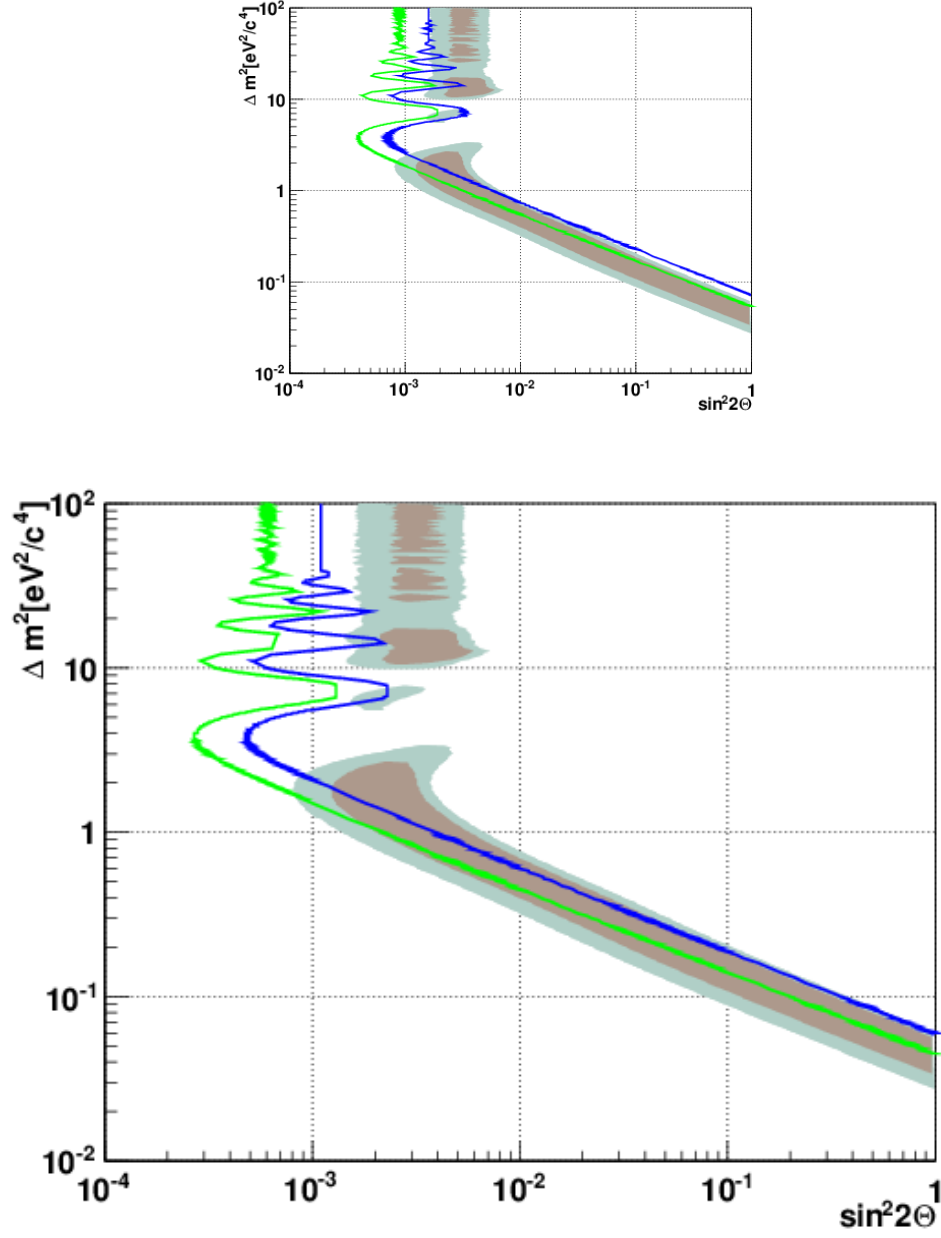| Item	Unit price	Quantity	Total
* PMTs & Electronics system :	500Ky/ch	400 ch	200My
* Tanks & Acrylic Vessels :	50My/set	2 sets	100My
* Gd-LS, Buffer-LS			100My
* Fluid handling and infrastructure	50My/set	1 set	50My
* Miscellaneous			50My
Grand Total			500My

Figure 39: The sensitivity of the MLF experiment assuming 2 and 4 years operations (4000 hours / year) assuming ~50% detection efficiency and 17 m baseline. The blue line shows the 5 σ C.L., while green one corresponds to 3 σ. Top plot shows the case with 2 years exposure, while the bottom plot shows that with 4 years.

A Test measurements of backgrounds at the MLF

A.1 MLF BL13; location of the measurement

A.2 1 ton plastic scintillation counters

A plastic scintillator detector was placed at BL13 in MLF to measure the background level of neutrons and photons as was shown in Fig. 9. We will describe the setup, the calibration and the obtained resolution of the 1 ton scintillator detector in the following subsections.

A.2.1 setup

Figure 40 shows a schematic view of the 1 ton plastic scintillator counters placed at BL13. It consists of 24 pieces of $10.5 \times 4.5 \times 460$ cm^3 scintillator and 14 pieces of $21.0 \times 4.5 \times 460$ cm^3 scintillator. Each end of the scintillators were viewed by PMTs. Signals from each PMT were recorded by 65 MHz FADC with 50 ns RC-filter.
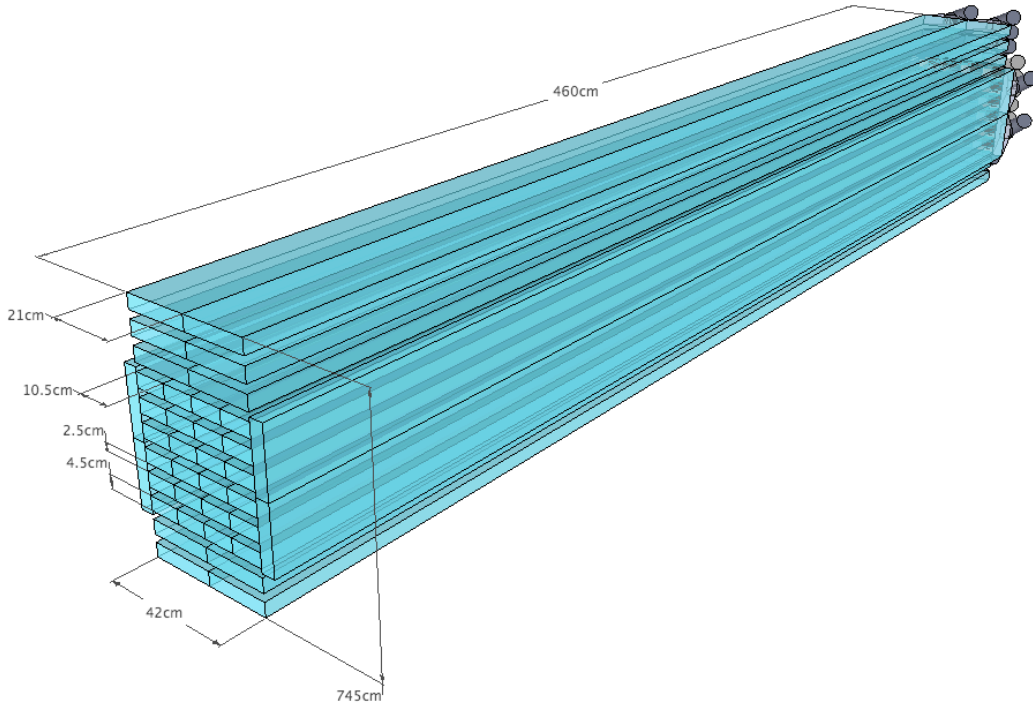

Figure 40: Schematic view of the 1 ton plastic scintillator counters. It consists of 24 pieces of 10.5 cm width and 14 pieces of 21.0 cm width scintillators. All of them are 460 cm long. Both ends of each scintillator were viewed by PMTs.

A.2.2   calibration

We used cosmic muons to measure the attenuation length of the scintillator, to calibrate energy and timing. We prepared 3 pairs of scintillator counters to trigger the cosmic rays. Figure 41 shows a schematic view of the cosmic muon trigger counters.
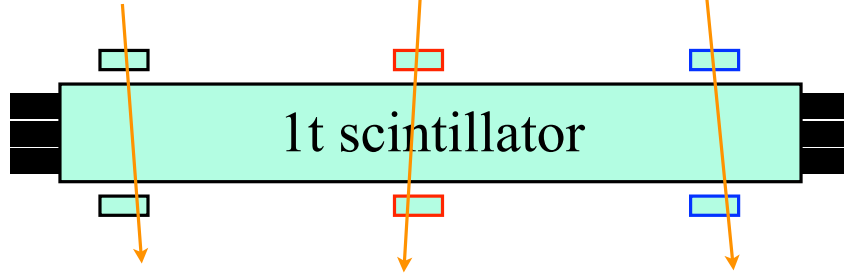

Figure 41: Schematic view of the cosmic muon trigger counters. We prepared 3 pairs of plastic scintillators to trigger cosmic muons.

We made some dedicated runs to measure the attenuation length of the scintillators. In some of the dedicated runs, we changed the position of the trigger counters along the beam axis. Figure 42 shows a measured typical attenuation curve. We measured the curve and parameterized one for each scintillator. By considering the attenuation length, the reconstructed charge was independent from the incident position as shown in Fig. 43.
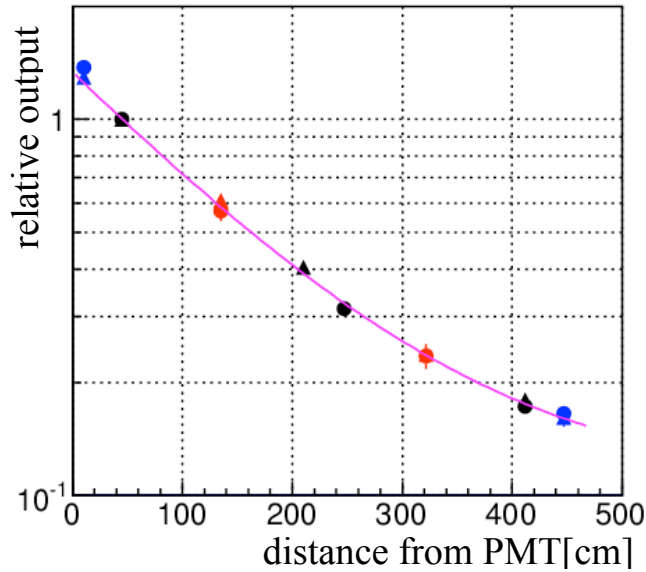

Figure 42: Typical measured attenuation curve for a certain scintillator. We measured the curve and parameterized one for each scintillator (magenta line).

We also aligned the timing of each PMT. Time offsets were determined to minimize the time difference between each pair of PMTs on each end. The velocity of
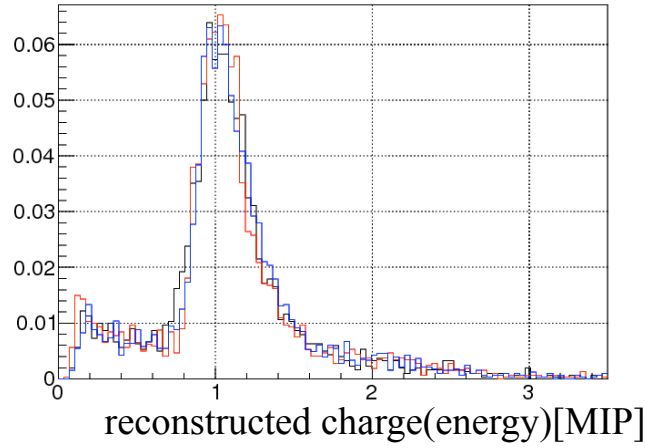
57

Figure 43: Reconstructed charge for different incident positions by considering the measured attenuation length. The MIP energy for the 4.5 cm thick scintillator is 8 MeV. The colors correspond to the events triggered by the cosmic muon counters shown in Fig. 41.

cosmic muons passing through the detector was considered. Figure 44 shows the time difference between scintillators for cosmic ray events. The timing of each PMT and scintillator was well calibrated. The light velocity in each scintillator was also measured. The typical velocity was 15 cm/ns.

A.2.3   resolution

We evaluated the obtained energy resolution by smearing the output of the pure Monte-Carlo simulation, and comparing it with data. Figure 45 shows a schematic view of the estimation procedure of the energy resolution. We parameterized the energy resolution as follows:

$$\frac{\sigma_E}{E} = \frac{p_0}{\sqrt{E}} \oplus \frac{p_1}{E} \oplus p_2, \tag{16}$$

where p_0 represents the photo-statistics term, p_1 represents the noise contribution and p_2 represents the calibration precision. The charge distribution at 3 different position along the beam axis were compared for each PMT. Because only one PMT was in interest at a time, we set $p_2 = 0$. We fitted the charge distributions by changing the rest of parameters, and obtained the light yield $n_{p.e.} \sim 30$ p.e./MeV and the equivalent noise level $\sigma_{\text{noise}} \sim 0.15$ MeV at 45 cm from the PMT (typical values).

We also evaluated the obtained position resolution and timing resolution. The hit position in a scintillator along the beam direction was calculated by using the time difference between PMTs on both ends of the scintillator. Figure 46 shows the reconstructed hit position in the scintillators of cosmic ray events for different incident positions. The obtained position resolution has slight position dependence because of the light attenuation in the scintillators. The obtained position resolution around the middle of the scintillator for MIP energy was $\sigma_x = 17$ cm. By considering

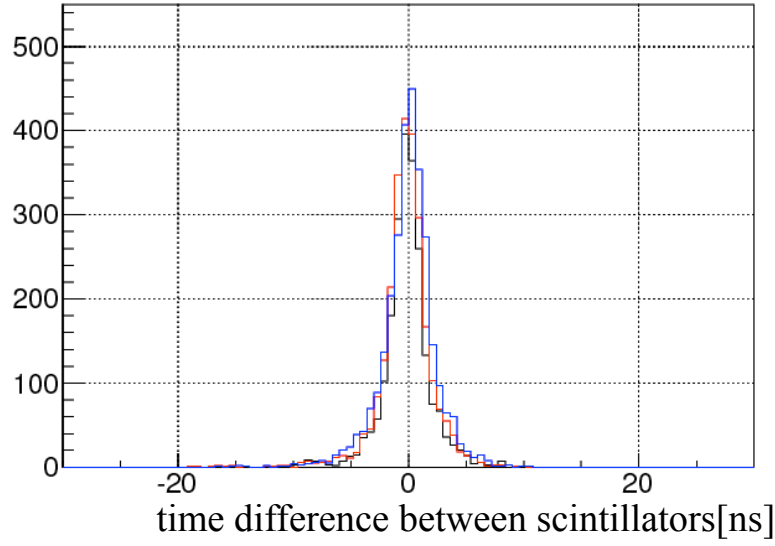Figure 44: Time differences between scintillators of cosmic ray events for different incident positions. The colors correspond to the events triggered by the cosmic muon counters shown in Fig. 41.
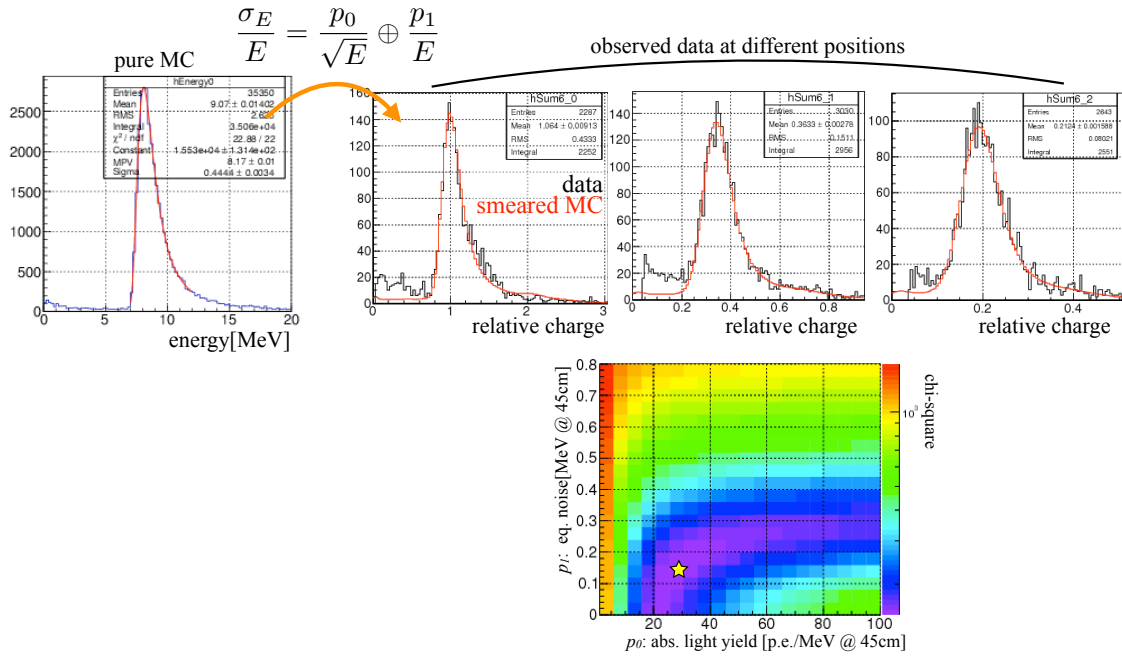

Figure 45: Schematic view of the estimation procedure of the energy resolution. The charge distribution at 3 different positions along the beam axis for the cosmic muon events were compared with the smeared MC outputs.

59

the observed light velocity in the scintillator 15 cm/ns, the timing resolution of the scintillator for MIP energy is $\sigma_t = 1.1$ ns.
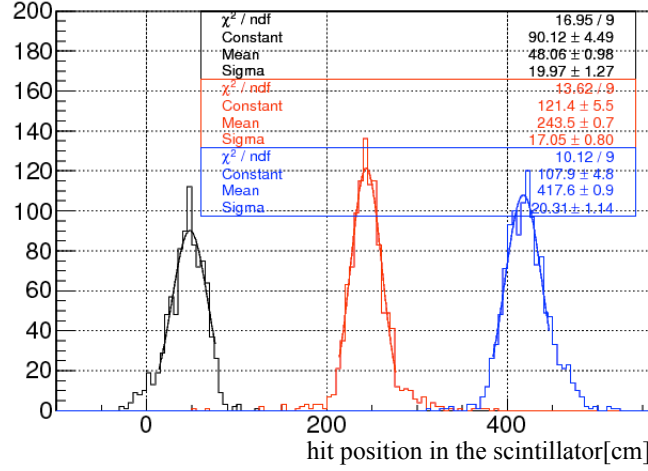
Figure 46: Reconstructed hit positions along beam direction of cosmic ray events for different incident positions. The colors correspond to the events triggered by the cosmic muon counters shown in Fig. 41.

A.3   NaI counter (370 g)

The NaI counter measured environmental γ at BL13. The NaI counter was located on the floor of BL13 near downstream side of the 1 ton detector with respect to the beam and the opposite side of the 1 ton detector with respect to BL14. The NaI crystal is a cylinder with diameter of 2 inch and thickness of 2 inch. Pulse heights of signals from a PMT are measured by a multi channel analyzer (MCA) through a preamplifier, a spectroscopy amplifier and a linear gate and stretcher module. Based on the pulse heights, a histogram of the pulse heights with 1024 bins is made with a PC. Energy calibration was done using peaks of environmental γ, such as 1.461 MeV γ of ^{40}K and 2.615 MeV γ of ^{208}Tl. Energy resolution is about $3\%/\sqrt{E[\text{MeV}]}$, estimated using Geant4.

B   Event generator and detector simulation

B.1   MC simulation

B.1.1   Event generator

Event generators are tools built to select the energy and momentum of the particles produced in the reactions expected in the detectors, which will be the entry for the MC simulations. The selection of the particle's energy and momentum method follows the flux distribution and cross-sections values, found in many different references. The tools also generates a random interaction point in the detector, based on its geometry, which is used to calculate the baseline value and momentum direction. All of them are build using the ROOT libraries, and some details of each is define in the following subsections.

Signal   The signal search in the experiment is a $\bar{\nu}_e$, which oscillated from a $\bar{\nu}_\mu$ state, interaction. Therefore, its spectral shape will be the same as the one for $\bar{\nu}_\mu$, from a μ^+ decay at rest, described by:

$$\frac{d\Gamma}{dE_{\bar{\nu}_\mu}} \sim E_{\bar{\nu}_\mu}^2 \left(3 - 4 \frac{E_{\bar{\nu}_\mu}}{m_\mu} \right) \tag{17}$$

which comes from the weak theory calculations of the μ decay, and it is represented in left of figure 47. The interaction cross-section is the Inverse Beta Decay (IBD) one,
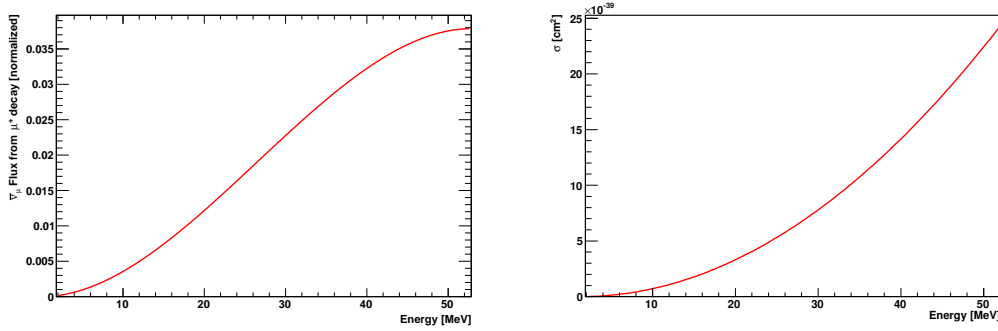
Figure 47:   Flux shape of the $\bar{\nu}_\mu$ produced in the μ^+ decay, on the left, and the IBD energy dependence of the cross-section, on the right.

which is:

$$\sigma_{\mathrm{IBD}} = \frac{2\pi^2/m_e}{f_{p.s.}^{\mathrm{R}} \tau_n} E_e p_e \tag{18}$$

where τ_n is the measured neutron lifetime and $f_{p.s.}^{\mathrm{R}} = 1.7152$ is the phase space factor, including the Coulomb, weak magnetism, recoil, and outer radiative corrections, being depicted in right of figure 47. An expression of the cross section depending also on the angle between the neutrino and the emitted positron can be found in [16]. Based on

the above information, a suitable energy for the neutrino can be chosen and following the kinematics of the IBD process, the positron and neutron energy and momentum can also be inferred. Figure 48 shows an example of the positron and neutron energy distribution for the signal events.

Figure 48: Positron (left) and neutron (right) energy distribution after IBD interactions, where the $\bar{\nu}_e$ comes from an oscillated $\bar{\nu}_\mu$ state.
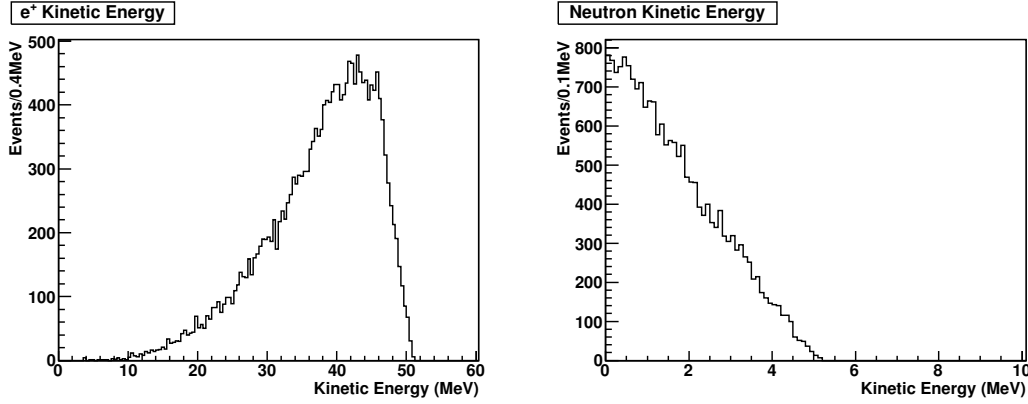
$\nu_e({}^{12}\mathrm{C},{}^{12}\,\mathrm{N_{g.s.}})e^-$ **BG** ν_e's comes from the μ^+ decay and they can interact with the ${}^{12}\mathrm{C}$ of the detector's liquid scintillator, resulting in a ${}^{12}\mathrm{N}$ and an electron, i.e.

$$\nu_e +{}^{12}\mathrm{C} \rightarrow e^- +{}^{12}\mathrm{N_{g.s.}},{}^{12}\,\mathrm{N_{g.s.}} \rightarrow^{12} C + e^+ + \nu_e \tag{19}$$

The nitrogen will be produced in the ground state in about 95% of the cases, and it will decay in a positron. This decay has an end point energy of ~ 16 MeV a half-life of 16 ms. Therefore one needs to know the energy of the incident ν_e to calculate the energy and momentum of the electron, and the description of the nitrogen-12 β^+ decay, for the positron.

As for the signal case, the ν_e from a μ^+ decay has the well known energy spectrum:

$$\frac{d\Gamma}{dE_{\nu_e}} \sim E_{\nu_e}^2 \left(1 - 2\frac{E_{\nu_e}}{m_\mu}\right) \tag{20}$$

which is represented in figure 49. The positron spectrum is defined as equation 21:

$$\frac{d\mathrm{N}}{dE_e} = P_e E_e (E_{\mathrm{max.}} - E_e)^2 \frac{2\pi\eta}{e^{2\pi\eta} - 1} \tag{21}$$

where

$$\eta = \frac{Z\alpha}{\beta_e}. \tag{22}$$

The positron spectrum generated by the equation is shown in **??**. 50.

The interaction cross section between the neutrino and the carbon atom has a shape as defined in figure 51.
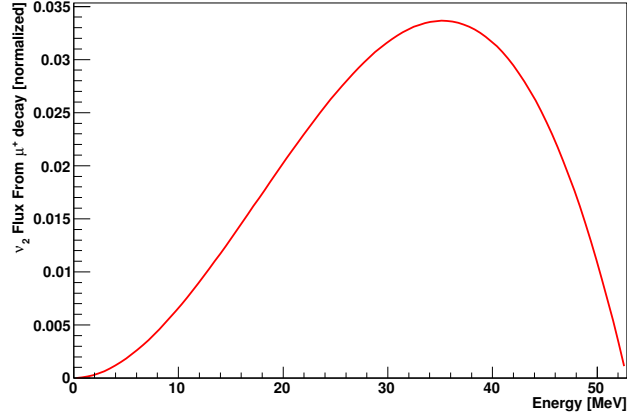
Figure 49: The energy spectrum of ν_e from μ^+ decay.
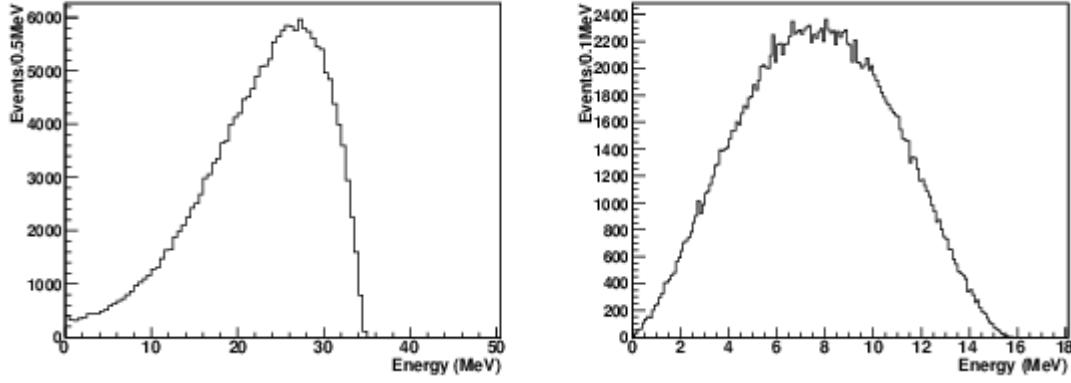
Figure 50: Electron and positron energy distribution for the $\nu_e(^{12}\mathrm{C},^{12}\mathrm{N_{g.s.}})e^-$ process. On the left the electron energy is calculated using the kinematics of reaction, and on the right, the positron energy comes from the $^{12}\mathrm{N}$ decay, as described by equation 21.
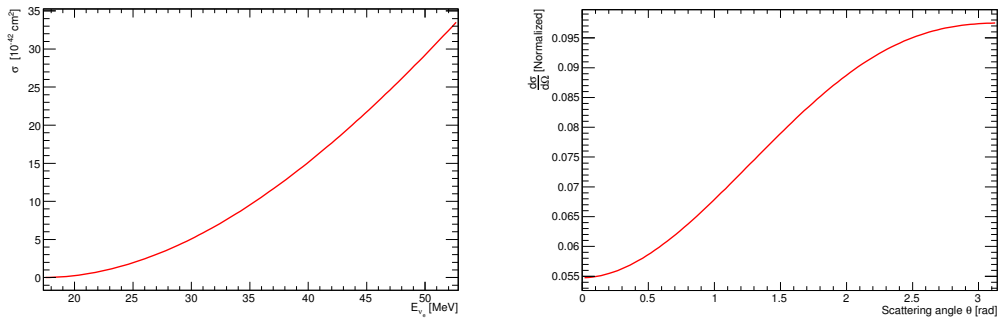
Figure 51: Cross section of the $\nu_e(^{12}\mathrm{C},^{12}\mathrm{N_{g.s.}})e^-$ reaction. On the left is the dependence on the neutrino energy and on the right on the angle between the neutrino and the emitted electron [32].

$\bar{\nu}_e$ **from** μ^- **decay BG**   Although the μ^- is absorbed before its decay, a small fraction of them can decay emitting $\bar{\nu}_e$ that will mimic a true $(\bar{\nu}_\mu \rightarrow \bar{\nu}_e)$ oscillation. The energy spectrum is also define as shown in equation 20 and the interaction process is the IBD, as for the signal case, having similar distributions as shown in figures 49 for the neutrino and figure 48 for the IBD products.

Environmental Gammas   For the MC simulation of environmental gammas, each of ^{238}U, ^{232}Th series, 30 γ-ray energies having largest branching ratios are considered [33], and for ^{40}K, single γ-ray of 1.461 MeV are generated in the MC simulation. In this proposal, as main environmental gamma sources, gammas from the PMT glass surface and various materials outside of the detector. For the PMT glass surface, this generator was used. Concentrations of ^{238}U, ^{232}Th and ^{40}K in the PMT glass are 13ppb, 61ppb and 3.3ppb, respectively. The gammas are generated isotropically. Meanwhile, for the gammas from out side of the detector, it is difficult to generate them precisely from all materials at the experimental site because the geometry is complicated. So assuming that most material generating the gammas is concrete, and the thickness is above 50 cm at least considering with the self shielding of the gammas, the gammas from outside of the detector are generated based on the energy spectrum after passing through 50 cm of the concrete calculated by the MC simulation with this generator. Concentrations of ^{238}U, ^{232}Th and ^{40}K in the PMT glass were calculated by fitting with sum energy spectrum weighted by the concentrations of ^{238}U, ^{232}Th and ^{40}K to measured energy spectrum with the NaI measurement at BL13.

Cosmic muon   Cosmic-ray muon generator is based on study by J. Kempa and A. Krawczynaka [34]. The flux I[cm^{-2}s^{-1}sr^{-1}(GeV/c)$^{-1}$] is expressed as a function of the momentum p_μ[GeV/c] and zenith angle θ (deg) by

$$logI = aln^2 p_\mu + blnp_\mu + c, \tag{23}$$

where a and b are given by

$$Y = p_1/(1/\theta + p_2\theta) + p_3 + p_4exp(-p_5\theta), \tag{24}$$

where Y means a or b respectively. c is given by

$$c = p_1\theta^2 + p_2\theta + p_3 + p_4exp(-p_5\theta). \tag{25}$$

The coefficients p_1,p_2,p_3,p_4 and p_5 are listed in Table 11. The generated position is determined by randomizing in a disk with diameter of 60m and at the height of 6m from ground level.

Cosmic induced fast neutron   In order to estimate the cosmic muon induced fast neutron events rate entering in the detector at the candidate site(see Appendix C), empirical functions depending on the muon energy(E_μ) in reference [30] are used for generating kinetic energy spectrum(E_n), multiplicity(M) and angular distribution(θ) of the fast neutrons for the MC simulation. Fig. 52 shows distributions of the kinetic

Table 11: The values of the coefficients of a,b and c.

p_i	a	b	c
p_1	-0.8816×10^{-4}	0.4169×10^{-2}	-0.3516×10^{-3}
p_2	-0.1117×10^{-3}	-0.9891×10^{-4}	-0.8861×10^{-3}
p_3	0.1096	4.0395	-2.5985
p_4	-0.1966×10^{-1}	4.3118	-0.8745×10^{-5}
p_5	0.2040×10^{-1}	-0.9235×10^{-3}	-0.1457

energy, multiplicity and zenith angle. Then the kinetic energy spectrum, multiplicity and angular distribution are defined as functions 26, 28 and 27.

$$\frac{dN}{dE_n} = A(\frac{e^{-7E_n}}{E_n} + B(E_\mu)e^{-2E_n}), \tag{26}$$

where A is a normalization factor, and $B(E_\mu) = 0.52 - 0.58e^{-0.0099E_\mu}$.

$$\frac{dN}{dM} = A(E_\mu) = 0.85 + 0.54e^{0.075E_\mu}, \tag{27}$$

where $A(E_\mu) = 0.085 + 0.54e^{-0.075E_\mu}$, $B(E_\mu) = \frac{27.2}{1+7.2e^{-0.076E_\mu}}$, $C(E_\mu) = 0.67 + 1.4e^{-0.076E_\mu}$.

$$\frac{dN}{dcos\theta} = \frac{A}{(1-cos\theta)^{0.6} + B(E_\mu)} \tag{28}$$

where $B(E_\mu) = 0.699E_\mu^{-0.136}$. Then, the fast neutron events were generated uniformly from cylindrical surface with 3.2m of the radius and 6.4m of the height(1m outside from the SUS tank surface).

B.1.2 Detector simulation

Detector simulation In this proposal, Geant4 was used for detector simulation study [19]. Geant4 is C++ class library produced by CERN, which provides a calculation of particle tracking in materials. Detector simulator was based on Geant4 (The version is 4.9.0.p1.). The simulator computes interactions between incident particles and the detector materials, and also trajectory of optical photons emitted by the scintillation radiation process. For the hadronic interaction process, QGSP BIC HP model was employed in Geant4. It comprehends from low energy region under 20MeV such as behavior of thermal and fast neutron to high energy region such as interactions between cosmic-ray muons and materials around the detector. The simulator also follows the trajectory of optical photons emitted in the liquid scintillator due to ionization by charged particles, the optical process includes attenuation and scattering of the photons. The number of these incident photons and the timing for each PMT are stored in the simulator after reduction due to the quantum efficiency($\sim$20%).

Time distribution of the scintillation lights emission is assumed as sum of 2 exponentials with fast and slow time constants of the liquid scintillator. The fast and
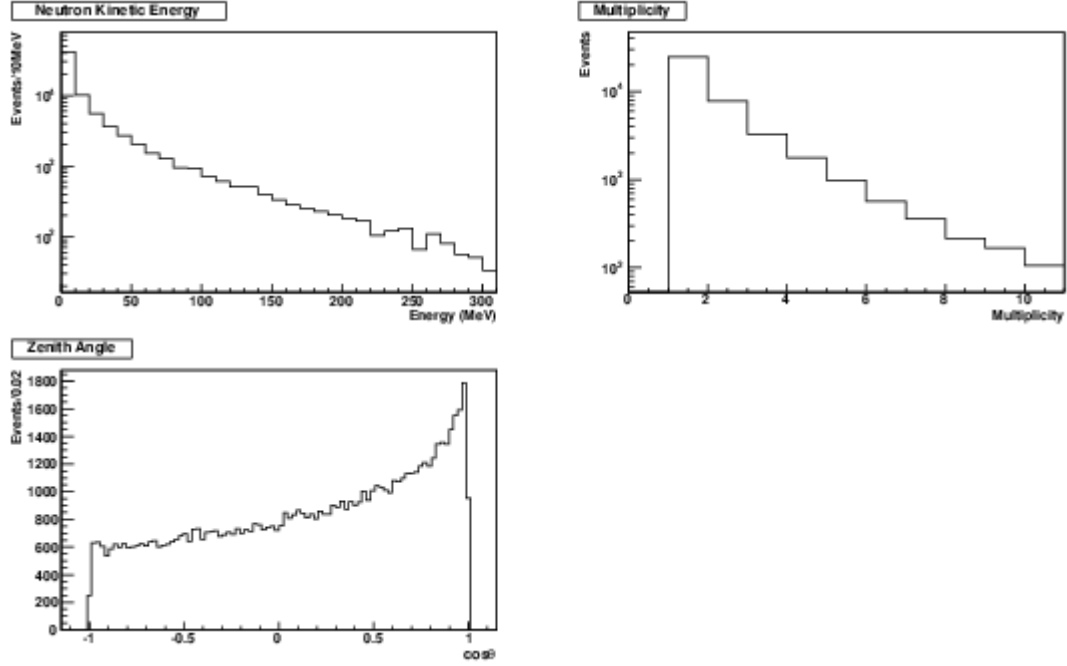
Figure 52: Distributions of the neutron kinetic energy(upper left plot), multiplicity(upper right plot) and zenith angle (lower plot) of the cosmic muon induced fast neutron events generated by the empirical functions in the reference [30].

slow time constants are 3.6ns and 270ns, respectively, and ratio of the fast and slow constants is 0.57.

Pulse generation The hit times for each PMT from the Geant4 output are shifted with transit time (TT~60ns) and smeared following Gaussian distribution with transit time spread (TTS~2.9ns) for the 10inches PMT(HAMAMATSU R7081) in the data sheet. One photoelectron pulse was reconstructed assuming Landau distribution, then the shifted and smeared time were used for mean time of the Landau function, and the sigma estimated by Double Chooz group was used in our sigma. One pulse for each PMT was reconstructed as sum of the one photoelectron pulses. Fig 53 shows an example of the one pulse for each PMT. Finally, the pulse shape depends on sum time distributions of the scintillation lights emission of fast and slow component in previous paragraph.

C   Estimation of cosmic muon induced backgrounds events

Neutron and some unstable isotopes are produced by reactions between cosmic muon and nuclei(especially ^{12}C) inside the organic liquid scintillator or materials at the experimental site(spallation products). Then especially, IBD mimic signals are induced by fast neutron produced by the reaction between the muon and materials outside of the detector. Basically, neutron produced inside the detector and short-lived unstable
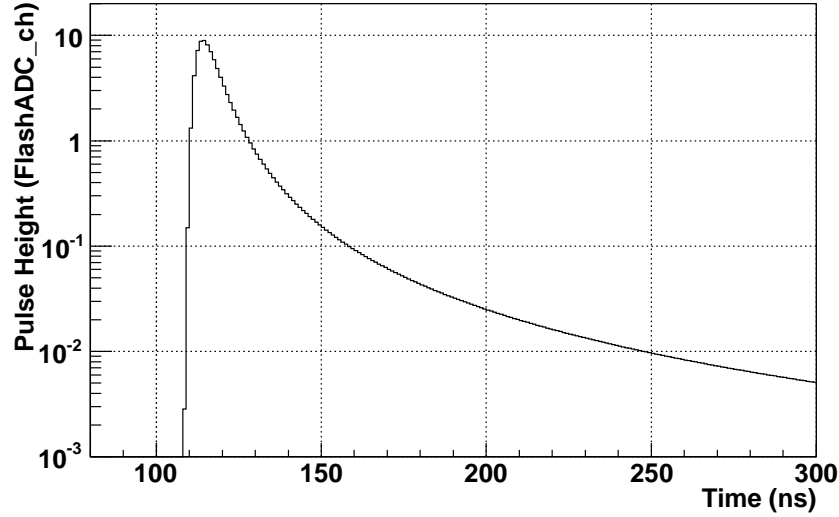
66

Figure 53: An example of the reconstructed MC pulse of PMT.

isotopes can veto because the detected signals include parent muons passing through the detector, so they do not contribute to IBD mimic signals.

C.1 Fast neutron from outside of the detector

In this proposal, in order to estimate the fast neutron rate at the candidate site, we used measured data of the fast neutron above ground with the 200L Gd-loaded liquid scintillator detector at an experimental room in Tohoku Univ. [29], because we have not carried out some background measurement at the candidate site yet. Basically, the fast neutron flux is related to muon energy, flux depending on depth of experimental site and atomic elements composing materials in the experimental site. We think that we can estimate order of magnitude of the fast neutron flux by using the measured data above ground in Tohoku Univ. at least, even if geometry and materials of the experimental room in Tohoku Univ. are differ from ones of the candidate site. In near future, we will carry out background measurement with same detector at the candidate site in near future, then we will estimate the fast neutron flux more precisely. The fast neutron candidates from outside of the detector are events after applying selection criteria, which are $4 < E_{prompt} < 100 MeV$, $4 < E_{delayed} < 10 MeV$ and $10 < \Delta t < 200 \mu s$. Fig. 54 shows energy spectra of the prompt and delayed signals, and the Δt distribution after applying the selection criteria. Excesses of black lines in Fig. 54 show the correlated events. The excess in the prompt energy spectra distribute until high energy range above 100MeV. The excess in the delayed energy spectra distribute below around 8 MeV, which is sum of energies of gammas generated via thermal neutron capture on Gd. Most events below 4MeV is environmental gammas. The excess of the Δt distributions has two

67

components, which distribute based on exponentials with 2.2 μs of muon life time and about 100 μs of the thermal neutron capture time on Gd. The selection criteria was defined considering with reducing the environmental gammas and Michel electrons after muon decays in the detector. The absolute fast neutron flux was calculated
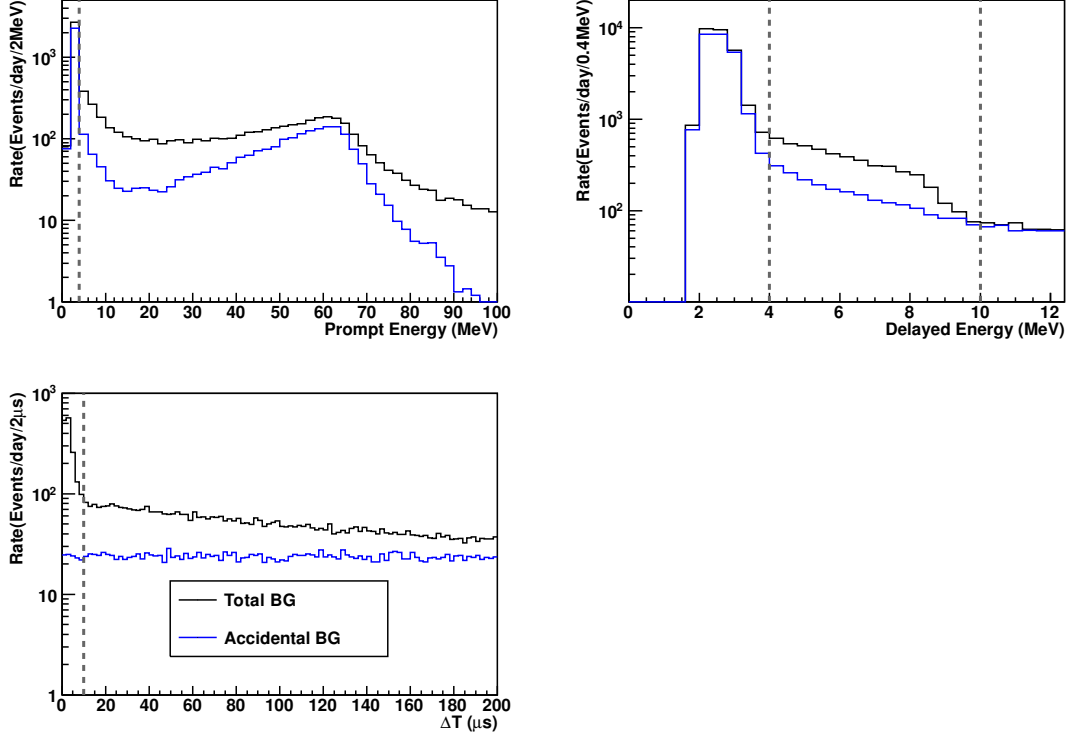

Figure 54: Energy spectra of the prompt(left upper) and delayed signals(right upper), and the Δt distribution(lower) of muon induced fast neutron candidates with the 200L Gd-loaded liquid scintillator detector. Gray dashed lines show the cut condition. Black lines show the candidates including both correlated and accidental events. Blue lines show only accidental events estimated by off time coincidence [29].

by χ^2 fitting with the excess of Δt distribution of the fast neutron candidates above 30MeV of the prompt energy in measured data to one in the MC samples with the fast neutron generator based on a reference [30](see B.1.1). Fig. 55 show comparison of distributions of each variables between the measured data and the MC samples scaled by the neutron flux calculated by the fitting. The prompt energy spectra of measured data and MC samples do not correspond in whole range below 100MeV. Events around several tens MeV include not only fast neutrons entering from outside of the detector but also muon events following neutrons produced inside the detector, because the detector does not implement veto counter for cosmic muons, the muon events following neutrons are remaining in the selection criteria. And the prompt energy spectra of measured data in KARMEN experiment and the MC samples with this generator do not correspond in the lower energy range [30]. So the fast neutron candidates above 30 MeV of the prompt energy was considered conservatively, and The Δt distributions were used for the fitting because the distribution is known as

a exponential depending on the thermal neutron capture time on Gd. Then the fast neutron flux is 17 Hz/m^2. Then the uncertainty of the fitting is $\sim$3 %. Fig. 56
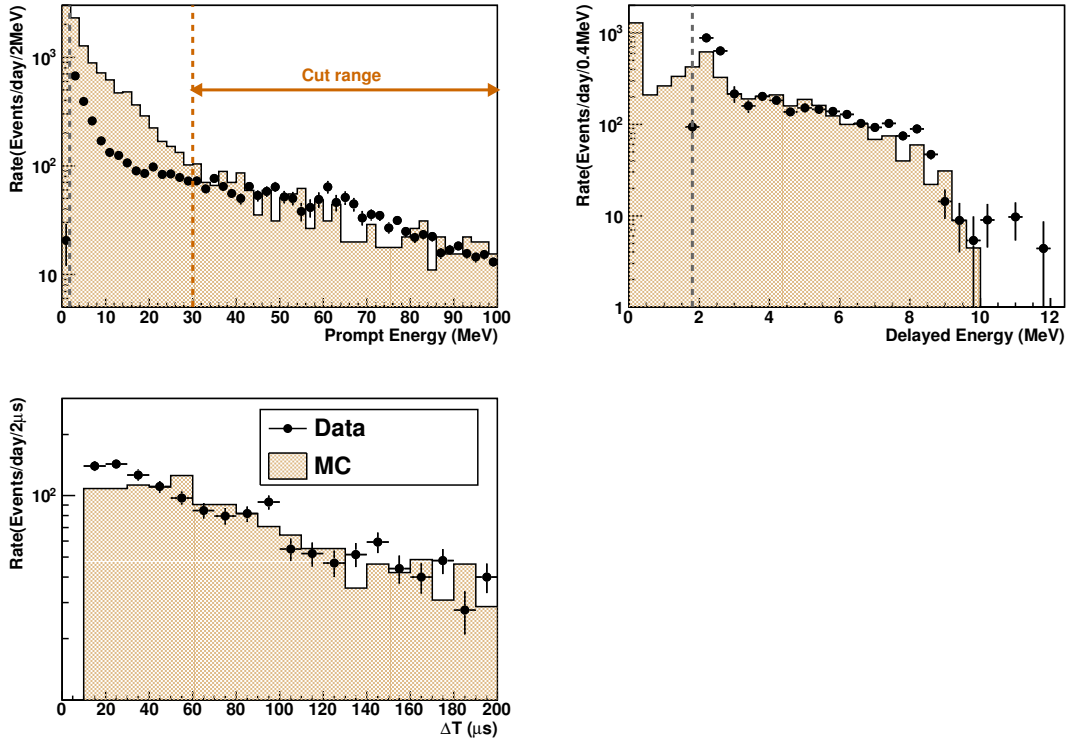

Figure 55: Comparison of distributions of each variables between the measured Tohoku data and the MC samples scaled by the neutron flux calculated by the fitting. Upper left and right figures show the prompt and delayed energy spectra. Lower figure shows the Δt distribution. Gray lines show the energy threshold level.

shows the energy spectra of prompt and delayed signals, and Δt distribution of MC samples for the detector of MLF experiment. The neutron events were generated from cylindrical surface of the SUS tank with the fast neutron generator. Finally, the fast neutron rate entering in surface of the SUS tank is expected to be 747 Hz. The remaining events rate after applying the neutrino selection criteria, is 0.68 Hz. Furthermore, it is effective for reducing the fast neutron events to apply that there is no veto signal, because sometime there are signals due to recoiled protons in the veto volume before entering the buffer volume. The rate after applying also no veto signal is reduced by $\sim$1/4, it is expected to be 0.16 Hz. But all of the rate do not contribute to the background rate, only coincidence rate with the beam timing contributes to the background rate. Then the coincidence rate(R_{coin}) considering with the prompt time window is calculated as follows.

$$R_{coin} = 0.16Hz \times 9.0\mu s = 1.4 \times 10^{-6}/spill \qquad (29)$$

Then, the number of the fast neutron events per year considering two detectors is $R_{con}\times$ 3.6$\times$ 10^8 $\times$ 2 detectors $\times$ 4 years = 4150 events. The real number of the fast neutron events will be measured in near future at the candidate site. Finally,
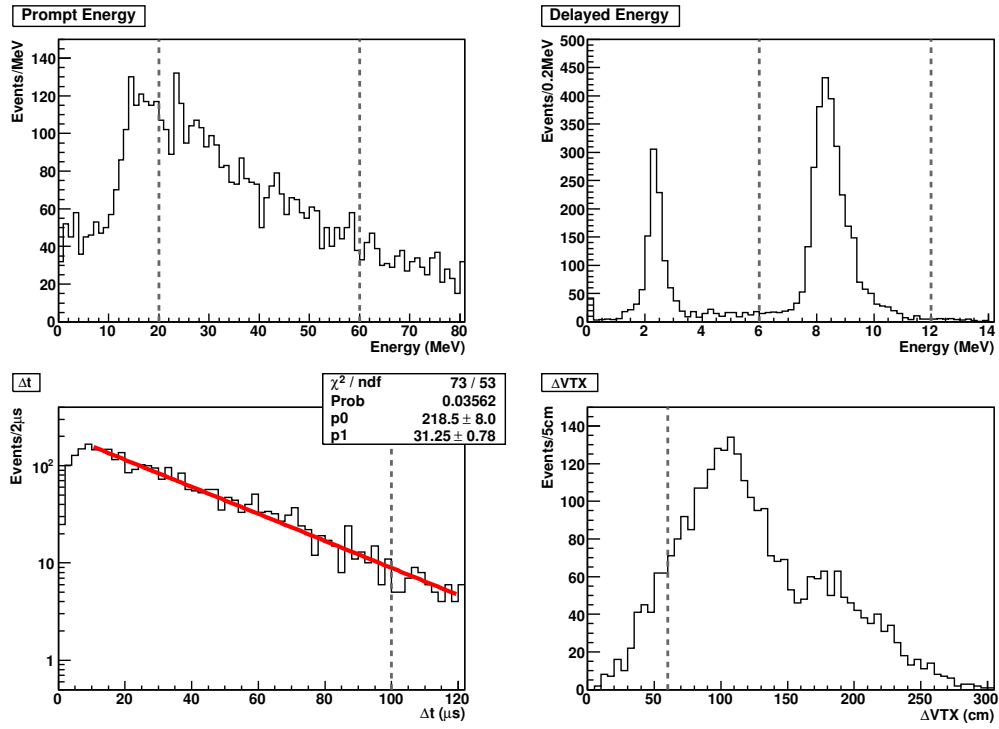
Figure 56: Energy spectra of prompt and delayed signals, and Δt distribution of the muon induced fast neutron events from outside of the detector. (The detector put at the 3rd floor of MLF (to be measured)

if there is several hundred events per year as above estimation, it is necessary to be reduced by several events per year. The number can be reduced by at least 1/100 by implementing some paraffin shielding with several tens cm of the thickness(can be reduced by ~1/10) and liquid scintillator with capability of particle identify like LSND experiments(can be reduced by ~1/100).

C.2 Spallation products

Rates of neutron and the long-lived unstable isotopes produced by the spallation reactions are related to muon energy, flux and carbon concentration in liquid scintillator. KamLAND group measured rates of the various isotopes [31], so the rates at the candidate site are extrapolated by below formula using ratios of target masses(M_i), mean muon energies(E_i), fluxes(ϕ_i) and carbon concentrations in the scintillator(N_i) between our experiment($i = JP$) and KamLAND($i = KL$). Values for the calculation show in Table 12. Then sum of the fiducial and gamma catcher masses was considered for the calculation.

$$R_{isotope}^{JP} = \frac{M_{JP}}{M_{KL}} \times \frac{N_{JP}}{N_{KL}} \times \left(\frac{E_{JP}}{E_{KL}}\right)^{\alpha} \times \frac{\phi_{JP}}{\phi_{LK}} \times R_{isotope}^{KL} \tag{30}$$

Where, α is a constant of power law for correlation between the mean muon energy and production rates of the spallation isotopes(α=0.74). The $R_{isotope}^{KL}$ of each isotope was calculated by using values in [31]. Considering the prompt energy cut range in the IBD selection criteria, the spallation products is expected to contribute the delayed like signals for the accidental backgrounds. Then the rate per spill for each isotope in 100 μs time window of the IBD selection is calculated as $R_{isotope}^{JP} \times 100\mu s$. Table 13 shows summary of the rates per spill per one detector. Basically, the spallation products are expected to be negligible as IBD mimic events.

Table 12: Values for calculation of rates of spallation products.

	M_i	N_i	E_i	ϕ_i
KamLAND (i=KL)	1000 (ton)	4.30×10^{22} (carbon/g)	260 (GeV)	1.49×10^{-3} (/m²/sec)
J-PARC (i=JP)	37 (ton)	4.30×10^{22} (carbon/g)	4 (GeV)	100 (/m²/sec)

%sectionCalibration

D Energy and Vertex Position Calibrations

The energy range to observe is 8 MeV to 53 MeV. Intrinsic non-linearity of the light output caused by the quenching effect and Cherenkov threshold effect is supposed

Table 13: Spallation products

Isotope	Life time	Radiation energy (MeV)	$R^{JP}_{isotope}$ (events/spill)
Neutron	-	8(Gd capture)	2.6×10^{-4}
^{12}B	29.1ms	13.4(β^-)	5.0×10^{-5}
^{12}N	15.9ms	17.3(β^+)	1.5×10^{-6}
^{8}Li	1.21s	16.0($\beta^-\alpha$)	3.9×10^{-5}
^{8}B	1.11s	18.0($\beta^-\alpha$)	1.1×10^{-5}
^{9}C	182.5ms	16.5(β^+)	1.9×10^{-6}
^{8}He	171.7ms	10.7($\beta^-\gamma n$)	5.6×10^{-7}
^{9}Li	257.2ms	13.6($\beta^-\gamma n$)	5.6×10^{-6}
^{11}Be	19.9s	11.5(β^-)	1.5×10^{-6}

to be small but on the other hand, non-linearity due to PMT or electronics saturation may be large. Radioactive sources can be put in the target region from the calibration port at the top. A Cf fission source will be used to calibrate the 8 MeV Gd energy and efficiency. For higher energy prompt signals, there is no radioactive sources to cover the necessary energy range. However, the Michel electron has well known and similar energy spectrum as expected $\bar{\nu}_e$ energy spectrum and can be used to calibrate the energy. High energy cosmic spallation signals will also be used for the energy calibration.

The fiducial volume is defined by the Gd signal which occurs only in the neutrino target region and no fiducial cut will be applied at the analysis. Thus the vertex position uncertainty does not affect the accuracy of the detection efficiency for the first order. However, reconstructed vertex position will be used to measure baseline dependence of the oscillation, for event selection cut based on the distance between prompt and delayed signals, and to correct position dependence of energy response. Position along the z-axis can be calibrated by the deployed sources from the calibration port. For r-direction, the radius of the acrylic vessel wall can be identified by looking at the edge effect of signals. Non uniformity of signal distribution can be checked by looking at the uniformly distributed Michel electron or spallation signals.

E   MLF radiation survey

Radiation survey has been performed by MLF facility people for the safety issue. Especially, the survey held on 22-Oct-2012 is important measurement since the beam power is 284 kW, close to the beam power at the 1 ton scintillation measurement at BL13.

The survey was performed at many places at the MLF facility, and it showed that radiation level of BL13, where the 1 ton scintillator detector is located, is higher than that at any other points although it is much safer compared to the limit of radiation.

Table 14 summarizes the survey result for BL13 and the candidate site.

Point	neutron	gamma	comments
BL13	1.2μSv/h	0.5μSv/h	digit of gamma monitor is 0.1μSv/h
Candidate site	0.025μSv/h	0.1μSv/h	digit of neutron monitor is 0.01μSv/h.

Table 14: Radiation Survey results

This survey monitor counts any energy of the gamma and neutrons, therefore the numbers are not guranteed to be directly related to amount of the fast and slow neutrons, and gammas. However, the radiation from the neutrons, which are source of the many backgrounds, are reduced by almost two order of magnitudes compared between BL13 and the candidate site. Note that measured digit of gamma monitor is 0.1μSv/h, while a digit of neutron monitor is 0.01μSv/h.

This radiation survey reports support the PHITS conclusion.

F Consideration on the detector

F.1 An alternative detector concepts- pros and cons

An alternative option of the detector is segemnted detector like KARMEN [35]. Compared to the LSND type detector, thare are following pros and cons.

Pros;

- A vertex resolution is determined by the size of one module. The detector also recognizes the multi-vertices easily. Michel electrons originated by fast neutrons' interactions can be rejected with the features.

- The self-shielding region of the detector for gammas from PMTs and enviroment can be reduced since PMTs are attched outside of the detector.

- The pilot runs for physics with small number of modules can be performed. The prototype module can be tested easily.

Cons;

- Number of PMTs are larger than that in LSND type.

- Particle Identification with Cherenkov is difficult.

F.2 Bases of detector type choice

As described in the main text, fast neutrons can create Michel electrons via charged pion production, thus we have to remove the events carefully.

LSND type detectors cannot reconstruct multi-vertices correctly, therefore the most of events which have beam on-bunch activities has to be cut. This strategy may be damaged if the number of beam spills, which have on-bunch activities, is larger than those has no on beam bunch activity.

On the other hand, the segmented detector can reconstruct the on-bunch multi-vertices events correctly. The reconstructed vertices are used for the spatial veto for the Michel electrons without thrown away the event itself since the distance between the signal from charged pions (on-bunch) and Michel electrons are correlated as shown in Section 4.

In conclusion, the next background measurement determines the detector choice. If the on-bunch activities are manageable with a LSND type detector, the strategy in this proposal of the detector is kept, however it could be necessary to change it if the on-bunch activities requires it.

F.3 Vertex and Energy resolution for the alternative detector

KARMEN detector consists of liquid scintillator modules, which have size of $\sim$18cm $\times$ 18cm $\times$ 350cm. Four 3 inch PMTs are attached to both sides of the 350 cm length.

Vertex resolution for two directions are determined by module size. As known well, typical resolution of tracking is calculated that the size detector devided by $\sqrt{(12)}$, that is, 5.2 cm. The resolution for the long detector side is determined by the timing resolution of the optics (a path length of scintillation light and PMT response). The timing resolution of the KARMEN detector is 350 ps due to careful scintillation ray-trace simulation, and it provides 5 cm vertex resolution.

To identify the multiple vertices in an events, 5 cm vertex resolution is good enough since there are a few events in 50 tons fiducial volume, the overlap of the vertices are negliegibly small.

For the energy resolution, KARMEN achieved the $11.6\%\sqrt{(E)}$. It is similar or better than that of LSND type detector in the proposal.

G Possible future extension using a large detector at longer distance

If the neutrino oscillation is not found in the high Δm^2 region, the extension of the experiment exists to search for the sub-eV^2 region.

Fig. 57 shows the typical sensitivity of the experiment at 60m baseline. The blue line corresponds to 5σ sensitivity, and green one to 3σ. Here we assume the detector with a 1.0 k ton fiducial volume is used, and the detection effciency is 48%, MLF beam power is 1MW and exposure is 2 years (4000 hours / year). The sources of background and the fitting procedure are same as those described before.
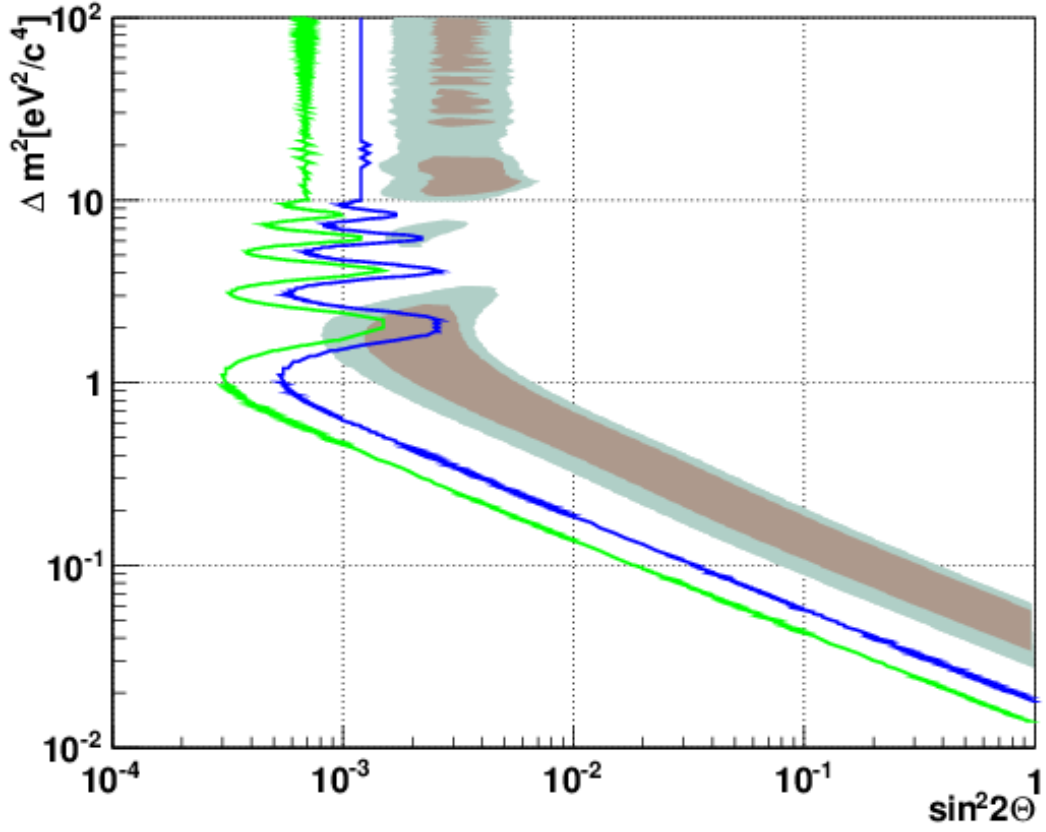
Figure 57: Typical sensitivity using a 1.0 kton detector with 60 m baseline. The blue line shows 5σ sensitivity, and green one corresponds to 3σ. Here we assume the detection effciency is 48%, MLF beam power is 1MW and exposure is 2 years (4000 hours / year). The sources of background and the fitting procedure are same as those described before.

References

[1] Y. Ashie et al. Super-Kamiokande Collaboration, Phys. Rev. D 71, 112005 (2005); Y. Fukuda et al. (Super-Kamiokande Collaboration), Phys. Rev. Lett. 81, 1562567 (1998).

[2] K. S. Hirata et al. [Kamiokande-II Collaboration], Phys. Rev. Lett. 63, 16 (1989); J. Abdurashitov et al. [SAGE Collaboration], Phys. Lett. B 328, 234 (1994); P. Anselmann et al. [GALLEX Collaboration], Phys. Lett. B 327, 377 (1994); S. Fukuda et al. [Super-Kamiokande Collaboration], Phys. Rev. Lett. 86, 5651 (2001); Q. R. Ahmad et al. [SNO Collaboration], Phys. Rev. Lett. 89, 011301 (2002); C. Arpesella et al. [Borexino Collaboration], Phys. Rev. Lett. 101, 091302 (2008).

[3] H. Ahn et al. [K2K Collaboration], Phys. Rev. D 74, 072003 (2006); P. Adamson et al. [MINOS Collaboration], Phys. Rev. Lett. 108, 191801 (2012); K. Abe et al. [T2K Collaboration], Phys. Rev. D 85, 031103 (2012); N. Agafonova et al. [OPERA Collaboration], Phys. Lett. B 691, 138 (2010).

[4] K. S. Hirata et al. [Kamiokande-II Collaboration], Phys. Rev. Lett. 63, 16 (1989); J. Abdurashitov et al. [SAGE Collaboration], Phys. Lett. B 328, 234 (1994); P. Anselmann et al. [GALLEX Collaboration], Phys. Lett. B 327, 377 (1994); S. Fukuda et al. [Super-Kamiokande Collaboration], Phys. Rev. Lett. 86, 5651 (2001); Q. R. Ahmad et al. [SNO Collaboration], Phys. Rev. Lett. 89, 011301 (2002); C. Arpesella et al. [Borexino Collaboration], Phys. Rev. Lett. 101, 091302 (2008).

[5] F. P. An et al. [Daya Bay Collaboration], Phys. Rev. Lett. 108, 171803 (2012); J. K. Ahn et al. [RENO Collaboration], Phys. Rev. Lett. 108, 191802 (2012); Y. Abe et al. [Double Chooz Collaboration], Phys. Rev. D 86, 052008 (2012); B. Achkar et al, Nucl. Phys. B 434, 503 (1995).

[6] B. Pontecorvo, JETP34, 172 (1958); V. N. Gribov and B. Pontecorvo, Phys. Lett. B 28, 493 (1969); Z. Maki, M. Nakagawa and S. Sakata, Prog. Theor. Phys. 28, 870 (1962).

[7] ALEPH, DELPHI, L3, OPAL, and SLD Collaborations, and LEP Electroweak Working Group, and SLD Electroweak Group, and SLD Heavy Flavour Group, Phys. Reports 427, 257 (2006).

[8] T. Asaka, S. Blanchet, and M. Shaposhnikov, Phys. Lett. B631, 151 (2005); A. Boyarsky, O. Ruchayskiy, and M. Shaposhnikov, Ann.Rev.Nucl.Part.Sci. 59, 191 (2009).

[9] A. Aguilar et al., Phys. Rev. D64, 112007 (2001).

[10] A. A. Aguilar-Arevalo et al. [MiniBooNE Collaboration], Phys.Rev.Lett.110.161801,2013.

[11] C. Giunti and M. Laveder, Phys.Rev.C 83 (2011) 065504

[12] Th. A. Mueller et al., Phys.Rev.C 83 (2011) 054615. P. Huber, Phys.Rev.C 84 (2011) 024617.

[13] J. Kopp et al., arXiv:1303.3011.

[14] M. Antonello et al., arXiv:1307.4699 [hep-ex].

[15] C. Giunti et al., Phys.Rev. D86 (2012) 113014.

[16] P. Vogel and J. F. Beacom, Physical Review D60 (053003).

[17] M. Shaevitz, 2011 Workshop on Baryon & Lepton Number Violation".

[18] G. Battistoni, S. Muraro, P.R. Sala, F. Cerutti, A. Ferrari, S. Roesler, A. Fasso', J. Ranft, Proceedings of the Hadronic Shower Simulation Workshop 2006, Fermilab 6–8 September 2006, M. Albrow, R. Raja eds., AIP Conference Proceeding 896, 31-49, (2007); A. Ferrari, P.R. Sala, A. Fasso', and J. Ranft, CERN-2005-10 (2005), INFN/TC_05/11, SLAC-R-773.

[19] J. Alison et al., IEEE Transactions on Nuclear Science 53 No. 1 (2006) 270-278; S. Agostinelli et al., Nuclear Instruments and Methods A 506 (2003) 250-303.

[20] T.Suzuki et.al., Phys. Rev. C 35 (1986) 2212.

[21] H. Iwase, K. Niita,T. Nakamura, JOURNAL OF NUCLEAR SCIENCE AND TECHNOLOGY 39 (11): 1142-1151 NOV 2002.

[22] M. Yeh, A. Garnov, and R.L. Hahn, Nucl. Instrum. and Meth. A578 (2007) 329-339.

[23] T.Matsubara, et al., Nucl. Instrum. and Meth. A661 (2012) 16-25.

[24] M. Nomachi, S. Ajimura, IEEE Transactions on Nuclear science, vol. 53, 2849-2852, (2006).

[25] S. Umehara, et. al., IEEE Nuclear Science Symposium Conference Record, 2091-2094, (2011).

[26] Masaharu Nomachi, Shuhei Ajimura, Takayuki Yuasa, Tadayuki Takahashi, Iwao Fujishiro, Fumio Hodoshima; SPACEWIRE BACKPLANE FOR GROUND EQUIPMENT, International Spacewire Conference 2013

[27] E. Kolbe, K. Langanke, G. Martnez-Pinedo, P. Vogel, J.Phys.G29:2569-2596,2003;

[28] J. Beringer et al. (Particle Data Group), Phys. Rev. D86, 010001 (2012).

[29] H. Furuta et al., "Pulse Shape Discrimination study with Gd loaded liquid scintillator for reactor neutrino monitoring", IEEE proceedings of the 2nd int. conf. ANIMMA 2011, Ghent (2011).

[30] Y-F. Wang et al., "Predicting Neutron Production from Cosmic-ray Muons", Phys. Rev. D 64, 013012 (2001).

[31] S. Abe et al. [KamLAND Collaboration], "Production of radioactive isotopes through cosmic muon spallation in KamLAND", Phys.Rev. C 81, 025807 (2010).

[32] E. Kolbe, "Differential cross sections for neutrino scattering on ^{12}C", Phys. Rev. C 54, 1741 (1996).

[33] H. Furuta et al., "On-site underground background measurements for the KASKA reactor-neutrino experiment", Nuclear Instruments and Methods, A,568,(2006),710-715.

[34] J. Kempa and A. Krawczynska, "Low energy muons in the cosmic radiation", Nuclear Physics B (Proc. Suppl.) 151(2006) 299-302.

[35] B. Armbruster et al. [KARMEN Collaboration], Phys. Rev. D **65**, 112001 (2002) [hep-ex/0203021].

[36] http://geant4.web.cern.ch/geant4/G4UsersDocuments/UsersGuides /PhysicsReferenceManual/html/node130.html.